UNIVERSIDAD DE SALAMANCA

DOCTORAL THESIS

Study of the macroscopic high-order harmonic emission from single-layer graphene

Author:

Roberto Boyero García

Supervisors:

Carlos Hernández García and Luis Plaja Rustein

Universidad de Salamanca,

Plaza de la Merced s/n, Salamanca, España

20 Oct, 2022

Publicaciones

La presente tesis doctoral se presenta como compendio de artículos e incluye tres trabajos originales publicados en revistas científicas cuyas referencias completas, autores y afiliciones de éstos se detallan a continuación:

1. R. Boyero-García, O. Zurrón-Cifuentes, L. Plaja, C. Hernández-García, Transverse phase matching of high-order harmonic generation in single-layer graphene. Opt. Express 29, 2488–2500 (2021).

2. R. Boyero-García, A. García-Cabrera, O. Zurrón-Cifuentes, C. Hernández-García, L. Plaja, Non-classical high harmonic generation in graphene driven by linearly-polarized laser pulses. Opt. Express 30, 15546–15555 (2022).

3. R. Boyero-García, A. García-Cabrera, O. Zurrón-Cifuentes, C. Hernández-García, L. Plaja, High-order harmonic spectroscopy of polycrystalline graphene. Opt. Mater. Express 12, 3543–3550 (2022).

Las siguientes publicaciones también son parte de la presente tesis:

1. O. Zurrón-Cifuentes, R. Boyero-García, C. Hernández-García, A. Picón, L. Plaja, Optical anisotropy of non-perturbative high-order harmonic generation in gapless graphene. Opt. Express 27, 7776–7786 (2019).

2. Óscar Zurrón-Cifuentes, R. Boyero-García, C. Hernández-García, L. Plaja, High harmonic generation in armchair carbon nanotubes. Opt. Express 28, 19760–19771 (2020)

VNiVERSiDAD D SALAMANCA

CAMPUS DE EXCELENCIA INTERNACIONAL

D. Luis Plaja Rustein, Catedrático de Óptica y D. Carlos Hernández García, Investigador Ramón y Cajal, ambos del departamento de Física Aplicada de la Universidad de Salamanca,

Hacen constar:

Que la tesis doctoral titulada "Study of the macroscopic high-order harmonic emission from single-layer graphene/ Estudio de la emisión macroscópica de armónicos de orden elevado en grafeno monocapa" ha sido realizada bajo su dirección en el Área de Óptica del Departamento de Física Aplicada de la Universidad de Salamanca por D. Roberto Boyero García.

Y para que así conste a los efectos oportunos, firman el presente documento en,

Salamanca, a 20 de octubre de 2022.

PLAJA RUSTEIN LUIS - 35084508D
lplaja@usal.es Universidad de Salamanca
2022.10.21 08:36:16 +02'00'

Fdo.: Luis Plaja Rustein

HERNANDEZ GARCIA CARLOS - 70879854H
2022.10.20 23:01:44 +02'00'

Fdo.: Carlos Hernández García

Dedicado a mi familia

Abstract

This thesis presents a theoretical study on the process of high-order harmonics generation (HHG) in single-layer graphene from the microscopic to tyhe macroscopic point of view. We start from the study of the role of the recently discovered imperfect recollisions in bulk solids, but in the context of a gapless monolayer such as graphene. Considering non-zero recollision distances between the electron-hole, we explain the high-harmonic emission observed at the final stages of the interaction, in the results obtained with the time-dependent Schrödinger equation, for recombination times greater than one cycle of the incident field. Next in this thesis, we present the first macroscopic analysis of the HHG process in graphene. We consider the influence of the spatial intensity distribution of the incident field on the total harmonic emission. The result concludes that there is a certain ring in the graphene target around the propagation axis, whose emissions govern the total emissions of the process. Finally, based on previous studies on the anisotropic behavior of the graphene sheet, we have developed a technique to characterize polycrystalline graphene using high-order harmonic spectroscopy.

Resumen

En esta tesis se presenta un estudio teórico sobre el proceso de generación de armónicos de orden elevado en una capa de grafeno desde el punto de vista microscópico hacia el macroscópico. Nuestros resultados parten del estudio del papel de las recolisiones imperfectas, recién descubiertas en sólidos gruesos, pero en el contexto de materiales monocapa sin gap como es el grafeno. Considerando distancias de recolision entre el par electrón-hueco diferentes de cero, explicamos las emisiones observadas en los resultados obtenidos con la ecuación de Schrödinger dependiente del tiempo, para tiempos de recombinación superiores a un ciclo del campo incidente. Además, presentamos el primer análisis macroscópico del proceso de HHG en grafeno. Consideramos la influencia de la distribución de intensidad espacial del campo incidente en la emisión total de armónicos. El resultado concluye que existe un determinado anillo en la lámina de grafeno en torno al eje de propagación, cuyas emisiones gobiernan las emisiones totales del proceso. Finalmente, basándonos en

estudios previos sobre el comportamiento anisótropo de la lámina de grafeno, hemos desarrollado una técnica para caracterizar grafeno policristalino mediante espectroscopia de armónicos de orden alto.

Agradecimientos

Hasta aquí llega una de las etapas más bonitas que he vivido en toda mi vida y, sin lugar a duda, ese podría ser el título de esta tesis. Durante estos más de cinco años he crecido enormemente tanto en lo profesional como en lo personal, y por suerte, no lo he hecho solo. A lo largo de todo este tiempo gracias a mucha gente he llegado a ser quién soy y realmente sería imposible mencionarlos a todos. Cualquier interacción, sea buena o mala, te condiciona y forja cada uno de los puntos que te describen ahora. Como se suele decir, de los errores se aprende.

Lo gracioso de esta historia es que nunca pretendí llegar a ser doctor. Cuando salí de realizar mi trabajo de fin de grado en el Centro de Láseres Pulsados dirigido por Álvaro Peralta Conde, allá por 2016, mi primer pensamiento fue: "yo quiero dedicarme a la investigación". Allí me descubrieron el sentido de todo lo que estaba estudiando y encontré mi motivación. Mi primer paso al acabar la carrera fue apuntarme al propio Máster de Física y Tecnología de los Láseres en la Universidad de Salamanca, donde descubrí a compañeros magníficos con la misma ilusión por aprender sobre el mundo de los láseres. La experiencia fue muy buena, tanto es así, que fue allí donde, de alguna manera, conseguí engañar a mis directores de tesis Carlos Hernández García y Luis Plaja Rustein. Inicialmente sólo iba a ser un contrato de cinco meses, que consiguió convertirse en dos años y así hasta llegar a hoy. Siento un profundo agradecimiento a mis dos directores por la oportunidad que me han brindado, siempre me han ayudado en todo lo que he necesitado y han encontrado un equilibrio perfecto entre ser directores y compañeros. Así como al resto del Grupo de Investigación en Aplicaciones del Láser y Fotónica, es magnífica la familia que habéis construido y sé que he tenido una suerte enorme en haber trabajado con todos vosotros, echaré de menos poner dinero para el bote del café. Y cómo no, mencionar a Laura Rego Cabezas y Aurora Crego García, mis compañeras y mis dos pilares durante todo este proceso. Los tres partimos desde el Máster y comenzamos

nuestro camino como doctorandos en aquel cuartucho del sótano. He vivido momentos maravillosos con vosotras, en congresos, seminarios y en algún bar que otro también. Muchas gracias por todo y, por cierto: "Mamá! Quiero ser doctor!", parece que lo hemos conseguido. En lo profesional, también me gustaría agradecer a Óscar Zurrón Cifuentes, para mí un ejemplo claro de pasión por la investigación, por el conocimiento y por haberme ayudado siempre que ha podido en el maravilloso mundo del grafeno. A Miguel Angel Silva Toledo y Fabian Scheiba, me abrieron las puertas de Hamburgo y me acogieron durante tres meses maravillosos que siempre recordaré junto con todos los compañeros en el centro Center for Free-Electron Laser Science, siempre tendréis las puertas de mi casa abiertas. Por último, a Máximo, mi profesor de instituto y de carrera, si acabé estudiando física fue sin duda gracias a ti.

Como decía al principio, esta etapa no sólo me ha proporcionado conocimiento, sino que también me ha hecho crecer en el plano personal. Por ello, quiero empezar agradeciendo a mí familia, mi padre Jose Ignacio y mi madre Dolores, me habéis dado absolutamente todo desde la mayor humildad para llegar a ser quien soy y jamás tendré palabras suficientes para agradecéroslo, os quiero con todo mi corazón, sé que estáis orgullosos de lo que soy, pero creedme que ojalá pudiera llegar a ser un uno por ciento de lo que sois vosotros. A mi hermana Marina, muchas gracias por estar ahí siempre, me das siempre todo sin pedirme nada a cambio y, pese a que seas la pequeña, eres una gran referencia para mí, sigue luchando por lo que te hace feliz, te quiero. A Marta, que eres una más de mí familia, sabes que esta última etapa ha sido especialmente dura, sin embargo, me has comprendido y me has ayudado en todo momento cuando quizá otra persona no hubiera aguantado, te lo agradezco profundamente a ti y también a toda tu familia que me ha hecho sentir uno más. Creo que formamos un gran equipo, por más momento bonitos a tu lado. A mis tíos Victor y Azu que siempre me habéis cuidado, a mis abuelos Victorio, Beatriz que sé que estaríais orgullosos. A mis abuelos Lola y Benito, a mi tío Beni, mi tía Toñi y mis primos Fory, Inma y Libia, somos una familia pequeña, pero entre todos nos queremos y sé que siempre puedo contar con vosotros esté donde esté. Como se suele decir, la familia no sólo es de sangre, sino que también se elige y yo he tenido la suerte de incluir a la mía personas maravillosas como Míguel, Adelfa y Miguelín y a mis hermanos de otra madre Josepa, Fer, Moreiro y Marina. También a

los Radicales, gracias por cada momento vivido, desde el principio me abristeis las puertas y me acogisteis sin apenas conocerme de nada, espero seguir creciendo con vosotros. Al Grupo 2, mis compañeros de carrera que quizá sin vosotros también la habría acabado, pero desde luego no habría sido ni la mitad de divertida. Y, por último, pero no menos importante, agradecer a Mar y Patrick, sois dos personas maravillosas que, pese a la distancia, hemos conseguido tener una amistad muy bonita.

Como dije al principio, mencionar a todo el mundo sería tarea imposible, sin embargo, agradezco a cada una de las personas que ha decidido dedicarme una porción de su tiempo.

Contents

Chapter 1

Introduction

From its invention in 1960 to our days, the wide applications of laser light have revolutionized areas of knowledge such as industry, medicine, communications, etc... In fundamental science, lasers play a leading role in capturing the dynamics of ultrafast phenomena. The shortest temporal resolution that can be captured by laser light is dictated by the pulse duration. The length of a laser pulse has a fundamental lower limit in the period of the electromagnetic wave. Therefore, high-frequency laser pulses are unavoidable in order to track the fastest electronic dynamics in matter. The development of such sources was boosted with the development of short infrared pulses at high intensity using the chirped pulse amplification (CPA) technique developed by 2018 Nobel Prize laureates Strickland and Mourou [1]. Nowadays, intense laser technology allows the study and control of a variety of strong laser-matter interaction phenomena at the femtosecond (10^{-15}s) or even attosecond (10^{-18}s) time scales. Among them, high harmonic generation (HHG) stands as a unique non-perturbative process, that allows not only to generate high-frequency coherent radiation, that can be used to synthesize the shortest laser pulses created up to now [2], but also to study ultrafast laser-driven electronic dynamics, whose details are encoded in the spectrum of the emitted radiation. HHG results from the strong non-lineal response of matter to high intensity laser radiation. The non-perturbative interaction induces an extreme non-linear dynamics in the system, from which follows the emission of high-frequency radiation. The high-frequency spectrum is composed by a phase-locked frequency comb, reaching the extreme ultraviolet (XUV) or even the soft X-rays. The extraordinary coherence of this process allows to synthesize these harmonics into trains of pulses with time durations as short as few tens

of attoseconds. The first evidences of this non-perturbative character of HHG were obtained from gases in the late 1980s. McPherson et al. [3] produced high-order harmonics up to the seventeenth (14.6 nm) of a 248 nm laser in Ne, and, one year later, M. Ferray et al. [4] reached the 33rd harmonic (32.2 nm) from a 1064 nm laser in Ar. A few years later, in 1993, a semiclassical explanation of the process behind HHG was proposed in the so-called *three-step model* (see Fig. 1.1) [5, 6]: first, the atom is tunnel ionized by the strong laser field, generating an electron wave packet in the continuum every time the field reaches an amplitude maximum; during a second step, the wave packet evolves accelerated by the field until, in a third step, it recombines with the parent ion. In this later step the high frequency radiation is emitted in the form of harmonics.

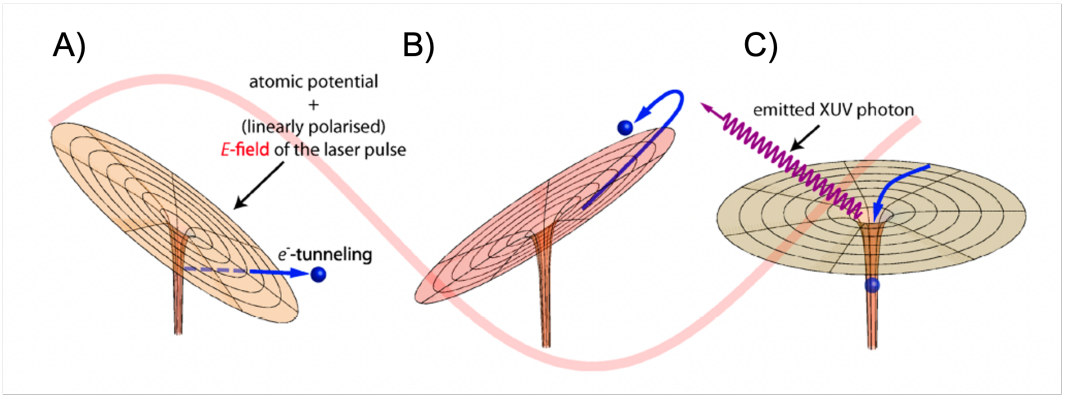

FIGURE 1.1: Semiclassical *three-step model* of HHG. (A) The electron is tunnel-ionized into the continuum. (B) The laser field accelerates the electron, which is brought back to the parent ion. (C) Upon recombination, high frequency radiation up to the XUV or soft x-rays is emitted. Figure extracted from [7].

As we can see in Fig. 1.2, where we reproduce the experimental harmonic spectrum obtained by L'Huillier et al. in 1989 [8], the lower part of the spectrum is composed by harmonics with decreasing efficiency, while the highest frequency spectrum forms a *plateau* that extends up to a cutoff frequency. The maximum energy radiated depends on the ionization energy of the gas, as well as on the ponderomotive energy of the electron in the continuum [9], which in turn depends on the external field wavelength and intensity.

The *three-step model* describes HHG in gases from a microscopic point of view. However, a constructive interference of the HHG emissions from all the atoms in the gas target –also known as phase-matching condition– is crucial to efficiently produce

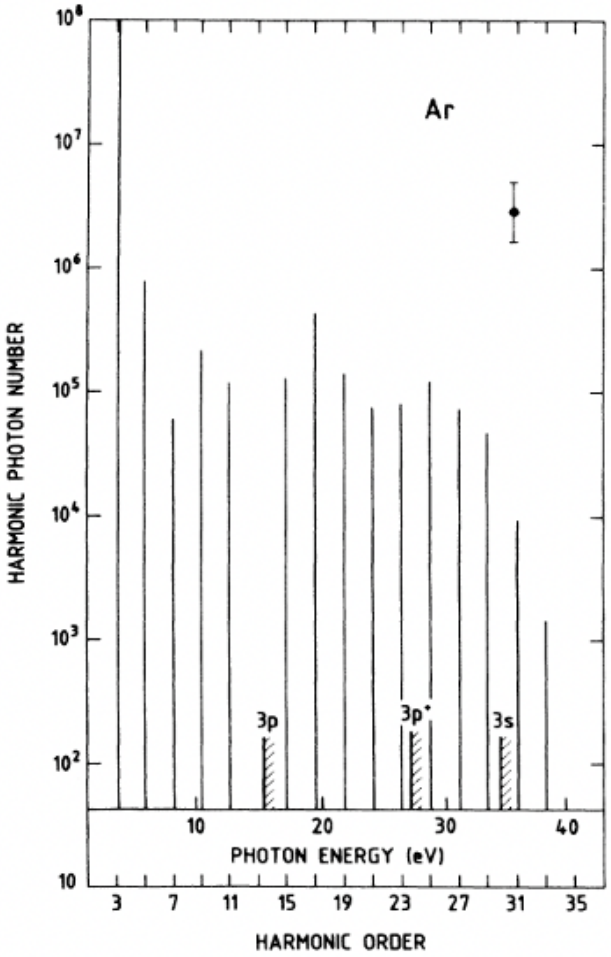

FIGURE 1.2: Experimental result of HHG in Ar driven by a laser pulse of peak intensity $3 \times 10^{13} W/cm^2$, centered at 1064 nm, extracted from Ref. [8]. The harmonic distribution reflects three regions: a exponential decrease for the first harmonics, a *plateau*, and a cutoff frequency.

harmonics that can be measured and also used in practical applications. Therefore, a full description of HHG must account for the single-atom emission as well as the build-up of the harmonic signal in the macroscopic target. We define the phase-matching condition as a situation in which the phase front of the harmonic field being generated at the target overlaps the phase front of the harmonic field already propagating through the sample (see Fig. 1.3).

In 1995, Salières et al. [11] presented a theoretical study for the phase-matching dependency with the driving-beam geometry, in particular with the position of the laser focus relative to the target, and opened the door to the successive studies of harmonic phase-matching [12–15]. The proper control of phase-matching is also relevant for the fine-tuning of the HHG process. In particular, the control of the chirp of

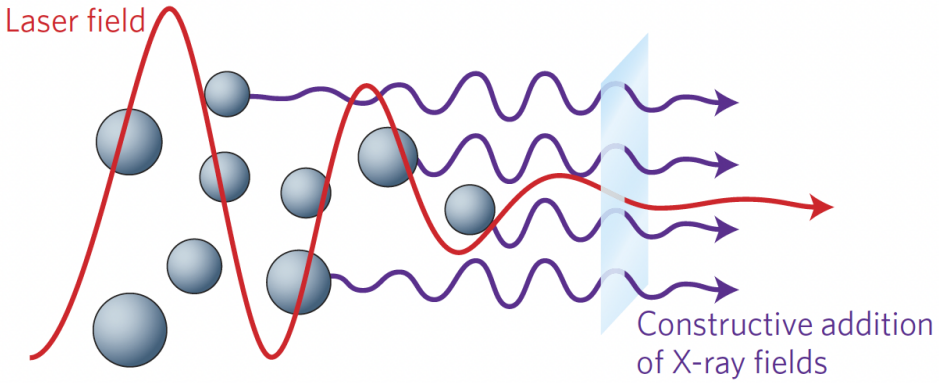

FIGURE 1.3: Basic representation of the phase-matching process in HHG. The driving field interacts with the atoms in a medium, generating harmonic emissions with a constructive addition. Figure extracted from [10]

the harmonic field was relevant for the first experimental demonstration of attosecond pulses in 2001 by Paul et al. [16], obtaining a train of 250 attosecond pulses, and for the first attosecond metrology experiments by Hentschel et al. [17], where they traced the electronic dynamics with a time resolution below 150 as. Remarkably, even in some of the most recent results of HHG, such as the generation of isolated attosecond pulses [18, 19], and the generation of circularly polarized harmonics [20, 21], phase-matching plays a relevant role.

Initially, HHG studies considered mainly gaseous targets. However, in the last two decades the development of intense laser sources in the mid-infrared (mid-IR) raised the possibility of driving HHG in solids. Solid targets have a larger density of electrons, therefore, in principle, can provide brighter harmonics. The first observation of HHG from bulk crystals was reported in 2011 by Ghimire et al. [22] using ZnO as target (see Fig. 1.4). Afterwards, addition studies showed the viability of HHG in other finite-gap solids, such as ZnO, MoS_2, ZnSe, GaSe or SiO_2 [22–26].

From a semiclassical point of view, bulk solids generate harmonics similarly to the *three-step model* in atoms. In this case, ionization is replaced by tunnel excitation of electrons from the valence to the to the conduction bands, and the final step is the electron-hole recombination. In crystalline solids, the spectral cutoff corresponds to the maximum gap explored by the electron-hole pair during its excursion. Note that the electron and hole trajectories in solids are not in free space, and thus they depend

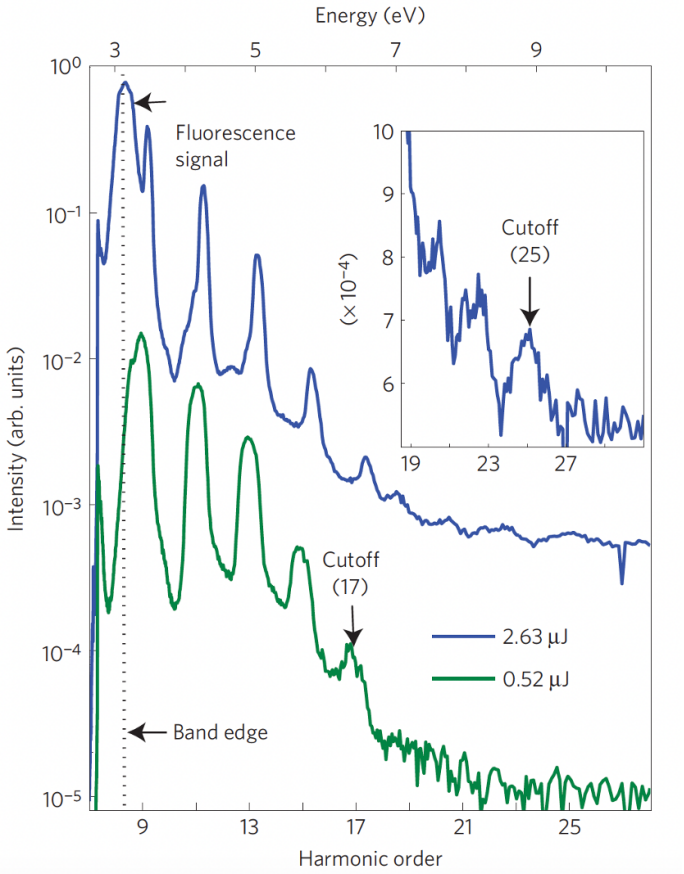

FIGURE 1.4: First HHG results obtained experimentally in a bulk solid, 500-μm-thick ZnO crystal. The green (blue) spectrum is generated with a driving pulse energy of 0.52 μJ (2.63 μJ) and centered at 3.25 μm. The inset shows the blue spectrum cutoff on a linear scale. Figure extracted from [22].

on the nature of the crystal and on the details of the band structure. A last important point is that, while atomic targets are isotropic, solid crystals may present an anisotropy in their nonlinear response, allowing the generation of elliptically or circularly polarized harmonics from linearly polarized drivers [23, 25, 27–30]. Nowadays, a new variety of targets, such as topological insulators and 2D materials, are becoming potential candidates for HHG due to their different geometrical or topological characteristics [23, 31]. In particular, there is a major interest in monolayers with zero gap, such as single-layer graphene. In this case, the mechanism of HHG substitutes tunnel excitation by the non-adiabatic crossings near the points where the valence and conduction bands are in contact (the so-called Dirac points) (see Fig. 1.5).

A paradigmatic example of 2D solid is graphene. In 1962 P.R. Wallace computed

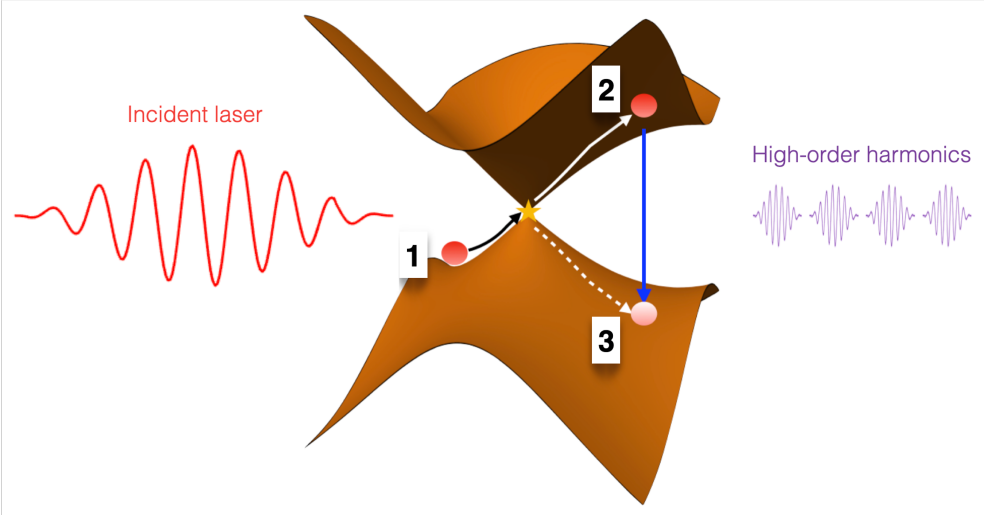

FIGURE 1.5: The *three-step model* scheme for HHG in a 2D-material with zero gap, like graphene. In a first step, the external field drives the electron-hole pair through the Dirac point, where the electron is promoted to the conduction band, creating a valence hole. Then, in a second step, it is accelerated by the external field along the band and, in the last step, the electron-hole pair recombines emitting the high-order harmonics.

the electronic energy bands and the first Brillouin zone of a single hexagonal layer of graphite using the tight binding approximation [32]. Later on, in 1986, these graphite single-layers were termed as graphene by Hanns-Peter Boehm, Ralph Setton and Eberhard Stumpp [33], combining the word *graphito*, referring to carbon in its ordered crystalline form, and the suffix *-ene*, referring to polycyclic aromatic hydrocarbons, in which the carbon atoms form hexagonal, or six-sided, ring structures. Graphene is composed of two carbon atoms per unit cell with four electrons each, three of them placed in hybrid sp^2 orbitals forming σ-bonds, while the fourth occupies an orbital perpendicular to the lattice plane, forming π and π^*-bonds. As a result, graphene is a 2-D hexagonal crystal built from two atomic sublatices, referred as A and B. The distinction between lattices A and B stems from their relative position in the 3-D structure of graphite, A being the lattice with neighbors above and below (see Fig. 1.6).

In 2004, Geim and Novoselov obtained for the first time isolated graphene via exfoliation with the well known *scotch-tape* method [35]. This achievement was awarded with the Nobel Prize in Physics in 2010. They also characterized its semimetal electronic properties and confirmed its gapless nature. Near the Dirac points the energy dispersion is approximately linear, forming conical shapes.

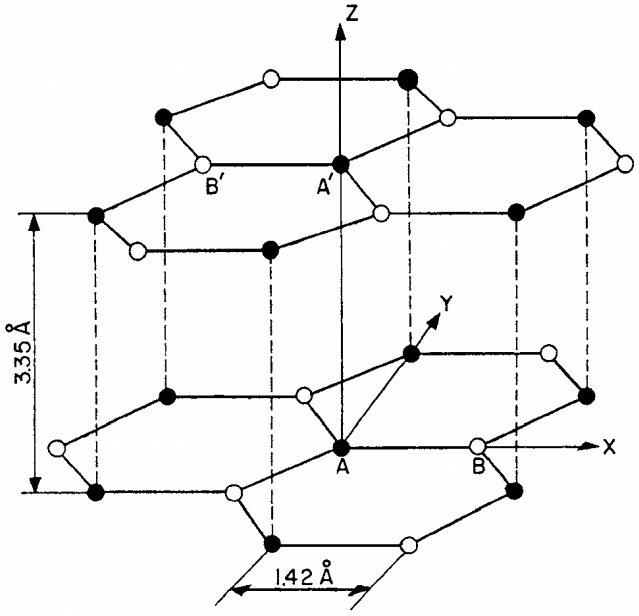

FIGURE 1.6: Scheme of the graphite structure. Atoms A and A′ (full dots) have neighbors in adjacent layer planes at 3.35 Å distance. On the other hand, B and B′ (open dots) are separated 6.71 Å by their neighbors in above and below planes. Figure extracted from [34].

In these cones, the mobility of both electron or hole carries can exceed 15.000 $cm^2V^{-1}s^{-1}$ in normal conditions, with carrier concentrations up to $10^{13}cm^{-2}$, and the electrons behave as massless quasiparticles with Fermy velocity $c/300$, being c the speed of light. Noticeably, the quantum Hall effect can be also observed under the same laboratory conditions [36]. Attending to the massless fermion equivalence, the Dirac equation can be used to describe most of the electronic properties of graphene [37]. The double sublattice configuration of graphene has as direct consequence an additional degree of freedom known as pseudospin or valley degeneracy. This two different states for the wave functions can be also understood as the chirality of the graphene [38, 39].

In terms of the optical response, graphene under intense external electric fields is strongly nonlinear. As mentioned above, the presence of Dirac points allows the generation of electron-hole pairs without tunnel excitation [40]. Mikhailov et al. in 2007 [41, 42] applied a quasi-classical theory to predict that graphene emits high-order harmonics. They estimated the production of frequencies up to 5-10 THz, thus, opening the door to graphene applications in terahertz electronics. Ishikawa et al.

[43] studied the dynamics of harmonic generation using optical Bloch equations, analyzing the interplay between intraband and interband dynamics at the Dirac points. Three years later, it was reported for the first time the third harmonic generation in graphene [44]. Finally, in 2017 Taucer et al. [45] and Yoshikawa et al. [30] produced nonperturbative harmonics up to the fith and ninth order (see Fig. 1.7), demonstrating experimentally for the first time the process of HHG in single-layer graphene. They confirmed the prediction of the high efficiency of the process, and also reported the dependency of the harmonic intensity with the polarization of the driving field, a consequence of graphene's non-linear anisotropy.

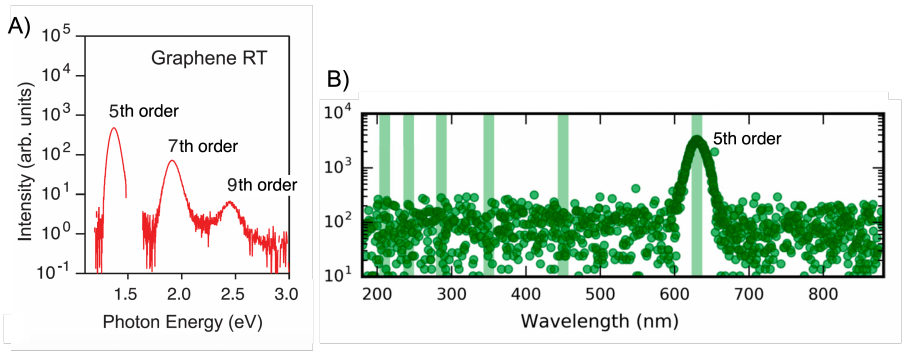

FIGURE 1.7: First high harmonic spectra obtained in single-layer graphene. In panel A), we present the result extracted from Yoshikawa et al. (figure adapted from [30]), reaching up to the 9th-order with a driving pulse centered at 0.26 eV ($\sim$ 4.8μm). In panel B), we present the spectrum from Taucer et al. (figure adapted from [45]), where the 5th-order is observed with a driving wavelength of 3.1μm.

During the last two decades, the combination of all the properties enumerated above has motivated the choice of graphene as a replacement of other materials in already existing applications, and also opening the door to future ones. It is used in a wide range of fields, from supporting nano-objects for transmission electron microscopy (TEM) [46], the use in solar cells as transparent conductive coating [47], or as transistors for high-frequency applications [48]. Most applications, however, claim for the production of large-area sheets, beyond the micrometre-size. The most extended industrial production method is chemical vapor deposition (CVD). Unfortunately, the single layers of graphene obtained in mass production are polycrystals (see Fig. 1.8). Thus, studies of HHG in polycrystalline graphene are required.

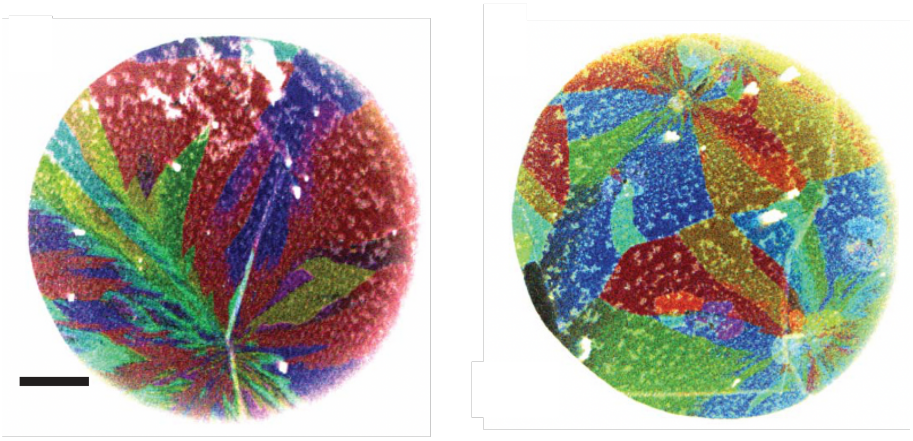

FIGURE 1.8: Images of different regions in a polycrystalline graphene sample generated by CVD. Both pictures are obtained by an electron microscopy technique called dark-field transmission electron microscopy (DF-TEM). The grain imaging gives false-colours to distinguish the shapes and orientations. Scale bar is 500 nm. Figure extracted from [49]

1.1 Objectives of this thesis and publications

The main motivation of this thesis is to contribute to the study of the fundamental aspects of high-harmonic generation from single-layer graphene. Taking as starting point previous studies on the microscopic theory of HHG from graphene, such as Ref. [40], we have focused into the exploration of the macroscopic response in order to approach the experimental situation [30, 45, 50]. This thesis report contains our results published in the following references:

1. Reference [51]. R. Boyero-García, O. Zurrón-Cifuentes, L. Plaja, C. Hernández-García, Transverse phase-matching of high-order harmonic generation in single-layer graphene. *Opt. Express* **29**, 2488–2500 (2021). Even though a single-layer graphene is a 2D material and the longitudinal propagation does not play a role in the final emission of harmonics, the phase-matching in the superposition of the local emissions in the graphene's plane still has a fundamental role. The so-called *transverse phase-matching* is well understood in gas targets. Our results determine that the total harmonic emission from the grahene layer is dominated by a certain phase-matched ring around the driving beam propagation axis.

2. Reference [52]. R. Boyero-García, A. García-Cabrera, O. Zurrón-Cifuentes, C. Hernández-García, L. Plaja, Non-classical high harmonic generation in

graphene driven by linearly polarized laser pulses. *Opt. Express* **30**, 15546–15555 (2022). From a semiclassical point of view, it is known that the number of electron trajectories in HHG from single-layer graphene is far greater than in finite gap solids, due to the replacement of tunnel excitation by the non-adiabatic excitation near the Dirac points. Recent results in HHG in bulk solids [53, 54] have demonstrated that non-classical trajectories are relevant in the build-up of the final HHG spectrum. In this paper we showed the signature of these non-classical trajectories in the harmonic spectrum obtained in graphene.

3. Reference [55]. R. Boyero-García, A. García-Cabrera, O. Zurrón-Cifuentes, C. Hernández-García, L. Plaja, High-order harmonic spectroscopy of polycrystalline graphene. *Opt. Mater. Express* **12**, 3543–3550 (2022). Chemical vapor deposition is one of the most popular techniques to obtain large areas of graphene, required to most industrial applications. This technique, however, produces polycrystals with different domain sizes and orientations. In order to characterize the polycrystal structure, i.e. to provide for the distributions of sizes and orientations, we propose to explore the graphene's non-linear anisotropic response. Following that, we present HHG simulations in polycrystalline graphene and a study of the harmonic polarization dependence on the size and orientation of the polycrystals.

The above results take as starting point previous results obtained along the thesis where the student participates also as a co-author:

1. Reference [56]. O. Zurrón-Cifuentes, R. Boyero-García, C. Hernández-García, A. Picón, L. Plaja, Optical anisotropy of non-perturbative high-order harmonic generation in gapless graphene. *Opt. Express* **27**, 7776–7786 (2019). In this work, we studied the influence of graphene's symmetry in the harmonic emission. The non-linear optic response leads to the generation of harmonics with elliptical or circular polarization when driven by a linearly polarized electric field.

2. Reference [57]. O. Zurrón-Cifuentes, R. Boyero-García, C. Hernández-García, L. Plaja, High harmonic generation in armchair carbon nanotubes. *Opt. Express*

28, 19760–19771 (2020). In order to explore HHG in new configurations of carbon allotropes, we solved numerically the HHG in carbon nanotubes. We focused into the emission of armchair-type with chiral index (n, n) irradiated by a mid-IR laser.

Chapter 2

Introducción

Desde su invención en 1960 hasta nuestros días, la variedad de aplicaciones de la luz láser ha revolucionado áreas de conocimientos como la industria, la medicina, las comunicaciones, etc... En ciencia fundamental, los láseres juegan un papel principal en la captura de la dinámica de fenómenos ultrarrápidos. La resolución temporal más breve obtenida con un láser pulsado viene dada por la duración del pulso. Esta tiene un límite inferior fundamental en el período de la onda electromagnética. Por lo tanto, pulsos láser de alta frecuencia son necesarios para observar la dinámica electrónica más rápida que ocurre en la materia. El desarrollo tecnológico de este tipo de fuentes de luz fue impulsado gracias a la obtención de pulsos cortos infrarrojos de alta intensidad. La clave de este desarrollo es la aparición de la técnica *chirp pulse amplification* (CPA), elaborada por Strickland y Mourou, Premios Nobel en Física en 2018 [1]. Hoy en día, las tecnologías relacionadas con los láseres intensos permiten estudiar y controlar una variedad de fenómenos de interacción láser-materia en la escala temporal de los femtosegundos (10^{-15} segundos) o, incluso, de los attosegundos (10^{-18} segundos). Entre ellas, la generación de armónicos de orden elevado (HHG, de sus siglas en inglés) se erige como el único proceso que permite generar radiación coherente de alta frecuencia, que puede ser usada para sintetizar los pulsos láseres más cortos creados hasta la fecha [2]. Además, permiten estudiar la dinámica electrónica ultrarrápida inducida por láseres, cuya traza queda reflejada en el espectro de la radiación emitida. El proceso de HHG resulta de la respuesta altamente no lineal de la materia a la radiación láser de alta intensidad. La interacción no perturbativa induce dinámicas extremadamente no lineales en el sistema, que resultan en

la emisión de radiación de alta frecuencia. El espectro de esta radiación está compuesto por un peine de frecuencias (o armónicos) que presentan una fase regular y que se extienden hasta el ultravioleta extremo (XUV) o, incluso, hasta los rayos X blandos. La extraordinaria coherencia de este proceso permite sintetizar estos armónicos en un tren de pulsos con duraciones temporales de unas pocas decenas de attosegundos. Las primeras evidencias del carácter no perturbativo del proceso de HHG se obtuvieron irradiando gases nobles a finales de los años 80. McPherson et al. [3] obtuvieron armónicos hasta el orden 17 (14.6 nm) a partir de un láser de 248 nm de longitud de onda interaccionando con neón. Un año más tarde, M. Ferray et al. [4] consiguieron el armónico 33 (32.2 nm) gracias a la interacción de un láser de 1064 nm en argón. Pocos años más tarde, en 1993, se propuso una explicación semiclásica para explicar la física subyacente al proceso de HHG, en lo que se conoce como el *modelo de los tres pasos* (ver Fig. 2.1) [5, 6]: primero, el átomo es ionizado por túnel mediante un campo láser intenso, generando un paquete de ondas electrónico en el continuo cada vez que el campo llega a su máxima amplitud; durante el segundo paso, el paquete de ondas evoluciona en el continuo viéndose acelerado por el campo láser hasta que, en el tercer paso, recombina con el ion padre. En este último paso la radiación de alta frecuencia es emitida en forma de armónicos de orden elevado.

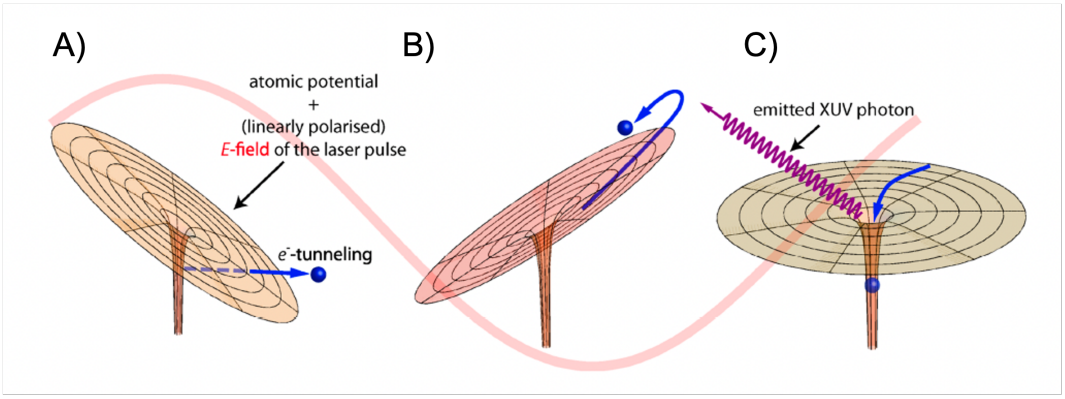

FIGURE 2.1: *Modelo de los tres pasos* semiclásico que permite explicar el proceso de HHG. (A) El electrón se ioniza por túnel al continuo. (B) El campo láser acelera el electrón, el cual es llevado de vuelta al ion padre. (C) Una vez recombina, se emite radiación de alta frecuencia, hasta el ultravioleta extremo o los rayos X blandos. Figura extraída de [7].

Como podemos ver en la Fig. 2.2, donde reproducimos el espectro experimental

de armónicos obtenido por L'Huillier et al. en 1989 [8], la parte baja del espectro está compuesta por armónicos cuya eficiencia decrece, mientras que las frecuencias altas del espectro forman un *plateau* que se extiende hasta la frecuencia de corte. La máxima energía radiada depende del potencial de ionización del gas, así como de la energía ponderomotriz del electrón en el continuo [9], que a su vez depende de la longitud de onda y la intensidad del campo incidente.

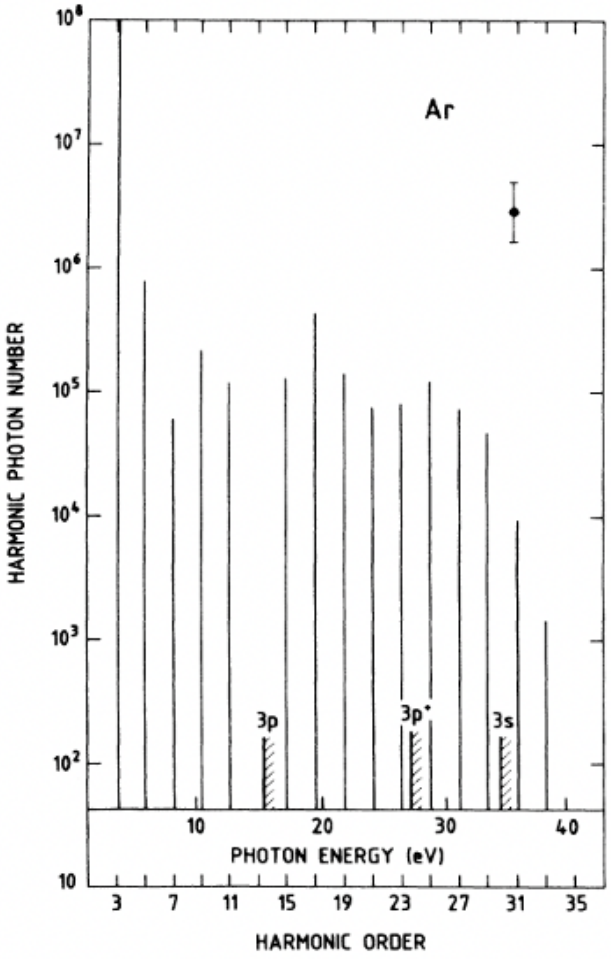

FIGURE 2.2: Resultado experimental de HHG en Ar inducido por un pulso láser con intensidad pico de $3 \times 10^{13} W/cm^2$, centrado en 1064 nm. Extraído de la Ref. [8]. El espectro de armónicos refleja tres regiones: un decrecimiento exponencial para los armónicos bajos, un *plateau* de armónicos de intensidad similar, que se extiende hasta la frecuencia de corte, a partir de donde la señal decrece bruscamente.

El *modelo de los tres pasos* describe el proceso de HHG en gases desde un punto de vista microscópico. Sin embargo, es crucial adoptar una visión macroscópica de cara a tener una interferencia constructiva entre la radiación emitida por todos los átomos del gas –también conocida como condición de acuerdo de fase— para

producir eficientemente armónicos que puedan ser medidos y/o utilizados en aplicaciones prácticas. Por lo tanto, una descripción completa del proceso de HHG tiene que tener en cuenta tanto la emisión de un solo átomo como la suma de la señal de armónicos en un medio macroscópico. Definimos la condición de acuerdo de fase como la situación en la que el frente de ondas del campo de armónicos generado en el medio coincide con el frente de ondas del campo de armónicos que ya se estaban propagando en la muestra (ver Fig. 2.3).

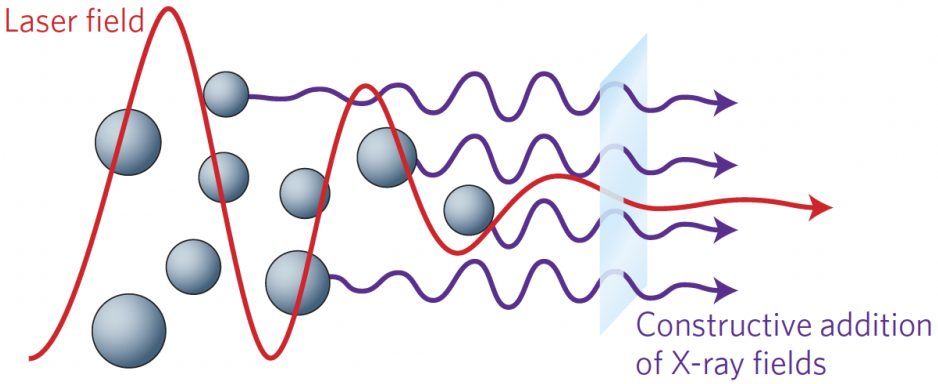

FIGURE 2.3: Representación básica del proceso de acuerdo de fase en el proceso de HHG. El campo externo interacciona con el átomo en el medio, generando una emisión de armónicos que se suman constructivamente. Figura extraída de [10].

En 1995, Salières et al. [11] presentaron un estudio teórico de la dependencia del acuerdo de fase con la geometría del haz externo. En particular, estudiaron cómo varía el proceso de HHG con la posición relativa entre el foco del láser incidente y el medio, abriendo el camino a posteriores estudios de acuerdo de fase en HHG [12–15]. El control adecuado del acuerdo de fase es relevante para un ajuste fino de las características de la radiación emitida en el proceso de HHG. En particular, el control del *chirp* del campo de armónicos fue relevante para la primera demonstración experimental de pulsos de attosegundo en 2001 por Paul et al. [16], obteniendo un tren de pulsos de 250 attosegundos, así como para el primer experimento de metrología de attosegundo realizado por Hentschel et al. [17], donde estudiaron dinámicas electrónicas con una resolución temporal por debajo de 150 as. Sorprendentemente, incluso en algunos de los más trabajos más recientes de HHG el ajuste de fase juega un papel fundamental, como ocurre en la generación de pulsos de attosegundo aislados [18, 19], y en la generación de armónicos polarizados circularmente [20, 21].

Inicialmente, los estudios de HHG consideraban medios gaseosos. Sin embargo, en las dos últimas décadas el desarrollo de fuentes láser en el infrarrojo medio (mid-IR, de sus siglas en inglés) ha conllevado la posibilidad de realizar HHG en sólidos. Los sólidos tienen una gran densidad de electrones, por tanto, en principio, pueden generar armónicos más brillantes. La primera observación de HHG en cristales gruesos fue reportado en 2011 por Ghimire et al. [22] utilizando ZnO (ver Fig. 2.4). Posteriormente, diferentes estudios han mostrado la viabilidad de HHG en otros sólidos de *gap* finito, como por ejemplo ZnO, MoS_2, ZnSe, GaSe o SiO_2 [22–26].

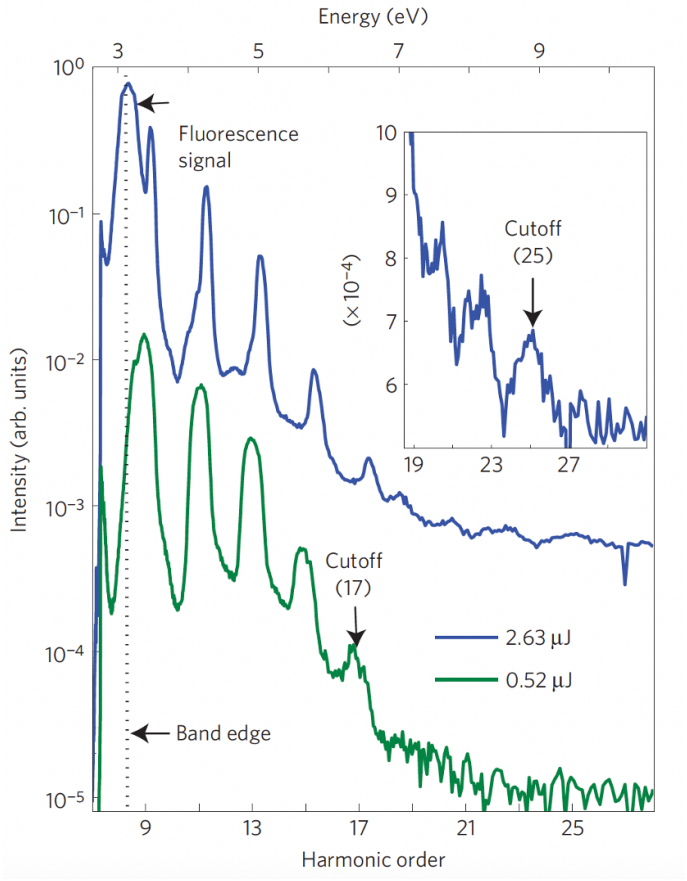

FIGURE 2.4: Primer resultado de HHG obtenido experimentalmente en un sólido grueso, cristal de ZnO de 500 μm de grosor. El espectro verde (azul) se ha generado con un pulso externo con energía de 0.52 μJ (2.63 μJ) y centrado en 3.25 μm. La figura insertada muestra la frecuencia de corte del espectro azul en escala lineal. Figura extraída de [22].

Desde un punto de vista semiclásico, los sólidos gruesos generan armónicos de una manera similar al *modelo de los tres pasos* que tiene lugar en átomos. En este caso, la ionización se remplaza por la excitación túnel de los electrones de la banda de valencia a la de conducción, y el último paso por la recombinación de la pareja

electrón-hueco. En sólidos cristalinos la frecuencia de corte del espectro de armónicos corresponde con el *gap* máximo que encuentra el par electrón-hueco durante su excursión. Cabe resaltar que las trayectorias del electrón y del hueco no están en el espacio libre y, por lo tanto, dependen de la naturaleza del cristal y de los detalles de la estructura de bandas. Un último aspecto a tener en cuenta es que, si bien los medios atómicos son isótropos, los cristales sólidos pueden presentar una anisotropía en su respuesta no lineal. Esto permite la generación de armónicos con polarización elíptica o circular a partir de campos láser polarizados linealmente [23, 25, 27–30]. Hoy en día, una nueva variedad de medios, como los aislantes topológicos o los materiales 2D, se están convirtiendo en candidatos potenciales para el proceso de HHG debido a sus peculiares características geométricas o topológicas [23, 31]. En particular, existe un gran interés en monocapas con *gap* cero, como el grafeno de una sola capa. En este caso, el mecanismo de HHG sustituye la excitación por túnel por los cruces no adiabáticos cerca de puntos donde las bandas de valencia y conducción están en contacto (los llamados puntos de Dirac) (ver Fig. 2.5).

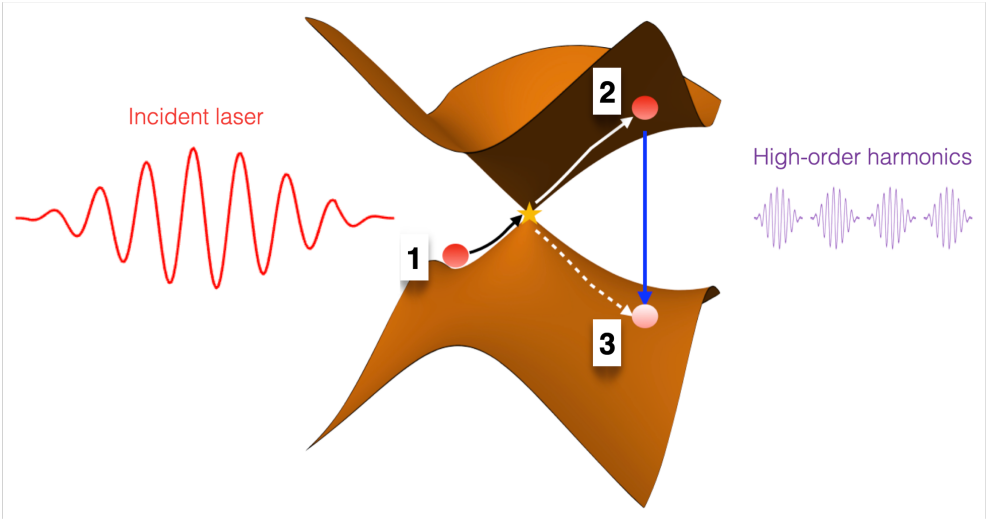

FIGURE 2.5: El esquema del *modelo de los tres pasos* del proceso de HHG en un material 2D con *gap* cero, como el grafeno. En un primer paso, el campo externo conduce al par electrón-hueco a través del punto de Dirac, donde el electrón es promovido a la banda de conducción. Luego, en un segundo paso, el par electrón-hueco es acelerado por el campo externo a lo largo de la banda y, en el último paso, el par se recombina emitiendo los armónicos de alto orden.

Un ejemplo paradigmático de sólido 2D es el grafeno. En 1962, PR Wallace calculó las bandas de energía electrónica y la primera zona de Brillouin de una sola capa hexagonal de grafito utilizando la aproximación de *tight-binding* [32]. Más tarde, en

1986, estas capas aisladas de grafito fueron denominadas grafeno por Hanns-Peter Boehm, Ralph Setton y Eberhard Stumpp [33], combinando la palabra *graphito*, que se refiere al carbono en su forma cristalina ordenada, y el sufijo *-ene*, que se refiere a los hidrocarburos aromáticos policíclicos, en los cuales los átomos de carbono forman estructuras de anillos hexagonales o de seis lados. El grafeno está compuesto por dos átomos de carbono por celda unitaria con cuatro electrones cada uno, tres de ellos colocados en orbitales híbridos sp^2 que forman enlaces σ, mientras que el cuarto ocupa un orbital perpendicular al plano de la red, formando enlaces π y π^*. Como resultado, el grafeno es un cristal hexagonal bidimensional construido a partir de dos subredes atómicas, denominadas A y B. La distinción entre las redes A y B proviene de su posición relativa en la estructura 3D del grafito, siendo A la red con vecinos arriba y abajo (ver Fig. 2.6).

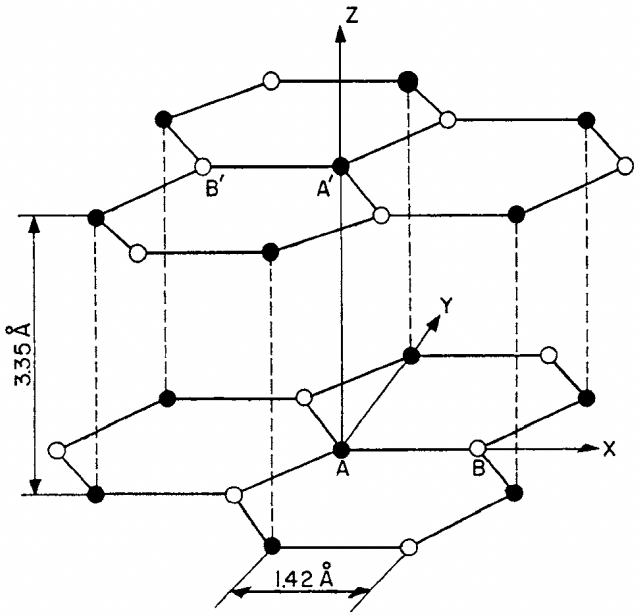

FIGURE 2.6: Esquema de la estructura del grafito. Los átomos A y A′ (puntos completos) tienen vecinos en planos de capas adyacentes a 3.35 Å de distancia. Por otro lado, B y B′ (puntos vaíos) están separados 6.71 Å por sus vecinos en los planos superior e inferior. Figura extraída de [34].

En 2004, Geim y Novoselov obtuvieron por primera vez grafeno aislado mediante exfoliación con el conocido método *scotch-tape* [35]. Este logro fue galardonado con el Premio Nobel de Física en el año 2010. También caracterizaron sus propiedades electrónicas semimetálicas y confirmaron su naturaleza sin *gap*. Cerca

de los puntos de Dirac la dispersión de energía es aproximadamente lineal, formando conos. En estos conos la movilidad tanto de electrones como de huecos puede superar los 15.000 $cm^2V^{-1}s^{-1}$ en condiciones normales, con concentraciones de portadores de hasta $10^{13}cm^{-2}$, y los electrones se comportan como cuasipartículas sin masa con velocidad de Fermy $c/300$, siendo c la velocidad de la luz. De hecho, el efecto Hall cuántico también se puede observar bajo las mismas condiciones de laboratorio [36]. Atendiendo a la equivalencia del fermión sin masa, la ecuación de Dirac se puede utilizar para describir la mayoría de las propiedades electrónicas del grafeno [37]. La configuración de doble subred del grafeno tiene como consecuencia directa un grado adicional de libertad conocido como pseudospin o degeneración de valle. Estos dos estados diferentes para las funciones de onda también pueden entenderse como la quiralidad del grafeno [38, 39].

En términos de respuesta óptica, el grafeno bajo campos eléctricos externos intensos es fuertemente no lineal. Como se mencionó anteriormente, la presencia de puntos de Dirac permite la generación de pares electrón-hueco sin excitación de túnel [40]. Mijailov et al. en 2007 [41, 42] obtuvieron una teoría cuasi-clásica para predecir que el grafeno emite armónicos de orden alto. Estimaron la producción de frecuencias de hasta 5-10 THz, abriendo así la puerta a las aplicaciones del grafeno en la electrónica de terahercios. Ishikawa et al. [43] estudiaron la dinámica de la generación de armónicos usando ecuaciones ópticas de Bloch, analizando la interacción entre la dinámica intrabanda e interbanda en los puntos de Dirac. Tres años después, se reportó por primera vez la generación del tercer armónico en grafeno [44]. Finalmente, en 2017 Taucer et al. [45] y Yoshikawa et al. [30] produjeron armónicos no perturbativos hasta el quinto y noveno orden (ver Fig. 2.7), demostrando experimentalmente por primera vez el proceso de HHG en grafeno de una sola capa. Confirmaron la predicción de la alta eficiencia del proceso y también reportaron la dependencia de la intensidad de los armónicos con la polarización del campo incidente, consecuencia de la anisotropía no lineal del grafeno.

Durante las dos últimas décadas, la combinación de todas las propiedades enumeradas anteriormente ha motivado la elección del grafeno como sustituto de otros materiales en aplicaciones ya existentes. De hecho se utiliza en una amplia gama

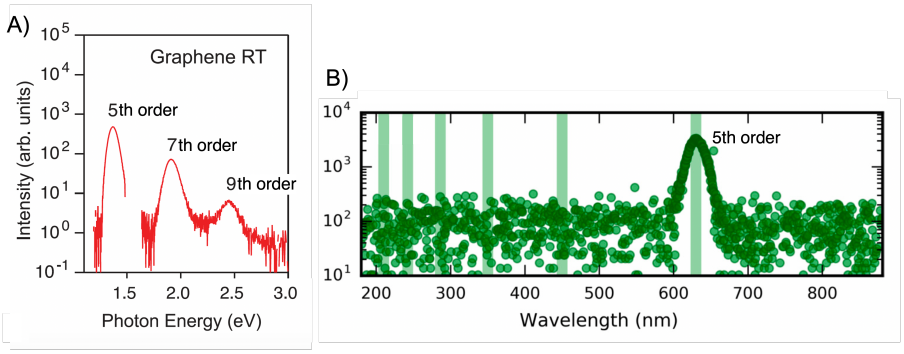

FIGURE 2.7: Primeros espectros de armónicos de orden elevado obtenidos en grafeno monocapa. En el panel A), presentamos el resultado de Yoshikawa et al. (figura adaptada de [30]), alcanzando hasta el noveno orden armónico a partir de un l-aser centrado en 0.26 eV ($\sim 4.8\mu m$). En el panel B), el espectro de Taucer et al. (figura adaptada de [45]), donde se observa el quinto orden armónico generado a partir de un láser de longitud de onda de $3.1\mu m$.

de campos, desde el soporte de nanoobjetos para microscopía electrónica de transmisión (TEM, de sus siglas en inglés) [46], el uso en células solares como recubrimiento conductor transparente [47], hasta como transistor para aplicaciones de alta frecuencia [48]. Sin embargo, la mayoría de las aplicaciones exigen la producción de láminas de gran superficie, más allá del tamaño micrométrico. El método de producción industrial más extendido es la deposición química de vapor (CVD, de sus siglas en inglés). Desafortunadamente, las capas individuales de grafeno obtenidas en la producción en masa son policristales (ver Fig. 2.8). Por lo tanto, los estudios de HHG en grafeno policristalino son de alto interés.

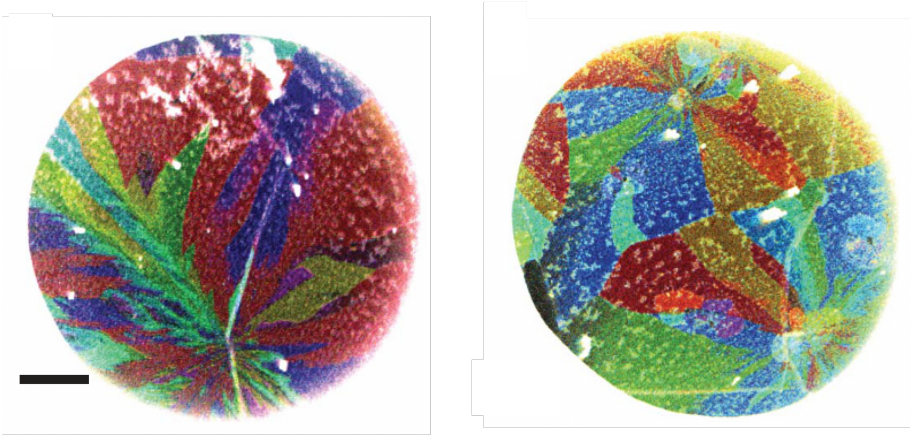

FIGURE 2.8: Imágenes de diferentes regiones en una muestra de grafeno policristalino generadas por CVD. Ambas imágenes se obtienen mediante una técnica de microscopía electrónica llamada microscopía electrónica de transmisión de campo oscuro (DF-TEM). La imagen de granos da colores falsos para distinguir las formas y orientaciones. La barra de escala es de 500 nm. Figura extraída de [49]

2.1 Objetivos de esta tesis y publicaciones

La principal motivación de esta tesis es contribuir al estudio de los aspectos fundamentales de la generación de armónicos de orden elevado en grafeno monocapa. Tomando como punto de partida los estudios previos sobre la teoría microscópica de HHG en grafeno, como la Ref. [40], nos hemos centrado en la exploración de la respuesta macroscópica para abordar situaciones próximas a los experimentos [30, 45, 50]. Esta tesis contiene los resultados publicados en las siguientes referencias:

1. Referencia [51]. R. Boyero-García, O. Zurrón-Cifuentes, L. Plaja, C. Hernández-García, Transverse phase-matching of high-order armonic generation in single-layer graphene. *Opt. Express* **29**, 2488–2500 (2021). Si bien el grafeno monocapa es un material 2D y la propagación longitudinal no juega un papel en la emisión final de armónicos, el ajuste de fase en la superposición de las emisiones locales en el plano del grafeno sí presenta un papel fundamental. El llamado *acuerdo de fase transversal* ha sido estudiado en HHG en medios gaseosos, pero en este trabajo lo analizamos por primera vez en un sólido. Nuestros resultados determinan que, debido al acuerdo de fase transversal, la emisión de armónicos resultante de la capa de grafeno está dominada por un anillo alrededor del eje de propagación del haz incidente.

2. Referencia [52]. R. Boyero-García, A. García-Cabrera, O. Zurrón-Cifuentes, C. Hernández-García, L. Plaja, Non-classical high harmonic generation in graphene driven by linearly polarized laser pulses. *Opt. Express* **30**, 15546–15555 (2022). Desde un punto de vista semiclásico, se sabe que el número de trayectorias electrónicas que tienen lugar en el proceso de HHG en grafeno de una sola capa es mucho mayor que en sólidos de *gap* finito. Esto es debido al reemplazo de la excitación túnel por la excitación no adiabática cerca de los puntos de Dirac. Resultados recientes de HHG en sólidos gruesos [53, 54] han demostrado que las trayectorias no clásicas son relevantes en la construcción del espectro final de HHG. En este artículo hemos demostrado el papel relevante de estas trayectorias no clásicas en el espectro de armónico generado en grafeno.

3. Referencia [55]. R. Boyero-García, A. García-Cabrera, O. Zurrón-Cifuentes, C. Hernández-García, L. Plaja, High-order harmonic spectroscopy of polycrystalline graphene. *Opt. Mater. Express* **12**, 3543–3550 (2022). La deposición química de vapor es una de las técnicas más populares para obtener grandes áreas de grafeno, requerida para la mayoría de las aplicaciones industriales. Esta técnica, sin embargo, produce policristales con diferentes tamaños de dominio y orientaciones. Para caracterizar la estructura policristalina, es decir, para proporcionar las distribuciones de tamaños y orientaciones, proponemos explorar la respuesta anisotrópica no lineal del grafeno a campos láser intensos. En este trabajo presentamos simulaciones de HHG en grafeno policristalino, con un estudio de la dependencia de la polarización de los armónicos frente al tamaño y la orientación de los policristales.

Los artículos anteriores toman como punto de partida resultados previos obtenidos a lo largo de la tesis donde el estudiante participa también como coautor:

1. Referencia [56]. O. Zurrón-Cifuentes, R. Boyero-García, C. Hernández-García, A. Picón, L. Plaja, Optical anisotropy of non-perturbative high-order harmonic generation in gapless graphene. *Opt. Express* **27**, 7776–7786 (2019). En este trabajo estudiamos la influencia de la simetría del grafeno en la emisión de armónicos. La respuesta óptica no lineal conduce a la generación de armónicos con polarización elíptica o circular cuando es inducida por un campo eléctrico polarizado linealmente.

2. Referencia [57]. O. Zurrón-Cifuentes, R. Boyero-García, C. Hernández-García, L. Plaja, High harmonic generation in armchair carbon nanotubes. *Opt. Express* **28**, 19760–19771 (2020). Para explorar el proceso de HHG en nuevas configuraciones de alótropos de carbono, resolvimos numéricamente el proceso en nanotubos de carbono. Nos enfocamos en la emisión de tipo sillón con índice quiral (n, n) irradiada por un láser mid-IR.

Chapter 3

Fundamentals

In this chapter we shall review fundamental concepts needed to contextualize the research carried on during this thesis. We will first review the phenomena of HHG from atomic gas targets. As commented in the previous chapter, the first experiments in HHG were carried at using noble gas jets as targets. These targets are not subjected to damage limitations, therefore allowing to explore comfortably the strong field interaction regime. In addition, the low reactivity of noble gases is also an advantage when manipulated in vacuum chambers. Interestingly, the bound-state dynamics does not play a relevant role in HHG from atoms. Therefore, the subject can be introduced straight away, without a need of presenting particular topics of atomic physics. The situation changes, however, in the case of solids, where the description of the electron dynamics is of paramount importance. Therefore, the section presenting the fundamentals of HHG from graphene will also include the description of the matter system. In both cases, atoms and solids, we will also introduce the details of the build-up of the harmonic signal from macroscopic targets.

3.1 The microscopic description of high-order harmonic generation in atoms

The understanding of HHG requires addressing two different levels. On one side, the microscopic description considers the harmonic emission of an elemental radiator in the target. At this level, the amplitude of the driving field is assumed spatially constant, and the effort is focused into the understanding of the non-linear response of the target species. Once the microscopic description is developed, the macroscopic

point of view studies the collective emission of the elementary emitters, distributed along the target and, therefore, exposed to different local values of the driving field amplitude.

When an intense laser field interacts with a target, it can induce a strong non-linear, non-perturbative, process that may result in the emission of harmonics. In the traditional approach, the optical non-linear response of a medium to an intense electric field of frequency ω_0 is described by the polarization density, as a perturbative series of the incident field of the form

$$\boldsymbol{P} = \chi^{(1)}\left(-\omega_0, \omega_0\right)\boldsymbol{F} + \chi^{(2)}\left(-2\omega_0, \omega_0\right)\boldsymbol{F}^2 + \chi^{(3)}\left(-3\omega_0, \omega_0\right)\boldsymbol{F}^3 + ..., \tag{3.1}$$

where $\chi^{(n)}\left(-n\omega_0, \omega_0\right)$ is the nth-order non-linear susceptibility and $\boldsymbol{F}$ is the external field amplitude. The quantum theory of the non-linear light-matter interactions was described by Maria Goepper-Mayer in 1931, in her doctoral dissertation [58]. However, it was not until one year after the invention of the laser in 1960, when the generation of the second-harmonic of a driving field was experimentally reported in crystalline quartz [59]. Soon afterwards, in 1962, the generation of the third harmonic was reported from calcite [60]. The mechanism described by the perturbative series 3.1 corresponds to the multiphoton excitation of matter, where the order in the series corresponds to the number of photons involved in the process. Since the probability of combining a set of photons decreases with its number, the efficiency of the multiphoton process drops with the harmonic order. When the laser intensity is high enough, the process becomes non-perturbative, and the expansion 3.1 is not longer valid. Driving field intensities of about 10^{13} to 10^{15} W/cm^2 are strong enough to inject the atomic electron into the continuum via tunnel ionization. In this case, the ionization rate increases with respect to the multiphoton absorption, and the high-order harmonics are generated more efficiently. This regime was experimentally tested in 1989 by Huillier et al. in Ar, Kr and Xe [8] when they noted that the harmonic spectrum departed from the monotonous descending intensity trend. As it was already introduced in this thesis work, the strong-field harmonic spectrum can be separated into three different regions (see Fig. 3.1): an exponential decrease for the lower order harmonics, followed by several harmonics with similar intensity,

known as *plateau*, and a abrupt cutoff frequency that limits the maximum harmonic-order radiated. The law describing the cutoff frequency, ω_{max}, was first identified in [9] from numerical simulations, and is given by:

$$\hbar\omega_{max} = I_p + 3.17U_p, \tag{3.2}$$

being I_p the ionization energy and U_p the cycle-averaged kinetic energy of a free electron in presence of a electromagnetic field, also known as the ponderomotive energy. For a monochromatic driving field, the ponderomotive energy is given by $U_p = q_e^2F^2/4m_e\omega_o^2$ where q_e and m_e are the electron charge and mass, respectively, and F_o the driving field amplitude. For centrosymmetric targets, such as noble gas atoms, the even-order susceptibilities are zero, therefore HHG produces a frequency comb with only odd-order harmonics.

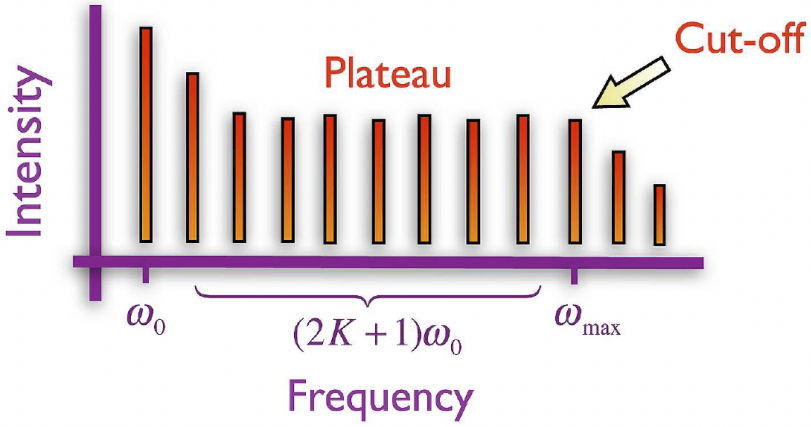

FIGURE 3.1: Basic structure of a HHG spectrum with the three characteristic stages as: an exponential decrease in intensity at low-order harmonics, followed by an extended intensity *plateau*, until a certain cutoff frequency where the intensity decreases again. For centrosymmetric targets, HHG spectrum is typically composed by odd harmonic orders (K is a positive integer). Figure extracted from [61].

3.1.1 Semiclassical approach

In order to explain intuitively mechanism behind HHG in gases, the most extended theory is the so-called *three-step model* [5, 62] explained previously in section 1. According to it, harmonics are radiated upon rescattering of electrons with the parent

ion. This process repeats twice every cycle i.e. once per maximum of the field amplitude, and structures the harmonic emission into a train of high-frequency XUV pulses. This periodicity, together with the symmetry of the target, determines the line-spacing between the harmonics in the frequency comb. As already introduced, centrosymmetric targets typically result in odd-order harmonics, but the use of polichromatic driving pulses may lead to the appearance of even-order (or more complex) harmonic distributions [63–65].

Assuming that the ionized-electron wave packet behaves as a semiclassical charged particle accelerated by the external field, we can analyze the electron trajectories that lead to the HHG emission. Note that in the tunnel ionization regime the electron is released into the continuum with a mean value of zero velocity. In this situation, a linearly polarized field can only drive the electron back and forth, optimizing the efficiency of the re-encounters with the parent atom. Neglecting the influence of the Coulomb potential and the effect of the magnetic field during the electron excursion in the continuum, we can integrate the equation of motion of the free electron interacting with a monochromatic field, linearly polarized in the y axis, $F(t) = F_o \sin \omega_0 t$, as follows:

$$\ddot{y} = \frac{q_e F_o}{m_e} \sin \omega_0 t, \tag{3.3}$$

$$\dot{y} = -\frac{q_e F_o}{m_e \omega_0} \left[\cos \omega_0 t - \cos \omega_0 t_o\right], \tag{3.4}$$

$$y = -\frac{q_e F_o}{m_e \omega_0^2} \left[\sin \omega_0 t - \sin \omega_0 t_o - \omega_0 \left(t - t_o\right) \cos \omega_0 t_o\right], \tag{3.5}$$

where t_0 is the time when the electron is ionized. Following the *three-step model* description, the frequency of the emitted harmonic corresponds to the kinetic energy at recollision time plus the ionization potential I_P. Accordingly, the maximum frequency radiated, i.e. the frequency cutoff, corresponds to the maximum kinetic energy on recollision among all the recolliding trajectories.

Figure 3.2a, illustrates the above discussion by showing a set of electron trajectories born in the continuum at different ionization times. The trajectories are obtained from Eqs. 3.3-3.5. The electric field is represented by the grey-dashed line and the

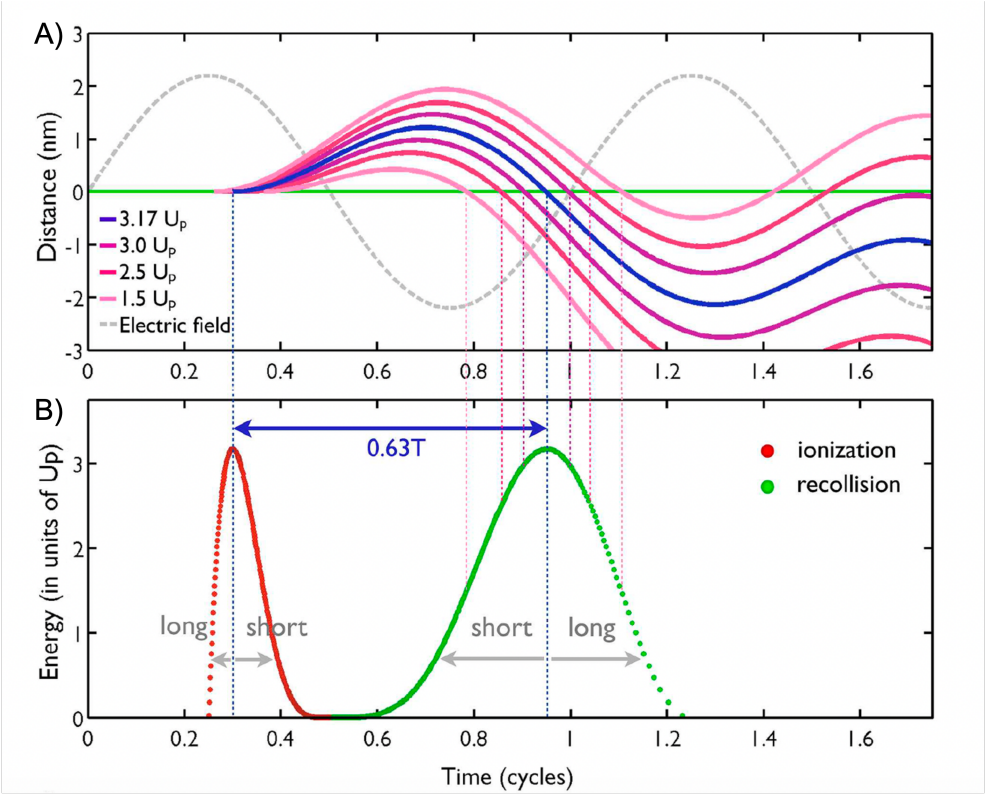

FIGURE 3.2: A) Classical trajectories in time calculated for a monochromatic laser field centered at 800 nm and a peak intensity 1.57×10^14 W/cm^2. Light green line represent the atom position, while the dashed grey line is the driving field. Blue line is the trajectory with the maximum recollision energy, i.e. cutoff and the three pairs of continuous lines represent the trajectories corresponding to 3.0 U_P, 2.5 U_P and 1.5 U_P energies. B) Ionization (red dots) and recollision (green dots) energies in time. *Short* and *long* trajectories distribution in both energy spikes are highlighted. The excursion time of the cutoff trajectory is 0.63 T, where T is the laser period. Figure extracted from [61]

green line shows the position of the atom. Only a subset of trajectories is represented, corresponding to those that rescatter with the parent ion. Note the fortunate coincidence of these trajectories being ionized near the driving field amplitude maximum, therefore with greater tunnel probability. As a consequence, the rescattering trajectories, leading to the emission oh harmonics, are also those more efficiently ionized.

Fig. 3.2b shows the kinetic energy at rescattering as a function of the ionization (red) and recollision (green) times of the corresponding trajectories. Note that those trajectories ionized slightly after the field amplitude maximum rescatter with energies close to the frequency cutoff $3.17Up$. A single trajectory fulfills this maximal energy condition, plotted as a blue line in Fig. 3.2a. In contrast, there is always a pair

of trajectories with the same recollision energy below the cutoff (e.g. $3.0U_P$,$2.5U_P$ and $1.5U_P$ cases presented in pink tones in Fig. 3.2). These trajectories differ in the ionization and rescattering times, and therefore spend different times during their excursion through the continuum. According to the duration of their excursion, they are termed as *short* and *long* trajectories. Lewenstein et al. in 1994 [66] gave the first glimpse to the semiclassical nature of the electron wave packet trajectories, in particular to the phase acquired by the wave function during the electron's excursion. The relative phase between the trajectories generates interference patterns in the harmonic spectra, that were first found experimentally in 2008 [67]. According to Lewenstein's description, this quantum phase is more sensitive to the driving field intensity the longer the trajectory's excursion is. As we shall study, this will be very relevant to understand the macroscopic build-up of the harmonic emission.

3.1.2 Quantum approach: Exact solution

HHG can be well described within the single active electron approximation (SAE), where the electron is assumed to interact with the electric field and the atomic core is frozen. The dynamics of the electron wave function, $\Psi(\boldsymbol{r},t)$, is ruled by the time-dependent Schrödinger equation (TDSE)

$$i\hbar\frac{\partial}{\partial t}\Psi(\boldsymbol{r},t) = H(\boldsymbol{r},t)\,\Psi(\boldsymbol{r},t)\,, \tag{3.6}$$

where $H(\boldsymbol{r},t)$ is the Hamiltonian describing the electron interaction with the ion and the electromagnetic field. Under the dipole approximation, the electromagnetic field is approximated as homogeneous, therefore

$$H(\boldsymbol{r},t) = T + V_C(r) + V_F(t), \tag{3.7}$$

where $T = -\frac{\hbar^2}{2m_e}\nabla^2$ is the kinetic energy operator, $V_C(r)$ the core's Coulomb potential, and $V_F(t) = -i\frac{q_e\hbar}{m_e c}\boldsymbol{A}(t)\cdot\nabla + \frac{q_e^2}{2m_e c^2}\boldsymbol{A}^2(t)$, $\boldsymbol{A}(t)$ being the electromagnetic vector potential. The integration of 3.6 is usually carried by means of the Crank-Nicolson algorithm [68]. According to Larmor's formula [69], the electron will emit an electromagnetic field proportional to its acceleration. The harmonic spectrum is, then,

computed as the Fourier transform of the mean value of the electron acceleration, $\boldsymbol{a}(t) = \langle -(q_e/m_e)\nabla V_C \rangle_{\Psi(t)}$. Fig 3.3 shows the harmonic spectrum corresponding to the dynamics of an electron initially occupying the ground state of a hydrogen atom. The electromagnetic field is modelled as a 16-cycle long sin^2 envelope pulse with center wavelength 800 nm and peak intensity 1.48×10^{14} W/cm^2. Note the emergence of the *plateau* structure, that extends approximately to the 27th order, in good agreement with the semiclassical cutoff formula 3.2.

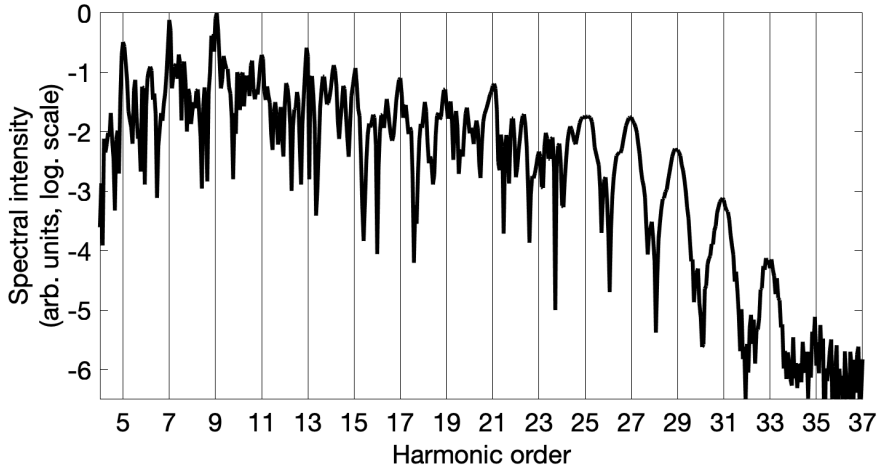

FIGURE 3.3: TDSE simulation results of the HHG spectrum in atomic hydrogen driven by a 800 nm, 16 cycles (total duration) and 1.48×10^{14} W/cm^2 peak intensity pulse.

Time-frequency analysis

In order to analyze the temporal characteristics of the harmonic emission it is very useful to develop a time-frequency analysis (TFA) of the harmonic signal. This diagnostic allows to resolve which harmonics are emitted at the different instants of time during the interaction. The TFA uses the harmonic spectrogram, obtained from the inverse Fourier Transform of the time-gated acceleration,

$$S_\sigma(\omega, \tau) = \frac{1}{\sqrt{2\pi}} \int_{-\infty}^{\infty} g_\sigma(t - \tau) a(t) e^{i\omega t} dt \tag{3.8}$$

where g_σ is a Gaussian function of width σ.

Fig 3.4 shows the spectrogram corresponding to the harmonic spectrum plotted in Fig. 3.3. The harmonic frequencies corresponding to the semiclassical trajectories

are superimposed as red and black circles, corresponding to the *short* and *long* trajectories, respectively. It is appealing the coincidence between the classical predictions and the TFA, which demonstrates the success of the semiclassical description even in the description of the spectral region well below the cutoff frequency.

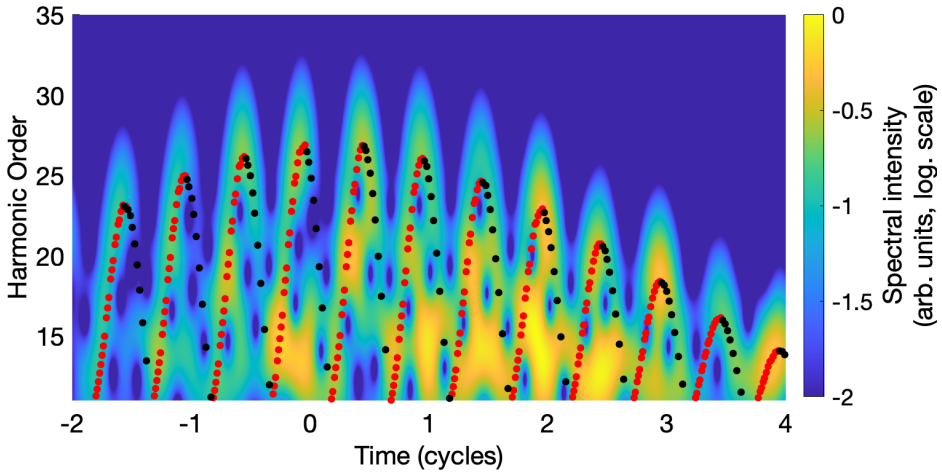

FIGURE 3.4: TFA of the HHG emission obtained in hydrogen atom using a driving laser pulse with $1.48\times10^{14}\ W/cm^2$ peak intensity, centered at 800 nm and 16-cycle total duration pulse. The TFA has been obtained scanning over the HHG spectral amplitudes with a Gaussian mask of $3\omega_0$ width. Red (black) dots represent the semiclassical results from *short* (*long*) classical trajectories.

3.1.3 Quantum approach: The Strong-Field Approximation

The integration of the TDSE in Eq. 3.6 provides the exact solution of the wave packet dynamics but, at the same time, it can be very computing-time demanding. This inconvenience is overcome with the use of simplified models, based on reasonable approximations. Among them, the Strong-Field Approximation (SFA) has been demonstrated very successful in the description of relevant strong-field phenomena, as above-threshold ionization or HHG [70–72]. The SFA neglects the Coulomb potential once the electron evolves in the continuum. The SFA approach is developed through the definition of Green's propagators of the complete and partial forms of the Hamiltonian. The solution of the TDSE 3.6 is given in terms of the Green's function, $G(\boldsymbol{r},t;\boldsymbol{r}_i,t_0)$, associated to the Hamiltonian 3.7 as,

$$\Psi(\boldsymbol{r},t) = i\int G(\boldsymbol{r},t;\boldsymbol{r_i},t_0)\,\Psi(\boldsymbol{r_i},t_0)\,d\boldsymbol{r}_i, \tag{3.9}$$

or, in Dirac notation,$|\Psi(t)\rangle = iG(t,t_0)\,|\Psi(t_0)\rangle$.

The SFA is developed considering two possible splittings of the total Hamiltonian 3.7. On one hand $H = H_A + V_F(t)$, with $H_A = T + V_C(\boldsymbol{r})$ being the atomic Hamiltonian, can be interpreted as describing an atomic electron interacting with an electric field. On the other hand, the splitting $H = H_F(t) + V_C$, with $H_F(t) = T + V_F(t)$, describes the field-assisted electron scattering with the ion potential. According to these definitions, we can define the Green's functions associated with the partial Hamiltonians H_A and $H_F(t)$ as $G_A(t,t_0)$ and $G_F(t,t_0)$ respectively. $G_A(t,t_0)$ propagates an atomic electron free from the interaction with the electric field, whereas $G_F(t,t_0)$ propagates a free electron quivering under the influence the electric field.

The exact calculation of the the Green's function $G(t,t_0)$ is too complex, therefore requires the development of approximations. One general strategy to approximate Green's propagators consist in considering the Lippmann-Schwinger expansion that, for the two Hamiltonian splitting considered above, reads as,

$$G(t,t_0) = G_A(t,t_0) + \frac{1}{\hbar}\int_{t_0}^{t} G(t,t_1)\,V_I(t_1)\,G_A(t_1,t_0)\,dt_1 \tag{3.10}$$

$$G(t,t_0) = G_F(t,t_0) + \frac{1}{\hbar}\int_{t_0}^{t} G(t,t_1)\,V_C(t_1)\,G_F(t_1,t_0)\,dt_1 \tag{3.11}$$

Note that these are not approximations, as the right-hand sides depend also on the final solution $G(t,t_0)$. In it most common form, the SFA substitutes the exact propagator inside the integral in Eq. 3.10 by the first term in the expansion 3.11, resulting in the approximated expression:

$$G(t,t_0) \simeq G_A(t,t_0) + \frac{1}{\hbar}\int_{t_0}^{t} G_F(t,t_1)\,V_I(t_1)\,G_A(t_1,t_0)\,dt_1. \tag{3.12}$$

The physical reading of this expression is the following: the evolution results from the superposition of different stories that may happen to the electrons. The first term in 3.12 describes the possibility that the electron evolves in the atom, without interaction with the electric field. The integral term, on the other side, describes the sum of all stories in which the electron evolves in the atom until a certain time, t_1, in which the interaction happens. Afterwards, the electron evolves as a free particle in

the electric field without noticing the Coulomb potential of the ion.

Now we can write the temporal evolution of the electronic wave function using the SFA propagator 3.12 as

$$\begin{aligned} |\Psi(t)\rangle &= iG_A(t,t_0)|\psi_0\rangle + \frac{i}{\hbar}\int_{t_0}^{t} G_F(t,t_1)\,V_F(t_1)\,G_A(t_1,t_0)\,|\psi_0\rangle\,dt_1 \\ &= |\psi_0(t)\rangle + |\delta\psi(t)\rangle, \end{aligned} \tag{3.13}$$

where $|\psi_0\rangle$ is the initial state of the electron, that we shall assume as the atomic ground state. The first term of the right part refers to the electron evolving solely under the Coulomb potential, then

$$|\psi_0(t)\rangle = iG_A(t,t0)\,|\psi_0\rangle = e^{-i\epsilon_0(t-t_0)/\hbar}\,|\psi_0\rangle, \tag{3.14}$$

where ϵ_0 is the energy of the state. For the integral term in 3.13 we introduce the Volkov states, the basis for describing the interaction between strong laser pulses and a free electron:

$$|\Psi_{\boldsymbol{P}}(t)\rangle = e^{i\frac{1}{\hbar}S(\boldsymbol{P},t,t_1)}\,|\boldsymbol{P}\rangle, \tag{3.15}$$

where $\langle \boldsymbol{r}|\boldsymbol{P}\rangle = e^{i/\hbar[\boldsymbol{P}-q_e/c\boldsymbol{A}(t)]\cdot\boldsymbol{r}}$, $\boldsymbol{P}$ being the canonical momentum, and $S(\boldsymbol{P},t,t_1)$ the free electron action given by

$$S(\boldsymbol{P},t,t_1) = -\frac{1}{2m_e}\int_{t_1}^{t}\left[\boldsymbol{P}-\frac{q_e}{c}\boldsymbol{A}(t')\right]^2 dt'. \tag{3.16}$$

Using the Volkov states, the Green's function G_F results in

$$G_F(\boldsymbol{r},t;\boldsymbol{r_1},t_1) = -i\int e^{i\frac{1}{\hbar}S(\boldsymbol{P},t,t_1)}\,|\boldsymbol{P}\rangle\,\langle\boldsymbol{P}|\,d\boldsymbol{P}. \tag{3.17}$$

Introducing Eq. 3.17 in the second term in Eq. 3.13, we obtain

$$\begin{aligned} |\delta\psi(t)\rangle &= -\frac{i}{\hbar}\int\int_{t_0}^{t} e^{i\frac{1}{\hbar}S(\boldsymbol{P},t,t_1)}e^{-i\frac{\epsilon_0}{\hbar}(t_1-t_0)}\,\langle\boldsymbol{P}|\,V_F(t_1)\,|\psi_0\rangle\,dt_1\,|\boldsymbol{P}\rangle\,d\boldsymbol{P} \\ &= \int\psi(\boldsymbol{P},t)\,|\boldsymbol{P}\rangle\,d\boldsymbol{P} \end{aligned} \tag{3.18}$$

We can solve $\psi(\boldsymbol{P},t)$ using a standard Runge-Kutta algorithm for the differential equation:

$$\frac{d}{dt}\psi(\boldsymbol{P},t) = -\frac{i}{2m_e\hbar}\left[\boldsymbol{P} - \frac{q_e}{c}\boldsymbol{A}\left(t'\right)\right]^2\psi(\boldsymbol{P},t) - \frac{i}{\hbar}e^{-i\frac{\epsilon_0}{\hbar}(t-t_0)}\left\langle\boldsymbol{P}\right|V_F(t_1)\left|\psi_0\right\rangle. \quad (3.19)$$

Once we have obtained the temporal evolution of the electron wave function, the acceleration of the electron can be expressed following Eq. 3.13 as

$$\langle\boldsymbol{a}(t)\rangle = \langle\psi_0(t)|\,\boldsymbol{a}\,|\psi_0(t)\rangle + \langle\delta\psi(t)|\,\boldsymbol{a}\,|\delta\psi(t)\rangle + 2\Re\left\{\langle\psi_0(t)|\,\boldsymbol{a}\,|\delta\psi(t)\rangle\right\}. \quad (3.20)$$

The first term in the right hand vanishes due to the parity of the atomic orbitals. The second term stems from the free electron oscillation due to a external field interaction. This term is mainly linear, therefore not relevant for HHG. The last one represents the acceleration of the dipole formed between the ionized electron and the ground state. Using the Ehrenfest theorem, the SFA acceleration operator can be expressed as,

$$\langle\boldsymbol{a}(t)\rangle = 2\Re\left\{\frac{1}{m_e}\langle\psi_0(t)|\left(-\nabla V_C\right)|\delta\psi(t)\rangle\right\} - \frac{q_e}{m_e}\boldsymbol{F}(t), \quad (3.21)$$

and using the information in Eq. 3.18

$$\begin{aligned}\langle\boldsymbol{a}(t)\rangle &= \int 2\Re\left[\frac{1}{m_e}\langle\psi_0(t)|\left(-\nabla V_C\right)|\boldsymbol{P}\rangle\right.\\ &\left.\times\left\{-\frac{i}{\hbar}\int_{t_0}^{t}e^{i\frac{1}{\hbar}S(\boldsymbol{P},t,t_1)}e^{i\frac{\epsilon_0}{\hbar}(t-t_1)}\left\langle\boldsymbol{P}\right|V_F(t_1)\left|\psi_0\right\rangle dt_1\right\}\right]d\boldsymbol{P}\\ &= \int a(\boldsymbol{P},t)\,d\boldsymbol{P}. \end{aligned} \quad (3.22)$$

Fig. 3.5, extracted from [73], shows a comparison between TDSE (blue line) and SFA (red line) spectrum results for a 6-cycles total duration driving field with $1.58\times 10^14 W/cm^2$ peak intensity and centered at 1600nm. The differences between the exact solution given by the TDSE, and the SFA are demonstrated to be minimal.

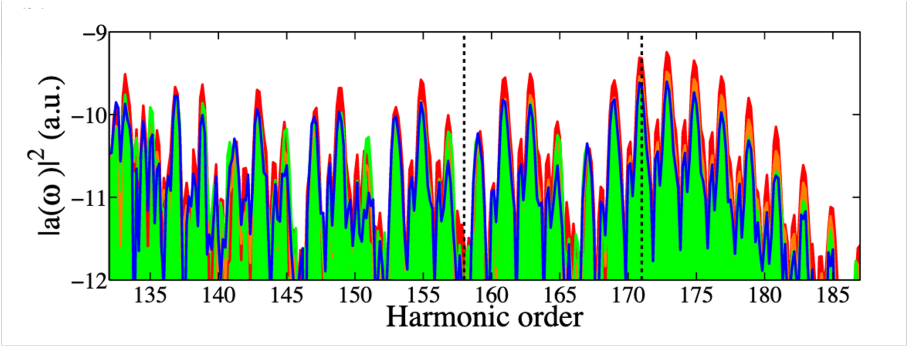

FIGURE 3.5: High-order harmonic spectra obtained with a driving pulse of 6 cycles total duration, 1.58×10^{14} W/cm^2 peak intensity and centered at 1600nm. Blue (red) line corresponds to the TDSE (SFA) results, while orange and green lines are different approximations not explained in this thesis work. Figure extracted from [73].

3.2 The macroscopic description of high-order harmonic generation in atoms

Once we have discussed the different approaches for HHG in gases from a single atom perspective, we can move on to the macroscopic point of view. This requires the evaluation of the total emission of the atoms in the target, each subjected to the local form of the driving field.

3.2.1 Phase-matching

Previously we commented on the relevance of the quantum phase acquired in the trajectories' excursions. Then we determined the harmonic acceleration formula under the SFA, and how it contained a phase term given by the action $S(\boldsymbol{P}, t, t_1)$. This phase is transmitted to the harmonics as the exponential of the action associated to each semiclassical trajectory with rescattering kinetic energy $q\hbar\omega_0 - |\epsilon_0|$, q being the harmonic order. Thus, the phase of the qth-order harmonic can be split in two parts as,

$$\varphi_q^n(\rho, \phi, z) = q\Phi(\rho, \phi, z) + \alpha_q^n I(\rho, \phi, z), \tag{3.23}$$

(ρ, ϕ, z) being the cylindrical coordinates of the position of a particular atom in the sample, and n ="s" or "l" labels the *short* or *long* nature of the trajectory considered. The first term in 3.23 is the qth multiple of the local value of the driving field's

phase $\Phi(\rho, \phi, z)$. This harmonic phase coincides with the expected from perturbation theory. The second term in Eq. 3.23 represents a non-perturbative addition to the harmonic phase, that depends on the local value of the driving field's intensity $I(\rho, \phi, z)$. The proportionality constants α_q^n depend on the harmonic order and on the nature of the trajectory. The actual values of these constants can be obtained from the SFA approach, combined with a saddle-point approximation. Fig. 3.6 shows the values of α_q^n as a function of the electron's returning energy, as computed for the case of a monochromatic driving field. Note that the sensitivity of the phase to the driver's intensity is larger for *long* trajectories, as α_q^l is always greater than α_q^s.

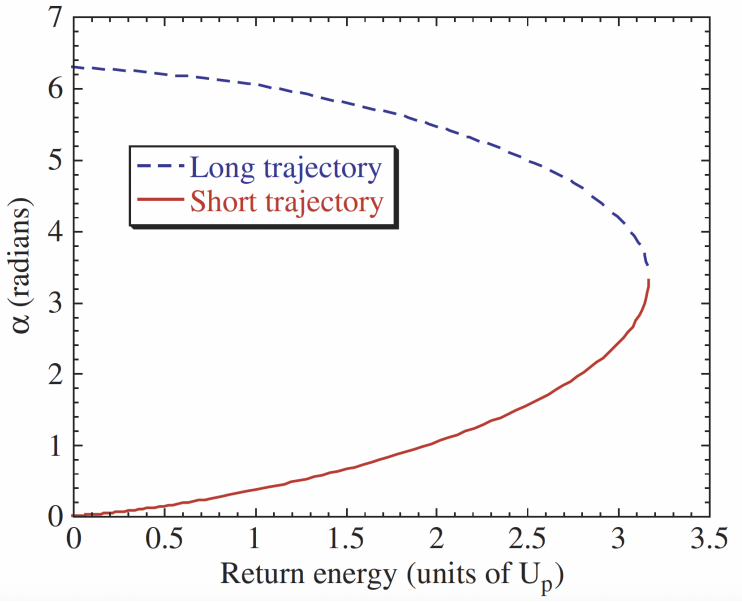

FIGURE 3.6: Numerical result for the phase coefficient α_q^n as a function of electron return energy, in units of U_P. Figure extracted from [15].

Since the macroscopic harmonic signal from the target is the superposition of the emissions from each atom, the optimal signal should be obtained when the phase of these emissions match to build a constructive interference. Considering the atom distribution along the field propagation direction, the phase difference between the harmonic field emitted at z_0 and propagated to z, and that being generated at z is $\Delta\varphi_q^n = \varphi_q^n(z) - \varphi_q^n(z_0) - k_q(z - z_0)$, where k_q is the harmonic wavenumber. At point z the emissions originated at all previous points z_0 present a longitudinal phase

mismatch factor of

$$\Delta k_q^{n,\parallel} = \frac{\partial \Delta \varphi_q^n}{\partial z} = \frac{\partial \varphi_q^n(z)}{\partial z} - k_q = q k_1 + \alpha_q^n \frac{\partial I(z)}{\partial z} - k_q \tag{3.24}$$

where k_1 is the wavenumber of the driving field. Note that up to here we have considered only the quantum phase as the source of harmonic phase difference along the propagation direction. However, in an experiment other sources of phase mismatch are the harmonic dispersion due to the ionized electrons, and the phase acquired by the field focusing geometry. It is common to find these terms in the longitudinal phase mismatch factor in the literature [15].

Additionally to the longitudinal phase dependencies, it is also important to take into account the *transverse phase-matching* [74]. The transverse intensity distribution of the driving field leads to a different non-perturbative phase term in each point of the transversal plane of the HHG emission. In such case, one can define the *transverse phase-mismatch* factor as:

$$\Delta k_q^{n,\perp} = \frac{\partial \varphi_q^n}{\partial \rho} = \alpha_q^n \frac{\partial I(\rho)}{\partial \rho}, \tag{3.25}$$

where ρ is the radial coordinate. As in the longitudinal case, additional terms that take into account the focusing geometry can be considered. It has been demonstrated not only that *transverse phase-matching* is important to improve the HHG efficiency [74], but also to modify the temporal and spatial properties [75, 76]. However, *transverse phase-matching* is well demonstrated in gases but not in solids. One of our results of this thesis is centered in the study of the *transverse phase-matching* in a monolayer graphene, where, due to the layer's atomic thickness, longitudinal phase-matching effects do not play a role.

3.2.2 Computation of macroscopic high-order harmonic emission

In order to obtain the target's emission as if detected in the far field, we follow the method presented in Ref. [61]. We consider the wave equation:

$$\nabla^2 \boldsymbol{F} - \frac{1}{c^2}\frac{\partial^2}{\partial t^2}\boldsymbol{F} = \frac{4\pi}{c^2}\frac{\partial}{\partial t}\boldsymbol{J}, \tag{3.26}$$

where $\boldsymbol{J}$ is the current density and $\boldsymbol{F}(\boldsymbol{r},t) = \boldsymbol{F}_o(\boldsymbol{r},t) + \boldsymbol{F}_i(\boldsymbol{r},t)$, $\boldsymbol{F}_o(\boldsymbol{r},t)$ being the driving field and $\boldsymbol{F}_i(\boldsymbol{r},t)$ the field radiated by the charges in the target. For high

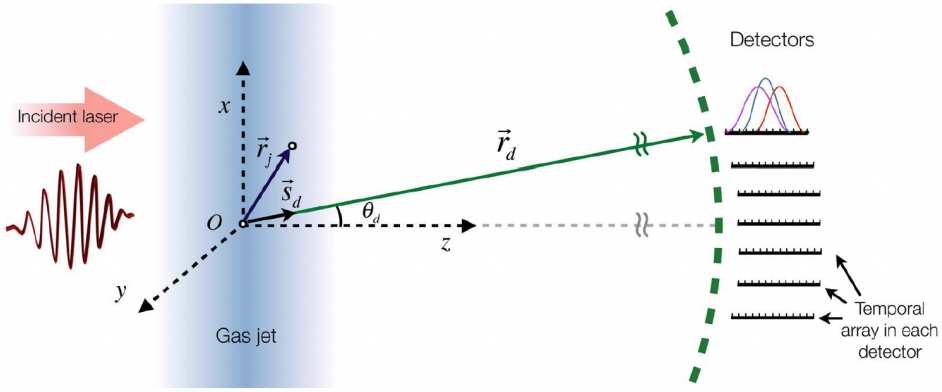

FIGURE 3.7: Scheme of HHG propagation from each emitter placed at $\boldsymbol{r_j}$ to a detector place at a distance $|\boldsymbol{r}_d|$ from the center of the target O. The detector is formed by elementary cells at different angles θ_d where the integrated harmonic emission from all elementary radiators at the target is collected. Figure extracted from [61].

frequencies we can assume propagation at vacuum velocity. Then, the field radiated by a source placed at the point $\boldsymbol{r}'$ in the target propagates to a detector, placed at $\boldsymbol{r}_d$, as,

$$\boldsymbol{F}(\boldsymbol{r}_d,t) = -\frac{1}{c^2}\int d\boldsymbol{r}' \frac{1}{|\boldsymbol{r}-\boldsymbol{r}'_d|}\left[\frac{\partial}{\partial t'}\boldsymbol{J}(\boldsymbol{r}',t')\right]_{t'=t-|\boldsymbol{r}_d-\boldsymbol{r}'|/c} \tag{3.27}$$

Since we decompose the target into elemental radiators, the far-field contribution of the radiator located at $\boldsymbol{r}_j$ is (see Fig. 3.7),

$$\boldsymbol{F}_j(\boldsymbol{r}_d,t) = -\frac{q_j}{c^2}\frac{1}{|\boldsymbol{r}_d-\boldsymbol{r}_j|}\boldsymbol{s}_d \times \left[\boldsymbol{s}_d \times \boldsymbol{a}_j\left(t-|\boldsymbol{r}_d-\boldsymbol{r}_j|/c\right)\right], \tag{3.28}$$

where $\boldsymbol{a}_j$ is the jth charge acceleration (that can be calculated through the TDSE or SFA approaches), and $\boldsymbol{s}_d$ is the unitary vector pointing to a detector at $\boldsymbol{r}_d$. Finally, the total emission by the sample can be written as the superposition of each contributions $\boldsymbol{F}(\boldsymbol{r}_d,t) = \sum_{j=1}^{N}\boldsymbol{F}_j(\boldsymbol{r}_d,t)$. This approaches has been successfully used in HHG in gas targets. In this thesis work we will adapt it to describe macroscopic HHG in single layer graphene.

3.3 High-order harmonic generation in graphene

Due to historical reasons, the theory of HHG has been well-established, and contrasted experimentally, for the case of atomic and gas targets. The previous section overviewed this understanding in order to introduce the main aspects of HHG. In this section we will consider graphene as target. The theory of HHG in solids, in particular in graphene, is much less developed. However it has some common points with the case in gases, and also some of the processes in solids are analogous to those in gases. In the next subsection we shall review the structural description of graphene, and its more relevant aspect for HHG: the energy band dispersion. After this, we shall finish this section exposing the theoretical method we have used in this thesis to compute HHG from graphene layers.

3.3.1 Crystal structure

Carbon atom is one of the most abundant elements on earth, and it has the ability to form multiple geometrical configurations with different properties. Carbon allotropes appear in four effective dimensions: 3D bulk systems (as diamond or graphite), 2D layers (as graphene), *quasi* 1D structures (as nanotubes) and 0D (as nanodots) [34]. Carbon structures have extraordinary electrical, optical and mechanical properties due to the presence of strong bonds made from *sp* orbitals hybridizations. Diamond is one of the most known allotropes due to its hardness and high refractive index, with an optical transparency from the infrared to the ultraviolet. Carbon bonds in diamonds are sp^3 hybridizations leading to a three-dimensional crystal structure. In contrast, graphene has an hexagonal structure formed by sp^2-orbital bonds that lead to properties completely opposed to diamonds. Graphite is formed by stacked layers of graphene following an AB sequence, and with delocalized p-orbitals. As a result, graphite is a good electrical conductor in the layer directions.

The upper valence and lower conduction bands in graphene are formed by out-of-plane π and $\pi*$ bonds. Graphene's hexagonal lattice is formed by two sub-lattices

(see Fig. 3.8a), defined by the translation vectors,

$$\boldsymbol{a}_1 = a(\sqrt{3}/2, 1/2, 0), \tag{3.29}$$

$$\boldsymbol{a}_2 = a(\sqrt{3}/2, -1/2, 0), \tag{3.30}$$

where a = 2.46 Å is the lattice constant. Thus, any lattice vector is defined as $\boldsymbol{R}_{n_1,n_2} = n_1\boldsymbol{a_1} + n_2\boldsymbol{a_2}$, where n_1 and n_2 are integers. There are in total 12 point group symmetry operations associated with the hexagonal lattice, six under rotation by angles of $2\pi/n$ with $n = 1 \dots 6$, and six under reflection.

The first Brillouin zone (see Fig. 3.8 b) is defined by the vectors in reciprocal lattice,

$$\boldsymbol{b_1} = 2\pi/a(1/\sqrt{3}, 1, 0), \tag{3.31}$$

$$\boldsymbol{b_2} = 2\pi/a(1/\sqrt{3}, -1, 0), \tag{3.32}$$

Therefore any reciprocal lattice vector can be expressed as $\boldsymbol{G}_{m_1,m_2} = m_1\boldsymbol{b}_1 + m_2\boldsymbol{b}_2$. This results in an hexagonal lattice rotated 90° with respect to that in real space. The six vertices, labeled as K and K', are points where both valence and conduction bands are in contact (Dirac points). The symmetry operations are the same for real and reciprocal spaces. The highest symmetry point is at the center, denoted by $\Gamma = (0, 0)$, dihedrical group D_{6h}. Then we have the Dirac points $K = \frac{4\pi}{3a}(\frac{\sqrt{3}}{2}, \frac{1}{2})$ and $K' = \frac{4\pi}{3a}(\frac{\sqrt{3}}{2}, -\frac{1}{2})$, dihedrical group D_{3h}, and point $M = \frac{2\pi}{\sqrt{3}a}(1, 0)$, dihedrical group D_{2h}. Besides, we can establish the symmetry lines $\Gamma - K$, $\Gamma - M$ and $K - M$ [77].

3.3.2 The band structure of graphene

In the previous section we have seen that the accurate description of the electron's evolution in the continuum is paramount to understand HHG from atoms. We shall see that in the case of crystals the electrons are promoted to the conduction bands, instead of being ionized (see Fig. 1.5). In this case, the electron evolution in the conduction band plays a role of similar importance as that of the ionized electron in atoms. Interestingly, solids add a new degree of complexity, as the energy dispersion is far more intricate in comparison to the parabolic form of the free electron. Before

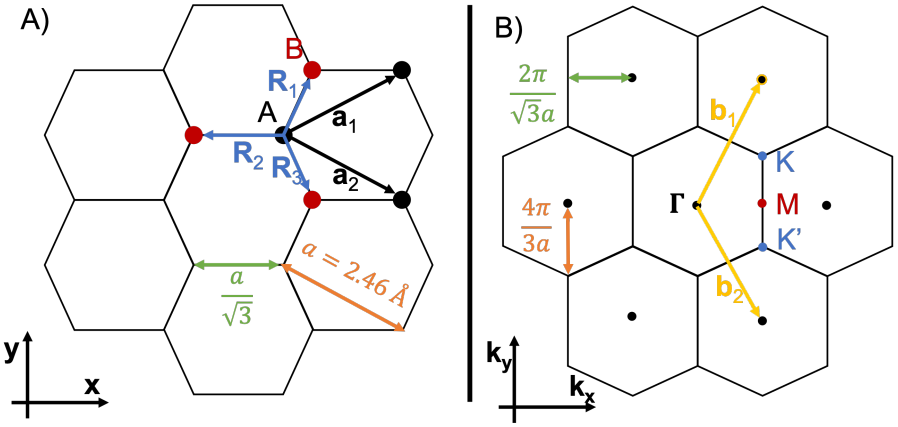

FIGURE 3.8: A) Hexagonal structure of graphene with basis vectors $\boldsymbol{a}_1$ and $\boldsymbol{a}_2$. The nearest neighbors B are pointed by the vectors $\boldsymbol{R}_j$. B) Hexagonal graphene structure in reciprocal space with basis $\boldsymbol{b}_1$ and $\boldsymbol{b}_2$, where K and K', Γ and M are the high symmetry points.

studying HHG, it is necessary to derive the details of the band structure of the solid system used as a target. In our case, we will restrict ourselves to the case of graphene. The following subsection develops the tight-binding approach to graphene's band structure. Once the energy dispersion in known, we shall review the approach we will follow to compute HHG.

The tight-binding description of graphene

Wallace described the electronic energy bands of graphite in the *tight binding* approximation [32], neglecting the overlap between wave functions from both sublattices. Several years later, in 1998, Saito *et al* completed the energy band description including the overlaps and, therefore, the interactions with the nearest neighbors. The band calculation starts from the Bloch electron wave functions defined in the two sublattices A and B, superpositions of carbon atomic orbitals $2p_z$:

$$\phi_{\boldsymbol{k}}^{A}(\boldsymbol{r}) = \frac{1}{\sqrt{N}} \sum_{\boldsymbol{R}_A} e^{i\boldsymbol{k}\cdot\boldsymbol{R}_A} \phi_z(\boldsymbol{r} - \boldsymbol{R}_A), \tag{3.33}$$

$$\phi_{\boldsymbol{k}}^{B}(\boldsymbol{r}) = \frac{1}{\sqrt{N}} \sum_{\boldsymbol{R}_B} e^{i\boldsymbol{k}\cdot\boldsymbol{R}_B} \phi_z(\boldsymbol{r} - \boldsymbol{R}_B), \tag{3.34}$$

where N is the total number of atoms in each sublattice, r is the electron position, and $\boldsymbol{R}_{A,B}$ are the positions of the ions in each sublattice. The phase factors in Eqs. 3.33 and 3.34 result from the application of the Bloch's theorem [78]. The total wave

function is the linear combination of the Bloch orbitals,

$$\psi_{\boldsymbol{k}}(\boldsymbol{r}) = c_A(\boldsymbol{k})\,\phi^A_{\boldsymbol{k}}(\boldsymbol{r}) + c_B(\boldsymbol{k})\,\phi^B_{\boldsymbol{k}}(\boldsymbol{r}). \tag{3.35}$$

Graphene eigenstates correspond to solutions eigenvectors of graphene's Hamiltonian H_κ

$$H_{\boldsymbol{k}}\psi_{\boldsymbol{k}}(\boldsymbol{r}) = E_{\boldsymbol{k}}\psi_{\boldsymbol{k}(\boldsymbol{r})}. \tag{3.36}$$

Multiplying by $\psi^*_{\boldsymbol{k}}(\boldsymbol{r})$ both sides of the equation 3.36 and using 3.35 we obtain

$$\begin{pmatrix} c_A^* & c_B^* \end{pmatrix} H_{\boldsymbol{k}} \begin{pmatrix} c_A \\ c_B \end{pmatrix} = \begin{pmatrix} c_A^* & c_B^* \end{pmatrix} E_{\boldsymbol{k}} S_{\boldsymbol{k}} \begin{pmatrix} c_A \\ c_B \end{pmatrix}, \tag{3.37}$$

with

$$H_{\boldsymbol{k}} = \begin{pmatrix} H_{AA} & H_{AB} \\ H_{BA} & H_{BB} \end{pmatrix}, S_{\boldsymbol{k}} = \begin{pmatrix} S_{AA} & S_{AB} \\ S_{BA} & S_{BB} \end{pmatrix}. \tag{3.38}$$

where $H_{ij} = \langle \phi^i_{\boldsymbol{k}} | H_{\boldsymbol{k}} | \phi^j_{\boldsymbol{k}} \rangle$ and $S_{ij} = \langle \phi^i_{\boldsymbol{k}} | \phi^j_{\boldsymbol{k}} \rangle$, with $i, j \in \{A, B\}$. Then, the Schrödinger equation is transformed into an eigenvalue equation,

$$|H_{\boldsymbol{k}} - E_{\boldsymbol{k}} S_{\boldsymbol{k}}| = 0. \tag{3.39}$$

whose solutions give us the band structure of the π-orbitals.

Let us now estimate the expressions for $H_{\boldsymbol{k}}$ in the nearest neighbors approximation. H_{AA} and H_{BB} represent the average energy of the orbital $2p_z$ with a value of $\varepsilon_{2p} = 0.28eV$. On the other side, an atom of sublattice A has three nearest neighbors atoms, belonging to the B sublattice. Therefore H_{AB} corresponds to the overlap integral

$$\begin{aligned} H_{AB}(\boldsymbol{k}) &= \frac{1}{N}\sum_{\boldsymbol{R}_A}\sum_{\boldsymbol{R}_B} e^{i\boldsymbol{k}\cdot(\boldsymbol{R}_B - \boldsymbol{R}_A)} \int \phi_z(\boldsymbol{r} - \boldsymbol{R}_A)\, H_{\boldsymbol{k}} \phi_z(\boldsymbol{r} - \boldsymbol{R}_B)\, d\boldsymbol{r} \\ &= \frac{1}{N}\sum_{j=1}^{3} e^{i\boldsymbol{k}\cdot\boldsymbol{r}_j} \int \phi_z(\boldsymbol{r} - \boldsymbol{R}_A)\, H_{\boldsymbol{k}} \phi_z\left(\boldsymbol{r} - \boldsymbol{R}_{B_j}\right) d\boldsymbol{r} \\ &= \gamma_0\left(e^{i\boldsymbol{k}\cdot\boldsymbol{r}_{11}} + e^{i\boldsymbol{k}\cdot\boldsymbol{r}_{12}} + e^{i\boldsymbol{k}\cdot\boldsymbol{r}_{13}}\right), \end{aligned} \tag{3.40}$$

being B_j the three nearest neighbors of the atom at the site R_A, and γ_0 the tight-binding integral of graphene, that can be defined as the average interaction energy, experimentally found to be -2.97 eV. Taking into account that:

$$\boldsymbol{R}_1 = \frac{1}{3}\left(2\boldsymbol{a}_1 - \boldsymbol{a}_2\right), \tag{3.41}$$

$$\boldsymbol{R}_2 = \frac{1}{3}\left(-\boldsymbol{a}_1 + 2\boldsymbol{a}_2\right), \tag{3.42}$$

$$\boldsymbol{R}_3 = \frac{1}{3}\left(-\boldsymbol{a}_1 - \boldsymbol{a}_2\right), \tag{3.43}$$

we can define the function

$$\begin{aligned} f\left(\boldsymbol{k}\right) &= e^{-\frac{i}{3}\boldsymbol{k}\cdot\left(\boldsymbol{a}_1+\boldsymbol{a}_2\right)}\left(e^{-\frac{i}{3}\boldsymbol{k}\cdot\boldsymbol{a}_1} + e^{-\frac{i}{3}\boldsymbol{k}\cdot\boldsymbol{a}_2} + 1\right) \\ &= e^{-iak_x/\sqrt{3}}\left[1 + 2e^{i\sqrt{3}ak_x/2}\cos\left(\frac{ak_y}{2}\right)\right], \end{aligned} \tag{3.44}$$

and simplify the equation for H_{AB} as $H_{AB}\left(\boldsymbol{k}\right) = \gamma_0 f\left(\boldsymbol{k}\right)$. Note that $H_{BA} = H_{AB}^*$.

Following a similar path we can obtain the expressions for $S_{\boldsymbol{k}}$ terms. On the one hand, $S_{AA} = S_{BB} = 1$ since $\phi_{\boldsymbol{k}}^A$ and $\phi_{\boldsymbol{k}}^B$ are normalized. On the other hand, the crossed terms can be written as,

$$S_{AB} = s_0 f\left(\boldsymbol{k}\right), \tag{3.45}$$

s_0 being the overlap integral between the nearest neighbors orbitals,

$$s_0 = \int \varphi_z\left(\boldsymbol{r} - \boldsymbol{R}_A\right)\varphi_z\left(\boldsymbol{r} - \boldsymbol{R}_B\right)d\boldsymbol{r}. \tag{3.46}$$

Once we have $H_{\boldsymbol{k}}$ and $S_{\boldsymbol{k}}$ we can obtain the energy bands of the π-orbitals from Eq. (3.39):

$$E_{\pm}\left(\boldsymbol{k}\right) = \frac{\varepsilon_{2p} \mp \gamma_0\left|f\left(\boldsymbol{k}\right)\right|}{1 \mp s_0\left|f\left(\boldsymbol{k}\right)\right|}, \tag{3.47}$$

where $|f\left(\boldsymbol{k}\right)|$ can be found from Eq. 3.44 as

$$\left|f\left(\boldsymbol{k}\right)\right| = \sqrt{1 + 4\cos\frac{\sqrt{3}ak_x}{2}\cos\frac{ak_y}{2} + 4\cos\frac{ak_y}{2}^2}. \tag{3.48}$$

At the Dirac points, K and K' as defined in the previous section 3.3.1, we have

$f(K) = f(K') = 0$, and the electronic bands are locally degenerated with energy ε_{2p_z} corresponding to the Fermi level.

Since $s_0 = 0.073$ is small, we can neglect the overlap between neighbor wave functions. Setting the energy reference at the Fermi level, we find Wallace's solutions [32],

$$E_{\pm}(\boldsymbol{k}) = \gamma_0 \left| f(\boldsymbol{k}) \right|. \tag{3.49}$$

Fig. 3.9 shows a plot of the energy band for two different trajectories in the Brillouin zone, $M - K - \Gamma - K' - M$ and $K - \Gamma - M - K$.

Thus, in the tight-binding approximation, the Hamiltonian can be written as,

$$H_{\boldsymbol{k}} = \begin{pmatrix} 0 & \gamma_0 f(\boldsymbol{k}) \\ \gamma_0 f^*(\boldsymbol{k}) & 0 \end{pmatrix}, \tag{3.50}$$

with eigenstates

$$\left|\Phi_{\boldsymbol{k}}^{\pm}\right\rangle = \frac{e^{i\boldsymbol{k}\cdot\boldsymbol{r}}}{\sqrt{2}} \begin{pmatrix} \mp 1 \\ e^{-i\phi_{\boldsymbol{k}}} \end{pmatrix}, \tag{3.51}$$

where $\phi_{\boldsymbol{k}}$ is the phase of the complex function $f(\boldsymbol{k})$.

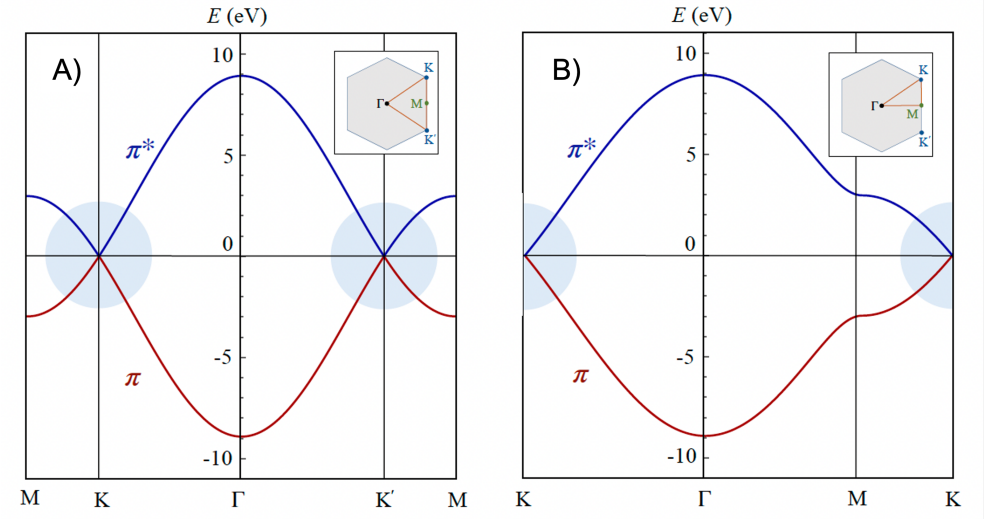

FIGURE 3.9: Solutions for the energy bands, π (red line) and $\pi*$ (blue line), under the tight-biding description following Eq. 3.49. A) and B) represent the bands along different paths in the Brillouin zone, shown in their respectively insets. Figure extracted from [79]

3.3.3 Polycrystalline graphene

Most technological applications of graphene require to produce large-area layers, beyond the micrometer squared. There are different fabrication strategies, the most extended one being chemical vapor deposition (CVD). In 2009 Li et al. [80] presented a potential alternative to exfoliation graphite technique –not scalable technique–, based on growing large-area single-layer graphene films (>95%) of about centimeter squared by CVD growth directly on copper foils by a surface catalyzed process.

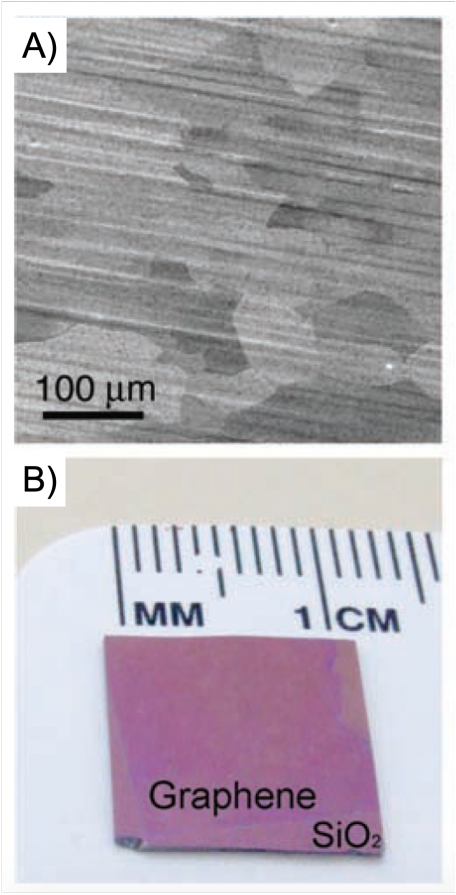

FIGURE 3.10: Graphene grown over copper foils by CVD. A) and B) show a scanning electron microscopy (SEM) image of graphene on a copper substrate and transferred to a SiO_2, respectively. Figures extracted from [80]

The process has two steps. First, the annealing stage where they warm the copper foil up to 1000ºC and deposit a mixture of methane and hydrogen ($CH_4 + H_2$). Then, the cooling stage, when the carbon is segregated to the metal surface. The growth conditions, as the thickness of the metal, the heating temperature, or the cooling process, can determine the deposition mechanism, and therefore the morphology

of the films. The practical interest in the generation of extended foils of graphene in highly reproducible conditions has motivated many studies on strategies to increase the size and to control the different number of grains and their boundaries, in order to obtain particular properties according with the intended applications [81]. Typically, graphene films obtained from CVD are polycrystalline, meaning that the foils are composed of crystalline domains, or grains, with different sizes and orientations. The most widely used technique to characterize single-layer polycrystalline graphene is transmission electron microscopy (TEM).

In 2011, Huang et al. [49] presented a full analysis of single-layer graphene films on copper. They use a variation of TEM called aberration-corrected annular dark-field scanning transmission electron microscopy (ADF-STEM) to characterize the domains and boundaries within the layer. The films were placed upon a holey silicon nitride grid with 2.5 μm length holes. The mean grain size obtained was 250 $\pm$ 11 nm and the grain relative-rotation was mainly centered at $\sim 7^{o}$ and $\sim 30^{o}$. Despite the graphene's electronic properties can be modified by boundary defects, the optical response is more resilient to these details, as the defect boundaries occupy a small fraction of the surface of the domain.

3.3.4 Calculation of HHG in single-layer graphene

In this section we shall review the dynamical equations for the interaction of an electromagnetic pulse with graphene, and how this can be used to compute HHG. We will also review the semiclassical understanding of the process, in terms of quivering electron-hole trajectories.

Electromagnetic field interaction with single-layer graphene

We consider the hamiltonian,

$$H(t) = \sum_{\boldsymbol{k}} H_{\boldsymbol{k}} + V_{int}(t), \tag{3.52}$$

where $H_{\boldsymbol{k}}$ is the graphene's Hamiltonian, Eq.(3.50), and $V_{int}(t) = -q_e \boldsymbol{F}(t) \cdot \boldsymbol{r}$ represents the interaction with the electric field, $\boldsymbol{F}(t)$.

The dynamics of the interaction is governed by the TDSE,

$$i\hbar\frac{\partial}{\partial t}\left|\Psi\left(t\right)\right\rangle = H\left(t\right)\left|\Psi\left(t\right)\right\rangle, \tag{3.53}$$

written as the time-dependent superposition of graphene's eigenstates 3.51. The solution of the time-dependent problem is greatly simplified using the Houston state basis, $\left|\Phi^{\pm}_{\boldsymbol{\kappa}_\tau}\left(t\right)\right\rangle$, with:

$$\boldsymbol{\kappa}_t = \boldsymbol{k} + \frac{q_e}{\hbar}\int_{-\infty}^{t}\boldsymbol{F}\left(\tau\right)d\tau. \tag{3.54}$$

where $\hbar\boldsymbol{\kappa}_t$ can be interpreted as a kinetic quasimomentum. Therefore, we can express the electronic wave function as,

$$\left|\Psi\left(t\right)\right\rangle = \int\left[C_+\left(\boldsymbol{\kappa}_t, t\right)\left|\Phi^{+}_{\boldsymbol{\kappa}_t}\right\rangle + C_-\left(\boldsymbol{\kappa}_t, t\right)\left|\Phi^{-}_{\boldsymbol{\kappa}_t}\right\rangle\right]d\boldsymbol{k}. \tag{3.55}$$

Projecting Eq. 3.53 onto $\left\langle\Phi^{\pm}_{\boldsymbol{\kappa}_t}\right|$ we obtain a differential system:

$$\begin{aligned} i\hbar\frac{\partial}{\partial t}C_\pm\left(\boldsymbol{\kappa}_t, t\right) &= \left[E_\pm\left(\boldsymbol{\kappa}_t\right) - \boldsymbol{F}\left(t\right)\cdot\boldsymbol{D}\left(\boldsymbol{\kappa}_t\right)\right]C_\pm\left(\boldsymbol{\kappa}_t, t\right) \\ &- \boldsymbol{F}\left(t\right)\cdot\boldsymbol{D}\left(\boldsymbol{\kappa}_t\right)C_\mp\left(\boldsymbol{k}, t\right), \end{aligned} \tag{3.56}$$

where $\boldsymbol{D}$ represents the transition matrix element between the conduction and valence band,

$$\boldsymbol{D}\left(\boldsymbol{\kappa}\right) = \left\langle\Phi^{+}_{\boldsymbol{\kappa}_t}\right| q_e\hat{\boldsymbol{r}}\left|\Phi^{-}_{\boldsymbol{\kappa}_t}\right\rangle, \tag{3.57}$$

that also corresponds to the Berry connection. This matrix element presents singularities at the Dirac points that introduce numerical instabilities. A way around this

problem is to rewrite Eq. 3.55 in terms of the Bloch states 3.51 as follows,

$$\begin{aligned}
|\Psi(t)\rangle &= \int C_{+}^{\boldsymbol{\kappa}_t}\left[\frac{e^{i\left(\boldsymbol{\kappa}_t\boldsymbol{r}-\phi_{\boldsymbol{\kappa}_t}\right)}}{\sqrt{2}}\left[-\left|u_A^{\boldsymbol{\kappa}_t}\right\rangle + e^{-\phi_{\boldsymbol{\kappa}_t}}\left|u_B^{\boldsymbol{\kappa}_t}\right\rangle\right]\right] d\boldsymbol{\kappa}_t \\
&+ \int C_{-}^{\boldsymbol{\kappa}_t}\left[\frac{e^{i\left(\boldsymbol{\kappa}_t\boldsymbol{r}-\phi_{\boldsymbol{\kappa}_t}\right)}}{\sqrt{2}}\left[\left|u_A^{\boldsymbol{\kappa}_t}\right\rangle - e^{-\phi_{\boldsymbol{\kappa}_t}}\left|u_B^{\boldsymbol{\kappa}_t}\right\rangle\right]\right] d\boldsymbol{\kappa}_t \\
&= -\int (C_{+}^{\boldsymbol{\kappa}_t} - C_{-}^{\boldsymbol{\kappa}_t})\frac{e^{i\boldsymbol{\kappa}_t\boldsymbol{r}}}{\sqrt{2}}\left|u_A^{\boldsymbol{\kappa}_t}\right\rangle d\boldsymbol{\kappa}_t \\
&+ \int (C_{+}^{\boldsymbol{\kappa}_t} + C_{-}^{\boldsymbol{\kappa}_t})\frac{e^{i\left(\boldsymbol{\kappa}_t\boldsymbol{r}-\phi_{\boldsymbol{\kappa}_t}\right)}}{\sqrt{2}}\left|u_B^{\boldsymbol{\kappa}_t}\right\rangle d\boldsymbol{\kappa}_t \\
&= \int C_A^{\boldsymbol{\kappa}_t}\frac{e^{i\boldsymbol{\kappa}_t r}}{\sqrt{2}}\left|u_A^{\boldsymbol{\kappa}_t}\right\rangle d\boldsymbol{\kappa}_t + \int C_B^{\boldsymbol{\kappa}_t}\frac{e^{i\boldsymbol{\kappa}_t r}}{\sqrt{2}}\left|u_B^{\boldsymbol{\kappa}_t}\right\rangle d\boldsymbol{\kappa}_t. \qquad (3.58)
\end{aligned}$$

where we have defined,

$$C_A^{\boldsymbol{\kappa}_t} = -(C_{+}^{\boldsymbol{\kappa}_t} - C_{-}^{\boldsymbol{\kappa}_t}) \qquad (3.59)$$

$$C_B^{\boldsymbol{\kappa}_t} = (C_{+}^{\boldsymbol{\kappa}_t} + C_{-}^{\boldsymbol{\kappa}_t})\, e^{-i\phi_{\boldsymbol{\kappa}_t}} \qquad (3.60)$$

Rewriting the dynamical equations in terms of these coefficients, we end with

$$i\hbar\frac{d}{dt}C_A^{\boldsymbol{\kappa}_t} = \frac{E_{+}(\boldsymbol{\kappa}_t) + E_{-}(\boldsymbol{\kappa}_t)}{2}C_A^{\boldsymbol{\kappa}_t} - \frac{E_{+}(\boldsymbol{\kappa}_t) - E_{-}(\boldsymbol{\kappa}_t)}{2}C_B^{\boldsymbol{\kappa}_t}e^{i\varphi_{\boldsymbol{\kappa}_t}} \qquad (3.61)$$

$$i\hbar\frac{d}{dt}C_B^{\boldsymbol{\kappa}_t} = \frac{E_{+}(\boldsymbol{\kappa}_t) + E_{-}(\boldsymbol{\kappa}_t)}{2}C_B^{\boldsymbol{\kappa}_t} - \frac{E_{+}(\boldsymbol{\kappa}_t) - E_{-}(\boldsymbol{\kappa}_t)}{2}C_A^{\boldsymbol{\kappa}_t}e^{i\varphi_{\boldsymbol{\kappa}_t}}, \qquad (3.62)$$

where the Berry connections do not appear explicitly and, therefore, the singularities at the Dirac points do not introduce numerical instabilities. The time-dependent dipole is computed from the solution of Eqs. 3.61 and 3.62 as

$$\boldsymbol{d}(t) = \langle\Psi(t)|\, q_e\hat{\boldsymbol{r}}\,|\Psi(t)\rangle\,. \qquad (3.63)$$

Following the Houston frame, and with $C^{A,B}$ coefficients, the dipole emission is:

$$\boldsymbol{d}(t) = i\frac{q_e}{2}\int\left[C_A^{\boldsymbol{\kappa}_t *}\nabla_{\boldsymbol{\kappa}_t}C_A^{\boldsymbol{\kappa}_t} + C_B^{\boldsymbol{\kappa}_t *}\nabla_{\boldsymbol{\kappa}_t}C_B^{\boldsymbol{\kappa}_t}\right]d\boldsymbol{k}. \qquad (3.64)$$

We then compute the HHG spectrum using the dipole acceleration, i.e. the second time-derivative of Eq. 3.64. In Fig. 3.11 we present an example of a HHG spectrum obtained in graphene driven by 3 μm wavelength laser pulse. We used a $\sin^2$ driving

laser pulse envelope of 6-cycles total duration and peak intensity of 5×10^{11} W/cm^2. As in the case of gases, we can identify a *plateau* structure that extends towards a maximum cutoff frequency.

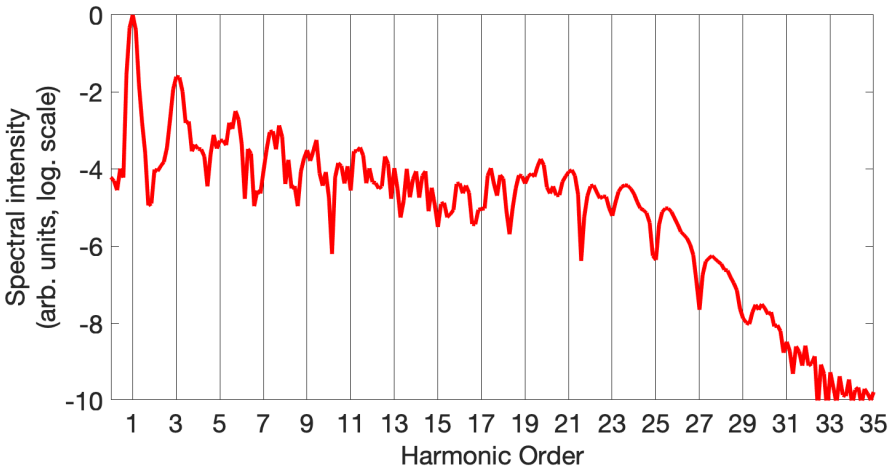

FIGURE 3.11: TDSE simulation results of the HHG spectrum obtained in graphene driven by a 3 μm, 6 cycles (total duration) and 5×10^{11} W/cm^2 peak intensity pulse.

Semiclassical description

Following the path described in Ref. [40], we can derive a semiclassical approach of HHG in graphene by defining the action

$$S_g\left(\boldsymbol{k}, t, t_1\right) = -\int_{t_1}^{t} \left[E_+\left(\boldsymbol{\kappa}_\tau\right) - E_+\left(\boldsymbol{\kappa}_\tau\right)\right] d\tau. \tag{3.65}$$

Modelling the Berry connection as a Dirac delta at the Dirac points, the dipole interband contribution can be written as

$$d_{\updownarrow}\left(t\right) = i\frac{D_0}{q_e}\int e^{\frac{i}{\hbar}S_g\left(\boldsymbol{k}_D, t, t_{D,\boldsymbol{k}}\right)} D\left(\boldsymbol{\kappa}_t, t\right) d\boldsymbol{k}, \tag{3.66}$$

$t_{D,\boldsymbol{k}}$ being the instant of time when the valence electron trajectory passes near a Dirac point, where the electron-hole pair is generated. Similarly to what happens in gases [82], the HHG dipole is dominated by the action. Eq. 3.66 can be integrated using the saddle-point approximation leading to the following conditions for the electron trajectories

$$E_+\left(\boldsymbol{\kappa_t}\right) - E_-\left(\boldsymbol{\kappa_t}\right) = q\hbar\omega_0 \tag{3.67}$$

$$\int_{t_{D,\boldsymbol{k}}}^{t} \boldsymbol{v}_{+}\left(\boldsymbol{\kappa}_{t}\right) d\tau = \int_{t_{D,\boldsymbol{k}}}^{t} \boldsymbol{v}_{-}\left(\boldsymbol{\kappa}_{t}\right) d\tau, \tag{3.68}$$

where $\boldsymbol{v}_{\pm}\left(\boldsymbol{\kappa}_{t}\right) = \left(1/\hbar\right) \nabla_{\boldsymbol{k}} E_{\pm}\left(\boldsymbol{\kappa}_{t}\right)$ are the velocity of the electrons in both bands. The first condition fixes the energy of the photon emitted as the value of the band gap at the moment of recombination, t. The second condition determines that, in this semiclassical framework, the recombination of the electron-hole pair is possible if their position coincides in the real space. This condition defines the concept of a *perfect recollision*, a relevant concept in the framework of this thesis work.

Using Eqs. 3.67 and 3.68 we can calculate the trajectories of the electron and the possible recombination energies. In Fig. 3.12A), we present the TFA (color background) of the TDSE harmonic emission shown in Fig. 3.11. We also include the trajectories estimated from the semiclassical description. Note that the trajectories starting in K (light red line) are half a cycle delayed compare to those starting at K' (dark red line). Interestingly, at the beginning of the HHG emission both results match very well, the semiclassical study can reproduce the TDSE spectrum at this stage. However, in rear part of the pulse, the trajectories do not properly resolve the emission obtained by the TDSE. In this thesis work we explore the sources of this phenomena, and we demonstrate the existence of the *imperfect recollisions* in HHG in single-layer graphene. In Fig. 3.12B), we plot a map of the energy of the electron-hole pair in terms of its excitation and recombination time.

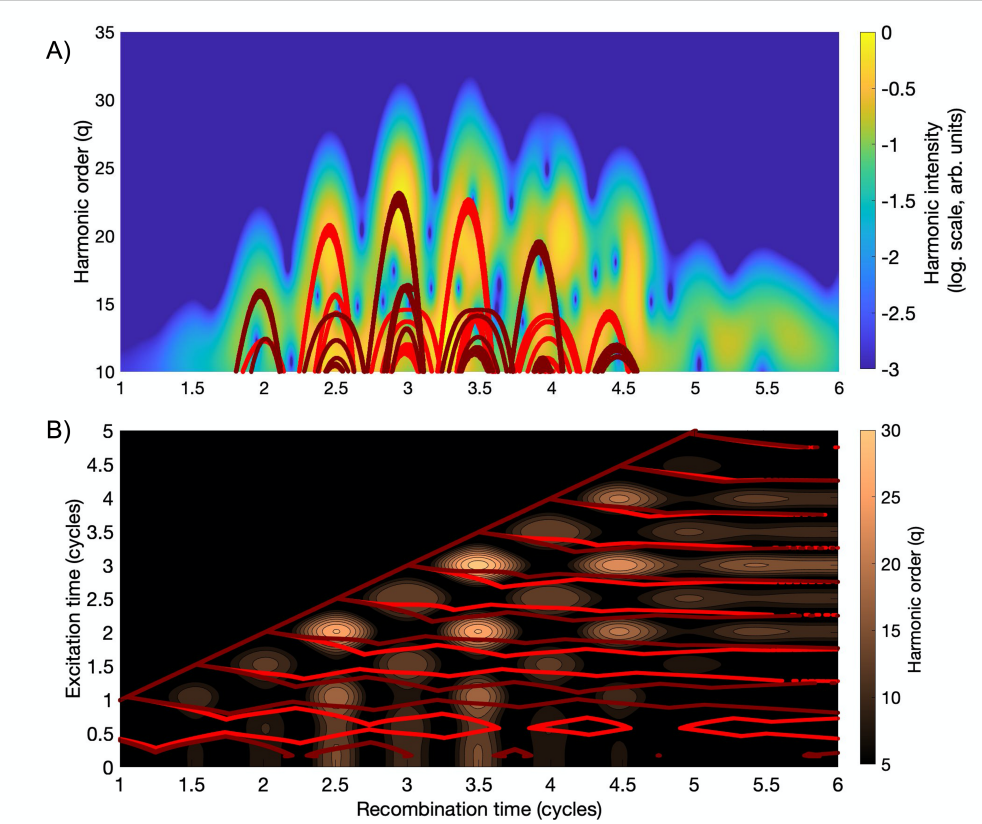

FIGURE 3.12: Results of HHG in graphene driven by a field centered at $3\mu m$, 6 cycles pulse with a $5 \times 10^{11} W/cm^2$ peak intensity. Panel A) shows in red the possible *perfect recollisions* calculated with Eqs. 3.67 and 3.68 over the TFA and the TDSE results. Panel B) depicts the corresponding band gap distribution in terms of the excitation and recombination times assuming *perfect recollisions*.

Chapter 4

Results

In this chapter we present the results of HHG in single-layer graphene developed along this thesis work. We analyze the process from different perspectives. Starting from a microscopic point of view, we study the quality of the description of HHG in terms of semiclassical trajectories and the role of the *imperfect recollisions*. In a second paper, we explore the macroscopic aspects of HHG, resolving the influence of *transverse phase-matching* in the build-up of the target harmonic emission, i.e. the one that would be observed in experiments. Finally, we analyze the potential use of high-order harmonic spectroscopy in a rather interesting application: the statistical characterization of domains in polycrystalline graphene.

4.1 Classical study of electron trajectories: the role of *imperfect recollisions*

In this paper we investigated the role of the *imperfect recollisions* in the process of HHG from single-layer graphene. Our results evidence the relevance of these non-classical electron-hole recombinations in the emitted harmonic spectrum.

The concept of *imperfect recollisions* is relatively new in the frame of HHG in solids. Originally, semiclassical recollision models similar to that introduced in section 3.3.4 or in Ref. [83], assume that, after the creation of the electron-hole pair, the high-order harmonics are emitted once the electron and the hole re-encounter in real space. Recently, Yue and Gaarde provided a new perspective in Ref. [53], introducing the concept of *imperfect recollisions*. From a quantum point of view, they demonstrated in monolayer hexagonal boron nitride, the possibility of electron-hole

recombination even if the wave-packet centers, i.e. the semiclassical positions, are spatially separated tens of a.u. due to the spread of the electron and hole wave wave packets (see Fig.4.1). They developed an extended recollision model (ERM) that relaxes the restriction of spacial re-encounter of the electron and hole trajectories, and included the effect of Berry connections and transition dipole phases in the trajectories. Comparing with quantum results calculated with the semiconductor Bloch equations (SBE) they concluded that *imperfect recollisions* are relevant in systems with large Berry curvatures.

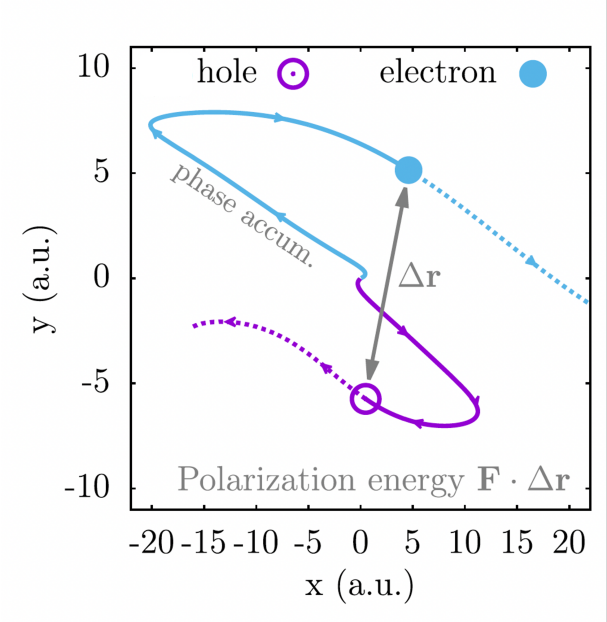

FIGURE 4.1: *Imperfect recollision* between the electron and the hole with a relative distance Δr. Figure extracted from [53].

This new phenomenon opens the door to reconsider the trajectory analysis in different solid systems such as graphene. Even though graphene does not present Berry curvatures, and the mechanism to produce high-order harmonics varies from the case of finite-gap solids, as we have introduced in Chapter 1, *imperfect recollisions* might be also relevant. In fact, in Fig. 3.12a) it is noticeable that *perfect recollisions* can not reproduce the hole TFA of the graphene HHG emission, as at the rear part of the pulse there are emissions from the TDSE that are not predicted with the semiclassical solutions.

In our contribution we relax the condition in Eq. 3.68 to select recollisions with

different relative distances of a chosen case of HHG in graphene, driven by a linearly polarized pulse with a peak intensity of $5 \times 10^{11} W/cm^2$ and centered at 3 μm. We demonstrated that *imperfect recollisions* are also important in graphene. The correct description of the harmonic emission requires to include electron-hole excursion times higher than one cycle of the driving field. For example, in the reported case, we found that *imperfect recollisions* with electron-hole distances of up to 492 Å are relevant in the harmonic emission.

Resumen

According to the requirements of the University of Salamanca, the Spanish version of the abstract is:

Estudios recientes en la generación de armónicos de orden elevado (HHG) en sólidos revelan nuevos escenarios con dinámicas electrónicas extraordinariamente ricas, comparadas con los casos de átomos y moléculas. En el caso de estos úlitmos, los principales aspectos del proceso se pueden describir semiclasicamente en función de los electrones que recombinan cuando las trayectorias pasan de nuevo por el ion padre. HHG en sólidos se describe con un mecanismo similar, en este caso se tiene en cuenta la recombinación del par electrón-hueco. Sin embargo, se ha reportado recientemente que una parte sustancial de la emisión de HHG corresponde a situaciones donde el electrón y el hueco no se sobreponen espacialmente. Según el conocimiento actual, HHG que vienen de las recolisiones imperfectas reflejan la naturaleza cuántica del proceso, en sistemas con grandes curvaturas de Berry o cuando el campo incidente está polarizado elípticamente. En este trabajo, demostramos que las recolisiones imperfectas son también relevantes en un caso más general. Demostramos el papel de este tipo de recolisiones en el espectro de HHG en grafeno – un sistema sin curvatura de Berry– iluminado por un campo linealmente polarizado. Nuestros cálculos también revelan que los multiples órdenes de las recolisiones imperfectas contribuyen en la emisión de armónicos cuando el tiempo de excursión del par electrón hueco sobrepasa un ciclo del campo incidente. Consideramos que nuestro trabajo supone una contribución sustancial para el completo entendimiento de las dinámicas inferiores al fentosegundo de HHG en sistemas sólidos.

Research Article | Vol. 30, No. 9 / 25 Apr 2022 / Optics Express 15546
Optics EXPRESS

Non-classical high harmonic generation in graphene driven by linearly-polarized laser pulses

ROBERTO BOYERO-GARCÍA,* ANA GARCÍA-CABRERA, OSCAR ZURRÓN-CIFUENTES, CARLOS HERNÁNDEZ-GARCÍA, AND LUIS PLAJA

Grupo de Investigación en Aplicaciones del Láser y Fotónica, Departamento de Física Aplicada, Universidad de Salamanca, E- 37008, Salamanca, Spain
*robertobg@usal.es

Abstract: Recent studies in high-order harmonic generation (HHG) in solid targets reveal new scenarios of extraordinary rich electronic dynamics, in comparison to the atomic and molecular cases. For the later, the main aspects of the process can be described semiclassically in terms of electrons that recombine when the trajectories revisit the parent ion. HHG in solids has been described by an analogous mechanism, in this case involving electron-hole pair recombinations. However, it has been recently reported that a substantial part of the HHG emission corresponds to situations where the electron and hole trajectories do not overlap in space. According to the present knowledge, HHG from this *imperfect* recollisions reflects the quantum nature of the process, arising in systems with large Berry curvatures or for elliptically polarized driving fields. In this work, we demonstrate that *imperfect* recollisions are also relevant in the more general case. We show the signature of such recollisions in the HHG spectrum from monolayer graphene —a system with null Berry curvature— irradiated by linearly polarized driving fields. Our calculations also reveal that *imperfect* multiple-order recollisions contribute to the harmonic emission when electron-hole excursion times exceed one cycle of the driving field. We believe that our work adds a substantial contribution to the full understanding of the sub-femtosecond dynamics of HHG in solid systems.

1. Introduction

High-harmonic generation (HHG) is nowadays a well established technique to generate highly coherent extreme-ultraviolet/x-ray radiation [1–7]. The phenomenon stems from the non-perturbative interaction of intense laser light with matter. For atomic and molecular targets, HHG can be understood in semiclassical terms, according to the so-called three-step model [8]. In this point of view, harmonics are radiated when a tunnel-ionized electron returns to the parent ion, where it recombines releasing its kinetic energy in the form of high-frequency radiation. This later step is only efficient if the electron's trajectory returns to the parent ion, which is a condition naturally found in linearly-polarized driving fields. For elliptically-polarized drivers, the electrons are pulled away from the parent ion, and the efficiency of the HHG process decreases accordingly [9]. It is worth noticing also that the electron may not recombine at the first encounter with the parent ion, therefore the harmonics can be emitted at subsequent *higher-order* recollisions [10–12]. In such case, however, the radiated photon energies fall well below the maximum photon energy of the first recollisions (the so-called harmonic *cutoff* frequency). Moreover, since high-order recollisions imply electron's excursion times longer than the driver's cycle, they are associated to lower harmonic conversion efficiencies, resulting from the progressive spread of the electron's wavepacket in the continuum [13–15].

#452201 https://doi.org/10.1364/OE.452201
Journal © 2022 Received 23 Dec 2021; revised 22 Feb 2022; accepted 7 Apr 2022; published 21 Apr 2022

Optics EXPRESS

Solid targets provide richer scenarios for HHG [6,16–21]. In this case, the irradiation geometry defines the HHG mechanism. For grazing incidences, i.e. when the polarization plane of the driving electric field is perpendicular to the target's surface, HHG follows from the recombination of electrons detached from the target [22], in close resemblance to the ionization mechanism in atomic and molecular cases. For solid targets, however, the crystal periodicity leaves a signal in the detached electron's wavefunction, in form of Talbot modulations, which in turn are reflected in the HHG spectrum. This phenomenon gives ground to the recent proposal of ultrafast Talbot spectroscopy at the nanometer scale [23]. On the other hand, for the case of normal incidence or bulk solid targets, the HHG mechanism follows from an adapted semiclassical three-step model [24]. According to this view, the electron's tunnel ionization step is replaced by tunnel excitation to the conduction band, and the consequent creation of a hole. Harmonics result from the electron-hole recombination at times when the electron and hole trajectories overlap, i.e. the so called *perfect recollisions* (ehPR). As a main characteristic, the harmonic *cutoff* frequency corresponds to the maximum energy gap during the electron/hole excursion [24–28].

Despite of these fundamental similarities, HHG in solids turns out to be far more complex than in atoms and molecules. On the one side, the crystal band's dispersion is not quadratic and thus, the dynamics of the electron in the conduction band is not as trivial as that of an electron ionized in free space. In addition, Berry curvatures introduce a deflection in the electron and hole trajectories. Therefore, while in gas systems the electron trajectories are universally defined, in solids they depend on the target species. On the other side, the details of the excitation of the electron to the conduction band are also affected by the band structure. For instance, it has been demonstrated that HHG from elliptically-polarized drivers results from electrons tunnel-excited at points surrounding the minimum band gap, rather than at the exact point [29]. In 2D semimetals enclosing Dirac points, the excitation details are more involved, as tunneling is replaced by the non-adiabatic crossing near these singular points [30]. This simple variation in the first step leads to substantial differences in the HHG process, as electron-hole excitation is no longer linked to the maxima of the driving field's amplitude. In other low dimensional targets, as carbon nanotubes, HHG follows from a similar non-adiabatic excitation mechanism near the Van Hove singularities [31].

In the general case, the complex dynamics in crystals does not only affect the maximum photon's energy but also the polarization and phase properties of the emitted harmonics. In particular, the band geometry around the symmetry points can lead to a highly non-linear anisotropic response, resulting in the generation of harmonics with elliptical polarization even when driven by linearly-polarized drivers [22,32–41]. In addition, the convoluted electronic dynamics during HHG in solids leads to high harmonics with complex phase properties. As a result, accounting for the spatial phase distribution in HHG from a macroscopic target [26,42] has allowed to achieve a better understanding of the harmonic spectrum properties.

It has been recently shown that although the modified semiclassical three-step model accounts for the main features of the HHG mechanism in solids, non-classical pathways can be also relevant in systems with large Berry curvatures [43] or when HHG is driven by elliptically polarized fields [44]. In these cases, harmonics are emitted during electron-hole *imperfect recollisions* (ehIR), i.e. when the electron-hole wave packets overlap even though their centers are spatially separated by distances one order of magnitude larger than the lattice constant [43].

In this article, we demonstrate that ehIR's have a relevant role also for HHG in solids with vanishing Berry curvature and driven by linearly-polarized laser fields. In particular, we show the enhanced role of high-order ehIR at times larger than the laser cycle. The excellent agreement between our semiclassical and quantum calculations demonstrates that ehIR must be considered to obtain a better understanding of the complex phase properties of HHG in solids.

The article is organized as follows. In Section 2, we present the details of the computation of the nonlinear response, where we use two models: the resolution of the time dependent

Optics EXPRESS

Schrödinger equation within the first neighbor tight-binding approximation, and a semiclassical saddle-point approach which allow us to interpret our results. In Section 3, we present and discuss our findings, where we identify the role of ehPR and ehIR for several cases of HHG in single-layer graphene driven by a linearly-polarized laser field. Finally we present our conclusions in Section 4.

2. Theoretical description of HHG in single-layer graphene

We consider the emission of high-order harmonics in single-layer graphene irradiated by a short mid-infrared pulse, linearly polarized along the graphene sheet plane. To this end, we compute the nonlinear response of graphene following the method described in [30], and we interpret our results in terms of classical electron-hole trajectories in real space. The dynamics of the interaction of a single layer graphene sheet with an ultrashort laser pulse will be described in the first neighbor tight-binding approximation [45]. We express the electron wavefuntion in terms of the graphene's eigenstates, $\Phi_{\mathbf{k}}^{\pm}(\mathbf{r})$,

$$\Psi(\mathbf{r},t) = \int \Psi_{\mathbf{k}}(\mathbf{r},t)d\mathbf{k} = \int \left[C_+(\mathbf{k},t)\Phi_{\mathbf{k}}^{+}(\mathbf{r}) + C_-(\mathbf{k},t)\Phi_{\mathbf{k}}^{-}(\mathbf{r})\right] d\mathbf{k}. \tag{1}$$

with $\Phi_{\mathbf{k}}^{\pm}(\mathbf{r})$ given as vectors in the basis of Bloch states,

$$\Phi_{\mathbf{k}}^{\pm}(\mathbf{r}) = \sqrt{\frac{1}{2}}e^{i\mathbf{k}\cdot\mathbf{r}}\begin{pmatrix} \pm 1 \\ e^{-i\phi(\mathbf{k})} \end{pmatrix}, \tag{2}$$

$\phi(\mathbf{k})$ being the argument of the complex function $f(\mathbf{k})$,

$$f(\mathbf{k}) = e^{-iak_x/\sqrt{3}}\left(1 + 2e^{i\sqrt{3}ak_x/2}\cos\frac{ak_y}{2}\right), \tag{3}$$

where $a = 2.46$Å.

The evolution of $\Psi(\mathbf{r},t)$ is solved in the reciprocal space's moving frame $\hbar\boldsymbol{\kappa}_t = \hbar\mathbf{k} - q_e\mathbf{A}(t)/c$, where $\mathbf{A}(t)$ is the vector potential of the electromagnetic field, c the speed of light, and q_e the electron's charge. The numerical instabilities associated with the singularities at the Dirac points can be circumvented by using the change of variables,

$$C_M(\boldsymbol{\kappa}_t,t) = C_+(\boldsymbol{\kappa}_t,t) - C_-(\boldsymbol{\kappa}_t,t) \tag{4}$$

$$C_P(\boldsymbol{\kappa}_t,t) = e^{-i\phi(\boldsymbol{\kappa}_t)}\left[C_+(\boldsymbol{\kappa}_t,t) + C_-(\boldsymbol{\kappa}_t,t)\right], \tag{5}$$

whose temporal dependence is governed by the following equations,

$$i\hbar\frac{d}{dt}C_M(\boldsymbol{\kappa}_t,t) = \frac{E_+(\boldsymbol{\kappa}_t)+E_-(\boldsymbol{\kappa}_t)}{2}C_M(\boldsymbol{\kappa}_t,t) + \frac{E_+(\boldsymbol{\kappa}_t)-E_-(\boldsymbol{\kappa}_t)}{2}e^{i\phi(\boldsymbol{\kappa}_t)}C_P(\boldsymbol{\kappa}_t,t) \tag{6}$$

$$i\hbar\frac{d}{dt}C_P(\boldsymbol{\kappa}_t,t) = \frac{E_+(\boldsymbol{\kappa}_t)+E_-(\boldsymbol{\kappa}_t)}{2}C_P(\boldsymbol{\kappa}_t,t) + \frac{E_+(\boldsymbol{\kappa}_t)-E_-(\boldsymbol{\kappa}_t)}{2}e^{-i\phi(\boldsymbol{\kappa}_t)}C_M(\boldsymbol{\kappa}_t,t) \tag{7}$$

where $E_{\pm}(\mathbf{k}) = \pm\gamma_0|f(\mathbf{k})|$ are the energies of the valence $(-)$ and conduction $(+)$ bands, respectively, and with $\gamma_0 = 2.97$ eV [45].

Finally, by solving Eqs. (6) and (7), we calculate the harmonic emission from the dipole acceleration, $\mathbf{a}(t) = \frac{d^2}{dt^2}\mathbf{d}(t)$ as [30],

$$\mathbf{d}(t) = \langle\Psi(t)|q_e\mathbf{r}|\Psi(t)\rangle = i\frac{q_e}{2}\int\left[C_M^*(\boldsymbol{\kappa}_t,t)\nabla_{\mathbf{k}}C_M(\boldsymbol{\kappa}_t,t) + C_P^*(\boldsymbol{\kappa}_t,t)\nabla_{\mathbf{k}}C_P(\boldsymbol{\kappa}_t,t)\right]d\mathbf{k}. \tag{8}$$

The fundamental physical aspects of HHG in graphene can be revealed by deriving a semiclassical saddle-point approximated model (SPAM), as dicussed in [30]. SPAM considers that the emission

Optics EXPRESS

of the q-th harmonic takes place at time t when the following conditions are fulfilled:

$$E_+(\boldsymbol{\kappa}_t) - E_-(\boldsymbol{\kappa}_t) = q\hbar\omega_0 \tag{9}$$

$$\int_{t_{D,\mathbf{k}}}^{t} \mathbf{v}_+(\boldsymbol{\kappa}_\tau)d\tau = \int_{t_{D,\mathbf{k}}}^{t} \mathbf{v}_-(\boldsymbol{\kappa}_\tau)d\tau \tag{10}$$

where $\mathbf{v}_\pm(\boldsymbol{\kappa}_\tau) = \nabla_{\mathbf{k}} E_\pm(\boldsymbol{\kappa}_\tau)/\hbar$, ω_0 is the laser's fundamental frequency and $t_{D,\mathbf{k}}$ the time when the electron with wave vector $\mathbf{k}$ at the beginning of the interaction crosses the Dirac point, i.e. the time when the electron-hole pair is created. In agreement with the semiclassical description of HHG in solids, SPAM considers that the HHG emission is produced by the recombination of overlapping classical electron-hole trajectories. Note, however, that SPAM describes the evolution of the mean position of the electron and hole wavepackets created in the vicinity of the Dirac points. The excitation of the wavepacket is not resonant with a one photon absorption, but rather is of the Landau-Zenner type during the non-adiabatic crossing near the Dirac points. As a consequence, the pair creation is not confined to the field-amplitude maxima, where tunnel excitation is most likely, but takes place at any time during the interaction. Following the ideas developed in [29,43], in this article we shall demonstrate a substantial role of ehIR in single-layer graphene. Note that this role is unexpected, as graphene is a system with null Berry curvature and our calculations assume that HHG is driven by linearly-polarized laser fields. To include ehIR, we have expanded the SPAM model to take into account the contribution of electron-hole trajectories that do not overlap classically. Therefore, we relax the condition of trajectory crossing in Eq. (10) by allowing the recombination distance ΔR to be nonzero [43],

$$\Delta R \equiv \int_{t_{D,\mathbf{k}}}^{t} \left[\mathbf{v}_+(\kappa_\tau) - \mathbf{v}_-(\kappa_\tau)\right] d\tau \tag{11}$$

Note that this semiclassical approach (SPAM), which does not include the wavepacket dispersion, is just used to interpret the results of the full quantum calculations given by Eqs. (6) and (7).

3. Results and discussion

We consider a six optical cycles (o.c.) driving field with a $\sin^2$ envelope, which corresponds to 2.2 o.c., 22 fs, of full width at half maximum (FWHM) in intensity (see inset in Fig. 1(a)). The field is assumed linearly polarized along the Γ-K direction. The laser pulse is centered at 3 μm wavelength, with a peak intensity of 5×10^{11} W/cm^2, and it is aimed perpendicularly to the graphene's layer. Note that the pulse duration is shorter that the typical electron thermalization time [46]. The resulting harmonic spectrum and its time-frequency analysis are presented in Figs. 1(a) and 1(b), respectively. The time-frequency representation has been obtained scanning over the HHG spectral amplitudes with a Gaussian mask of $4\omega_0$ in FWHM, and subsequently performing the Fourier transform of each sample. As a reference, Figs. 1(c) and 1(d) show the same information for the case of HHG in a hydrogen atom. HHG in hydrogen is calculated from the solution of the three-dimensional time dependent Schrödinger equation, using a 0.72 μm driving field of peak intensity of 1.6×10^{14} W/cm^2, parameters that have been adjusted to produce a HHG spectrum with similar *cutoff* frequency as the graphene case.

The comparison of both spectra reveals that the emission of harmonics in graphene presents a temporal structure far more complex than that in atoms. In the atomic case (Fig. 1(d)) the high-order harmonics result from two well-resolved emission bursts per half-cycle, the so-called short and long trajectories, which present a positive and negative slope structure in the time-frequency representation, respectively [47–51]. In contrast, in HHG from graphene, the first step —the creation of the electron-hole pair— is connected with the Dirac points: electron-hole pair excitation follows from the non-adiabatic crossing near the singular points (see the inset of

Optics EXPRESS

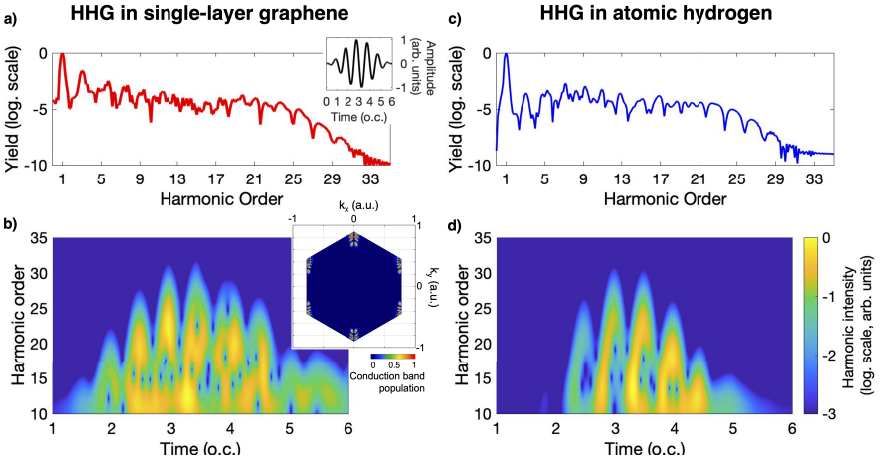

Fig. 1. Harmonic spectrum (a) and time-frequency analysis (b) of the high order harmonic emission from single-layer graphene. The inset in (a) plots the driving electric field, a 3 μm, six-cycles $\sin^2$ pulse (22 fs FWHM) linearly polarized in the graphene plane along the Γ-K direction, with peak intensity of 5×10^{11} W/cm^2. Panels (c) and (d) plot the same information from a hydrogen atom target, irradiated with a linearly-polarized 0.72 μm, six-cycles $\sin^2$ pulse, with peak intensity of 1.6×10^{14} W/cm^2. Inset in (b) is the normalized color map of the electron excitation in the conduction band. The time at which this snapshot is taken is depicted in the inset of panel (a), at 2.75 cycles after the beginning of the laser pulse.

Fig. 1(b)) and, therefore, pairs are created continuously instead of at the driving field's maxima, as it is the general case for bulk crystals, atoms and molecules. As a result, the number of interfering trajectories playing a relevant role in HHG in graphene is substantially larger, and not necessarily regularly spaced in time [30], as it can be observed in Fig. 1(b). Note that, once the driving field interaction with the graphene layer ends, the time-frequency picture reveals that there is still emission from the excited sample, a behavior that has been reported in previous works [36]. In the following we shall see that, even though the semiclassical trajectories leading to ehPR successfully account for the main spectral features in Figs. 1(a) and 1 (b), the harmonic signal can only be fully explained considering also the role of ehIR.

We present in Fig. 2 the results of the SPAM calculations for the graphene case presented in Fig. 1. The background in Figs. 2(a) and 2(b) are replicas of Fig. 1(b). We analyse the temporal distribution of electron-hole recombination energies from ehPR (Fig. 2(a)) and ehIR (Fig. 2(b)). The plotted ehIR energies correspond to the cases in which the electron and hole are 10 unit cells (24 Å, pink lines) and 70 unit cells (172 Å, grey lines) apart, at the instant of recombination. Lighter tones are used for trajectories initiated near the K Dirac points, and darker tones for those initiated near the K′ points (see the inset in Fig. 2(c)). Note that, while the temporal distribution of radiated frequencies from ehPR explains reasonably the fundamental features of the HHG spectrum in (Fig. 2(a)), it becomes also clear that ehPR do not provide a full explanation of the harmonic contributions at intermediate times and, specially, at the end of the driving pulse.

To simplify the discussion of the results from ehIR in Fig. 2(b), we shall focus our attention to the highest harmonic orders, q>15, and to the trajectories originated at the Dirac point K (lighter lines). The discussion of the emission for pairs originated near points K′ (darker lines) is analogous, due to the crystal's inversion symmetry.

Figure 2(b) points out that the emissions from ehIR's for increasingly longer recombination distances are progressively delayed. This is consistent with the increasingly larger excursion times needed for the electron-hole pair to reach longer interparticle distances. This aspect is

Optics EXPRESS

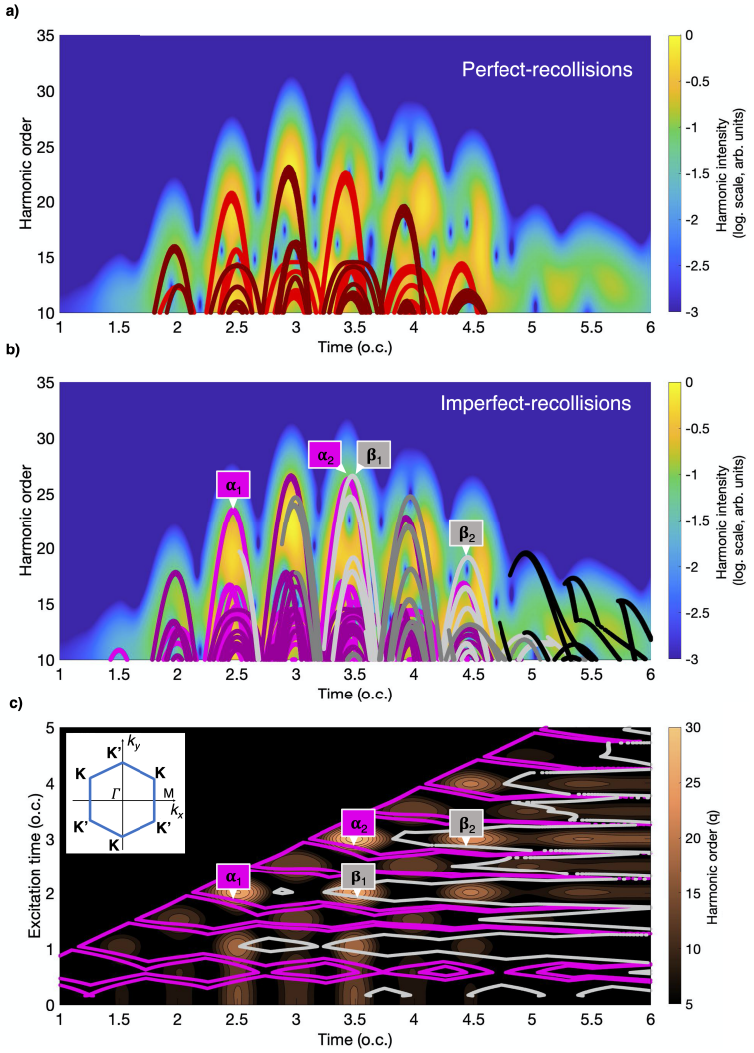

Fig. 2. Results of the harmonic emission corresponding to trajectories leading to ehPR —red, panel (a)— and ehIR —pink and grey, panel (b)—. The electron-hole pairs are created at points K (light colors) and K′ (dark colors) of the graphene's Brillouin zone. Panels (a) and (b) show the energy of the electron-hole pair at recombination obtained with the semiclassical SPAM calculations against the background corresponding to the time-frequency analysis shown in Fig. 1 (b). In (a) we plot the frequency of the harmonic emission corresponding to ehPR, i.e. when the electron and hole classical trajectories intersect, and in (b) the same results for ehIR, where the electron-hole distances at the recombination time are 24 Å (pink) and 172 Å (grey). We have added a long recombination distance of 492 Å (black) in order to recover the harmonic emission at the rear part of the pulse. Panel (c) shows the distribution of energies radiated from ehIR as a function of the pair recombination (horizontal axis) and excitation (vertical axis) times. The inset shows the geometry of graphene's Brillouin zone. Labels α_i and β_i correspond to two pairs of sampled ehIR trajectories recombining at 24 Å and 172 Å, respectively, with excitation times of ∼1.9 o.c. (i=1), and ∼2.9 o.c. (i=2).

Optics EXPRESS

reproduced in Fig. 2(c), where we show the energy of the electron-hole pair at any potential recombination time, as a function of the pair recombination (horizontal axis) and excitation (vertical axis) times. Labels α_i and β_i correspond to two pairs of sampled ehIR trajectories recombining at distances of 24 Å and 172 Å, respectively, with different excitation times: ~1.9 o.c. for i=1, and ~2.9 o.c. for i=2. To complete our analysis, we have also included in Fig. 2(b) the trajectory contributions of ehIR that recombine at longer distances (200 unit cells, 492 Å, black lines), which present a relevant contribution at the rear part of the harmonic emission. Thus, our analysis unequivocally demonstrates the relevance of ehIR in HHG in graphene. The harmonic contributions that are not reproduced by ehPR in Fig. 2(a) are mostly fulfilled by the ehIR sampled in Fig. 2(b), whereas the nature of ehIR is clearly identified in Fig. 2(c). We note that a larger sample of ehIR born at different excitation times, and with other recombination distances, completely fulfills the harmonic emmission not reproduced by ehPR in Fig. 2(a).

It is important to point out that the excursion time, i.e. the time lapse between excitation and emission times, increases with the recombination distance. In Ref. [29] ehIR are understood from non-classical pathways, since while the mean position of the electron and hole wavefunctions are distant, dispersion leads to the overlap of the wavefunctions. Threfore, ehIR at larger distances require a larger wavepacket dispersion and, thus, a larger excursion time. Results in Fig. 2(c) show excursion times of the order of 1.5 cycles for ehIR recombining at 172 Å (β_i).

Note that the wavepacket dispersion rate is nearly six times larger than the one reported for hBN in [29]. This enhanced dispersion suggests that the excited electron-hole wavepackets are more localized in our case, therefore the dispersion rate is larger. We interpret this as consequence of the different excitation mechanisms for each species. In graphene, the non-adiabatic electron-hole excitation results in a broad wavepacket in the reciprocal space, around the Dirac points. In contrast, tunnel excitation, as is the case of hBN, is very sensitive to the band gap, therefore resulting in narrower wavepackets in the reciprocal space around the gap minima.

Finally, in Fig. 3 we show a comparative analysis of the role of ehPR against ehIR for different driving peak intensities. According to the current understanding of HHG in solids, the frequency of the harmonic radiation is given by the energy gap at the time of recombination of the electron-hole pair. Since the trajectories quiver in the reciprocal space with an amplitude $(q_e\mathbf{A}/c)$, the harmonic *cutoff* frequency is expected at the maximum gap energy during this excursion. For the two cases represented in Fig. 3, the maximum gap is reached at the turning point $(2q_e\mathbf{A}_0/c)$, $\mathbf{A}_0$ being the amplitude of the vector potential. This maximum quivering for each case is represented in the energy band representation in the insets of Fig. 3. According to this, the prediction for the harmonic *cutoff* frequency is the 15th order ($\simeq$ 6 eV) for a peak intensity of 1.3×10^{11} (Fig. 3(a)), and the 43rd order ($\simeq$ 18 eV) for a peak intensity of 2×10^{12} (Fig. 3(b)), which agrees with the corresponding time-frequency analyses. Figure 3 also shows the prediction of the harmonic emission from the semiclassical SPAM for ehPR (red) and ehIR at distances of 86 Å (green) and 172 Å (grey). As a main observation, we can see that in all cases, ehIR are necessary to reproduce the harmonic emission, specially at longer times. Note that the quiver trajectory of electrons and holes in the reciprocal space is the same for ehPR and ehIR. However, by relaxing the constraint of zero distance at recombination, ehIR harvest the full potential harmonic emission during the quivering, making it possible the emission of the maximum *cutoff* frequency in situations excluded by the ehPR's overlapping constrain.

Optics EXPRESS

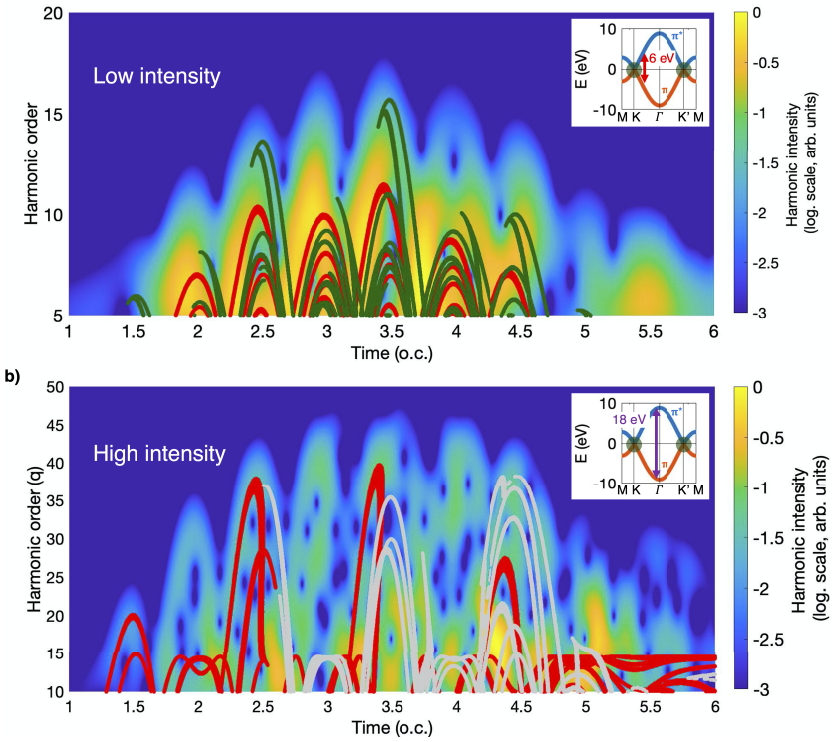

Fig. 3. Time-frequency analysis of the harmonic emission corresponding to two different peak intensities, 1.3×10^{11} W/cm^2 (a) and 2.0×10^{12} W/cm^2 (b), with the same length duration and central wavelength as in the previous figures. For the scan of the spectrum we have used a Gaussian mask of 2.5 ω_0 in (a), and 4 ω_0 in (b). In both panels we plot the frequency of the harmonic emission corresponding to ehPR (red) and to ehIR recombining at 86 Å (green) for (a) and at 172 Å (grey) for (b).

4. Conclusion

We have presented quantum calculations and classical analysis of HHG in single-layer graphene. A comparative analysis with the results of HHG from atoms reveals the extraordinary complex nature of the process in the solid layer. The main trends of the characteristics of this complex emission can be associated with the particular mechanism of HHG in graphene, in which the electron-hole pair excitation is not associated with the maxima of the driving field amplitude. However, our study demonstrates that still relevant spectral features are connected with non-classical recollisions —the so-called *imperfect* recollisions— where the electron-hole pair can recombine even when the classical trajectories do no overlap. We have found that these *imperfect* recollisions typically contribute to the harmonic emission at increasing delayed times for longer recombination distances. These time delays, which are connected with the spreading of the electron and hole wavefunctions to the recombination distance, are significantly larger for graphene. We interpret this result as the consequence of the linear dispersion relation near the Dirac points.

Funding. European Research Council (851201); Ministerio de Educación, Cultura y Deporte (FPU18/03348); FEDER funds (SA287P18); Junta de Castilla y León (SA287P18); Ramón y Cajal (RYC-2017-22745); Ministerio de Ciencia, Innovación y Universidades (PID2019-106910GB-100).

Optics EXPRESS

Acknowledgments. We acknowledge support from the European Research Council (ERC) under the European Union's Horizon 2020 research and innovation programme (grant agreement No. 851201).

Disclosures. "The authors declare no conflicts of interest."

Data availability. Data underlying the results presented in this paper are not publicly available at this time but may be obtained from the authors upon reasonable request.

References

1. A. McPherson, G. Gibson, H. Jara, U. Johann, T. S. Luk, I. A. McIntyre, K. Boyer, and C. K. Rhodes, "Studies of multiphoton production of vacuum-ultraviolet radiation in the rare gases," J. Opt. Soc. Am. B **4**(4), 595–601 (1987).
2. M. Ferray, A. L'Huillier, X. F. Li, L. A. Lompre, G. Mainfray, and C. Manus, "Multiple-harmonic conversion of 1064 nm radiation in rare gases," J. Phys. B: At., Mol. Opt. Phys. **21**(3), L31–L35 (1988).
3. F. Krausz and M. Ivanov, "Attosecond physics," Rev. Mod. Phys. **81**(1), 163–234 (2009).
4. T. Popmintchev, M. C. Chen, D. Popmintchev, P. Arpin, S. Brown, S. Alisauskas, G. Andriukaitis, T. Balciunas, O. Mücke, A. Pugzlys, A. Baltuska, B. Shim, S. E. Schrauth, A. Gaeta, C. Hernández-García, L. Plaja, A. Becker, A. Jaron-Becker, M. M. Murnane, and H. C. Kapteyn, "Bright coherent ultrahigh harmonics in the kev x-ray regime from mid-infrared femtosecond lasers," Science **336**(6086), 1287–1291 (2012).
5. L. Plaja, R. Torres, and A. Zaïr, "Attosecond physics," in *Attosecond Measurements and Control of Physical Systems*, (Springer-Verlag, 2013).
6. S. Ghimire and D. A. Reis, "High-harmonic generation from solids," Nat. Phys. **15**(1), 10–16 (2019).
7. X. Shi, C. T. Liao, Z. Tao, E. Cating-Subramanian, M. M. Murnane, C. Hernández-García, and H. C. Kapteyn, "Attosecond light science and its application for probing quantum materials," J. Phys. B: At., Mol. Opt. Phys. **53**(18), 184008 (2020).
8. K. J. Schafer, B. Yang, L. F. DiMauro, and K. C. Kulander, "Above threshold ionization beyond the high harmonic cutoff," Phys. Rev. Lett. **70**(11), 1599–1602 (1993).
9. K. S. Budil, P. Salières, A. L'Huillier, T. Ditmire, and M. D. Perry, "Influence of ellipticity on harmonic generation," Phys. Rev. A **48**(5), R3437–R3440 (1993).
10. C. Hernández-García, J. A. Pérez-Hernández, T. Popmintchev, M. M. Murnane, H. C. Kapteyn, A. Jaron-Becker, A. Becker, and L. Plaja, "Zeptosecond high harmonic kev x-ray waveforms driven by midinfrared laser pulses," Phys. Rev. Lett. **111**(3), 033002 (2013).
11. C. Hernández-García and L. Plaja, "Resolving multiple rescatterings in high-order-harmonic generation," Phys. Rev. A **93**(2), 023402 (2016).
12. P. C. Li, Y. L. Sheu, H. Z. Jooya, X. X. Zhou, and S. I. Chu, "Exploration of laser-driven electron-multirescattering dynamics in high-order harmonic generation," Sci. Rep. **6**(1), 32763 (2016).
13. J. Tate, T. Auguste, H. G. Muller, P. Salières, P. Agostini, and L. F. DiMauro, "Scaling of wave-packet dynamics in an intense midinfrared field," Phys. Rev. Lett. **98**(1), 013901 (2007).
14. M. V. Frolov, N. L. Manakov, and A. F. Starace, "Wavelength scaling of high-harmonic yield: Threshold phenomena and bound state symmetry dependence," Phys. Rev. Lett. **100**(17), 173001 (2008).
15. J. A. Pérez-Hernández, L. Roso, and L. Plaja, "Harmonic generation beyond the strong-field approximation: the physics behind the short-wave-infrared scaling laws," Opt. Express **17**(12), 9891–9903 (2009).
16. S. Ghimire, A. D. DiChiara, E. Sistrunk, P. Agostini, L. F. DiMauro, and D. A. Reis, "Observation of high-order harmonic generation in a bulk crystal," Nat. Phys. **7**(2), 138–141 (2011).
17. H. Liu, Y. Li, Y. You, S. Ghimire, T. F. Heinz, and D. A. Reis, "High-harmonic generation from an atomically thin semiconductor," Nat. Phys. **13**(3), 262–265 (2017).
18. T. T. Luu, M. Garg, S. Y. Kruchinin, A. Moulet, M. T. Hassan, and E. Goulielmakis, "Extreme ultraviolet high-harmonic spectroscopy of solids," Nature **521**(7553), 498–502 (2015).
19. M. Hohenleutner, F. Langer, O. Schubert, M. Knorr, U. Huttner, S. W. Koch, M. Kira, and R. Huber, "Real-time observation of interfering crystal electrons in high-harmonic generation," Nature **523**(7562), 572–575 (2015).
20. A. A. Lanin, E. A. Stepanov, A. B. Fedotov, and A. M. Zheltikov, "Mapping the electron band structure by intraband high-harmonic generation in solids," Optica **4**(5), 516–519 (2017).
21. O. Schubert, M. Hohenleutner, F. Langer, B. Urbanek, C. Lange, U. Huttner, D. Golde, T. Meier, M. Kira, S. W. Koch, and R. Huber, "Sub-cycle control of terahertz high-harmonic generation by dynamical bloch oscillations," Nat. Photonics **8**(2), 119–123 (2014).
22. N. Tancogne-Dejean and A. Rubio, "Atomic-like high-harmonic generation from two-dimensional materials," Sci. Adv. **4**(2), eaao5207 (2018).
23. A. García-Cabrera, C. Hernández-García, and L. Plaja, "Ultrafast sub-nanometer matter-wave temporal talbot effect," New J. Phys. **23**(9), 093011 (2021).
24. G. Vampa, C. R. McDonald, G. Orlando, D. D. Klug, P. B. Corkum, and T. Brabec, "Theoretical analysis of high harmonic generation in solids," Phys. Rev. Lett. **113**(7), 073901 (2014).
25. G. Ndabashimiye, S. Ghimire, M. Wu, D. A. Browne, K. J. Schafer, M. B. Gaarde, and D. A. Reis, "Solid-state harmonics beyond the atomic limit," Nature **534**(7608), 520–523 (2016).
26. I. Floss, C. Lemell, G. Wachter, V. Smejkal, S. A. Sato, X. M. Tong, K. Yabana, and J. Burgdörfer, "*Ab initio* multiscale simulation of high-order harmonic generation in solids," Phys. Rev. A **97**(1), 011401 (2018).

Optics EXPRESS

27. T. Higuchi, M. I. Stockman, and P. Hommelhoff, "Strong-field perspective on high-harmonic radiation from bulk solids," Phys. Rev. Lett. **113**(21), 213901 (2014).
28. T. T. Luu and H. J. Wörner, "High-order harmonic generation in solids: A unifying approach," Phys. Rev. B **94**(11), 115164 (2016).
29. L. Yue and M. B. Gaarde, "Expanded view of electron-hole recollisions in solid-state high-order harmonic generation: Full-brillouin-zone tunneling and imperfect recollisions," Phys. Rev. A **103**(6), 063105 (2021).
30. O. Zurrón, A. Picón, and L. Plaja, "Theory of high-order harmonic generation for gapless graphene," New J. Phys. **20**(5), 053033 (2018).
31. O. Zurrón-Cifuentes, R. Boyero-García, C. Hernández-García, and L. Plaja, "High harmonic generation in armchair carbon nanotubes," Opt. Express **28**(13), 19760–19771 (2020).
32. N. Yoshikawa, T. Tamaya, and K. Tanaka, "High-harmonic generation in graphene enhanced by elliptically polarized light excitation," Science **356**(6339), 736–738 (2017).
33. S. Jiang, H. Wei, J. Chen, C. Yu, R. Lu, and C. D. Lin, "Effect of transition dipole phase on high-order-harmonic generation in solid materials," Phys. Rev. A **96**(5), 053850 (2017).
34. C. Liu, Y. Zheng, Z. Zeng, and R. Li, "Driving-laser ellipticity dependence of high-order harmonic generation in graphene," Phys. Rev. A **97**(6), 063412 (2018).
35. O. Zurrón-Cifuentes, R. Boyero-García, C. Hernández-García, A. Picón, and L. Plaja, "Optical anisotropy of non-perturbative high-order harmonic generation in gapless graphene," Opt. Express **27**(5), 7776–7786 (2019).
36. Z. Chen and R. Qin, "Circularly polarized extreme ultraviolet high harmonic generation in graphene," Opt. Express **27**(3), 3761–3770 (2019).
37. R. E. F. Silva, A. Jimenez-Galan, B. Amorim, O. Smirnova, and M. Ivanov, "Topological strong-field physics on sub-laser-cycle timescale," Nat. Photonics **13**(12), 849–854 (2019).
38. M. S. Mrudul and G. Dixit, "High-harmonic generation from monolayer and bilayer graphene," Phys. Rev. B **103**(9), 094308 (2021).
39. F. Dong, Q. Xia, and J. Liu, "Ellipticity of the harmonic emission from graphene irradiated by a linearly polarized laser," Phys. Rev. A **104**(3), 033119 (2021).
40. D. Baykusheva, A. Chacón, J. Lu, T. P. Bailey, J. A. Sobota, H. Soifer, P. S. Kirchmann, C. Rotundu, C. Uher, T. F. Heinz, D. A. Reisnd, and S. Ghimire, "All-Optical Probe of Three-Dimensional Topological Insulators Based on High-Harmonic Generation by Circularly Polarized Laser Fields," Nano Lett. **21**(21), 8970–8978 (2021).
41. S. A. Sato, H. Hirori, Y. Sanari, Y. Kanemitsu, and A. Rubio, "High-order harmonic generation in graphene: Nonlinear coupling of intraband and interband transitions," Phys. Rev. B **103**(4), L041408 (2021).
42. R. Boyero-García, O. Zurrón-Cifuentes, L. Plaja, and C. Hernández-García, "Transverse phase matching of high-order harmonic generation in single-layer graphene," Opt. Express **29**(2), 2488–2500 (2021).
43. L. Yue and A. M. B. Gaarde, "Imperfect recollisions in high-harmonic generation in solids," Phys. Rev. Lett. **124**(15), 153204 (2020).
44. L. Li, P. Lan, X. Zhu, T. Huang, Q. Zhang, M. Lein, and P. Lu, "Reciprocal-space-trajectory perspective on high-harmonic generation in solids," Phys. Rev. Lett. **122**(19), 193901 (2019).
45. S. Reich, C. Thomsen, and J. Maultzsch, *Carbon Nanotubes: Basic concepts and physical properties* (Wiley-VCH, 2004).
46. M. Breusing, C. Ropers, and T. Elsaesser, "Ultrafast carrier dynamics in graphite," Phys. Rev. Lett. **102**(8), 086809 (2009).
47. M. Bellini, C. Lyngå, A. Tozzi, M. B. Gaarde, T. W. Hänsch, A. L'Huillier, and C. Wahlström, "Temporal coherence of ultrashort high-order harmonic pulses," Phys. Rev. Lett. **81**(2), 297–300 (1998).
48. M. B. Gaarde, F. Salin, E. Constant, P. Balcou, K. J. Schafer, K. C. Kulander, and A. L'Huillier, "Spatiotemporal separation of high harmonic radiation into two quantum path components," Phys. Rev. A **59**(2), 1367–1373 (1999).
49. A. Zaïr, M. Holler, A. Guandalini, F. Schapper, J. Biegert, L. Gallmann, U. Keller, A. S. Wyatt, A. Monmayrant, I. A. Walmsley, E. Cormier, T. Auguste, J. P. Caumes, and P. Salières, "Quantum path interferences in high-order harmonic generation," Phys. Rev. Lett. **100**(14), 143902 (2008).
50. C. Hernández-García and L. Plaja, "Off-axis compensation of attosecond pulse chirp," J. Phys. B: At., Mol. Opt. Phys. **45**(7), 074021 (2012).
51. S. Carlström, J. Preclíková, E. Lorek, E. W. Larsen, C. M. Heyl, D. Paleček, D. Zigmantas, K. J. Schafer, M. B. Gaarde, and J. Mauritsson, "Spatially and spectrally resolved quantum path interference with chirped driving pulses," New J. Phys. **18**(12), 123032 (2016).

4.2 Transverse harmonic phase-matching in single-layer graphene

The objective of this work was to present, to the best of our knowledge for the first time, a numerical study of HHG in single-layer graphene from a macroscopic perspective. In particular, we aimed to explore the influence of *transverse phase-matching* in the target harmonic emission.

In section 3.2.1 we introduced the relevance of phase-matching in HHG in gases. In order to obtain a constructive interference of all the emissions produced in the target, the phase of the locally radiated harmonic field must interfere constructively in the far field. We can divide the phase-mismatching sources into longitudinal and transverse ones. Longitudinal phase-matching defined in Eq. 3.24 takes into account the phase-mismatch between the harmonics emitted along the propagation axis. In this case, the propagation of the driving field along the gas determines the phase-matching conditions. Its focusing geometry, or the variation in the refractive index due to the ionized electrons are some phenomena that determine the amplitude and phase properties of the pulse as it propagates in the gas. In the other hand, *transverse phase-matching* defined in Eq. 3.25, stems from the influence of the driver's transverse intensity distribution on the phase of the harmonic field. Commonly, driving fields are described by spatial profiles similar to a Gaussian beams. In this case, the intensity decreases with the distance to be beam axis, therefore the phase of the harmonics emitted in the transversal plane varies, and affects the interference in the macroscopic harmonic build up from the target [74]. In Fig. 4.2, C. Hernandez-García and coworkers showed the spatial distribution of the far-field phase of the 19th harmonic emitted from the different the points of the gas target, using a sin^2 envelope pulse of 2.9 cycles full width half maximum (FWHM), 800nm wavelength and $1.57 \times 10^{14} W/cm^2$ peak intensity. They defined a transverse coherence length, L^{coh}, as the transverse distance between two consecutive target positions whose emissions interfere destructively.

While HHG in gases depends strongly of both phase-mismatch sources (longitudinal and transverse), in monolayer systems such as graphene, the longitudinal phase-matching can be neglected due to the nearly atomic thickness of the layer, and

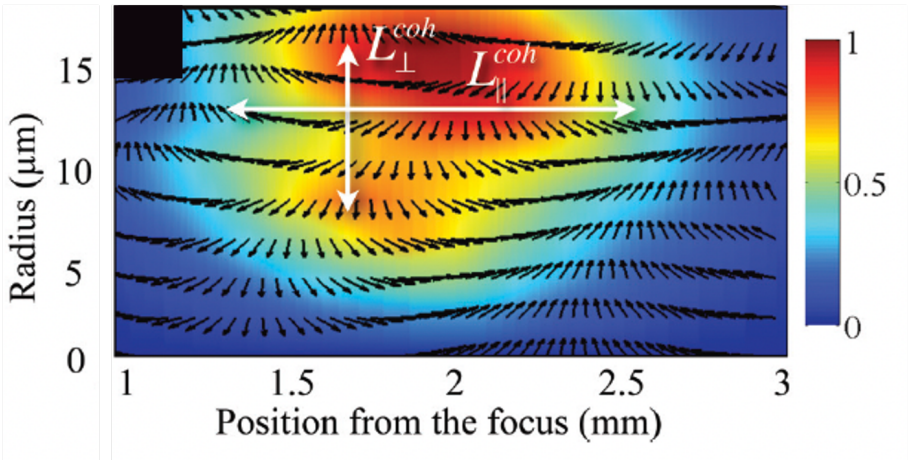

FIGURE 4.2: Spatial map corresponding to the 19th harmonic amplitude produced in a hydrogen gas jet placed after the focus position. The black arrows represent the harmonic phase by the angle. $L_\perp^{coh}$ and $L_\perp^{coh}$ are the longitudinal and transverse coherence length, respectively. Driving field is a sin^2 envelope of 2.9 cycles FWHM, with $1.57 \times 10^{14} W/cm^2$ peak intensity and centered at 800 nm. Figure adapted from [74].

the only relevant phase matching source into play is the *transverse phase-matching*.

In order to study in this work the macroscopic harmonic emission from single-layer graphene, we model a discretized layer with a random distribution of regions, each with a sufficiently large number of graphene primitive cells, so that the assumption of a continuous Brillouin zone remain valid. On the other side, the size of these regions are smaller than the fundamental wavelength of the external field, therefore, in each region the driving field can be assumed as homogeneous. We consider a linearly polarized Gaussian driving beam, as it is the most commonly used in experiments. The macroscopic emission is the superposition of the contributions for each of these regions, which are propagated to a far-field detector following the same procedure as in section 3.2.2. In order to spot the consequences of the *transverse phase-matching*, we have compared the total harmonic emission when the local contributions are added coherently and incoherently. The first result of this article is that, the harmonic efficiency is higher in the incoherent than in the coherent case. The second relevant result is that not all regions of the target contribute to the macroscopic harmonic emission. In particular we have identified that *transverse phase matching* favors the emission from a ringed region around the driver's beam axis.

Resumen

According to the requirements of the University of Salamanca, the Spanish version of the abstract is:

La eficiencia de la generación de armónicos de orden elevado (HHG) en un caso macroscópico está fuertemente ligado al correspondiente acuerdo de fase de las contribuciones que vienen de los emisores microscópicos. Nosotros desarrollamos un modelo teórico combinado micro+macroscópico que nos permite distinguir la relevancia del acuerdo de fase de los armónicos de orden elevados en una lámina de grafeno. Para un pulso incidente Gausiano, nuestras simulaciones muestran que la parte relevante de la emisión de HHG está reducido espacialmente a un anillo de acuerdo de fase alrededor del eje del haz. Este notable hallazgo es una consecuencia directa del comportamiento no perturbativo de HHG en grafeno –donde la eficiencia de los armónicos escala de manera similar a lo ya observado en gases– y conecta la parte micoscópica y macroscópica en HHG en una lámina de grafeno.

Research Article | Vol. 29, No. 2 / 18 January 2021 / Optics Express 2488
Optics EXPRESS

Transverse phase matching of high-order harmonic generation in single-layer graphene

ROBERTO BOYERO-GARCÍA,* OSCAR ZURRÓN-CIFUENTES, LUIS PLAJA, AND CARLOS HERNÁNDEZ-GARCÍA

Grupo de Investigación en Aplicaciones del Láser y Fotónica, Departamento de Física Aplicada, Universidad de Salamanca, E- 37008 Salamanca, Spain
*robertobg@usal.es

Abstract: The efficiency of high-harmonic generation (HHG) from a macroscopic sample is strongly linked to the proper phase matching of the contributions from the microscopic emitters. We develop a combined micro+macroscopic theoretical model that allows us to distinguish the relevance of high-order harmonic phase matching in single-layer graphene. For a Gaussian driving beam, our simulations show that the relevant HHG emission is spatially constrained to a phase-matched ring around the beam axis. This remarkable finding is a direct consequence of the non-perturbative behavior of HHG in graphene—whose harmonic efficiency scaling is similar to that already observed in gases— and bridges the gap between the microscopic and macroscopic HHG in single-layer graphene.

1. Introduction

Since its discovery in the late 80s [1,2], high-harmonic generation (HHG) has turned out to be a remarkably rich process in nonlinear optics. The interaction of intense femtosecond laser pulses with an atomic, molecular, or solid target drives electrons to a non-perturbative dynamics, resulting in the generation of coherent high-frequency radiation, extending from extreme ultraviolet to soft x-rays [3]. High-frequency harmonics are emitted in the form of ultrashort pulses, with temporal durations at the attosecond timescale [4,5].

While the vast majority of studies and applications of HHG have been developed in the context of atomic and molecular targets, its demonstration in solids targets [6] has boosted a considerable interest in the recent years. In atoms and molecules, HHG is well understood in semiclassical terms [7]: an electronic wavepacket is ejected from its parent atom through tunnel ionization driven by the laser field. Once in the continuum, the electron is accelerated by the field. Upon reversal of the field amplitude, the electron is driven back to the ion, where it recollides, releasing its kinetic energy as high-frequency harmonics of the driving field. HHG in solid systems follows similar physical mechanisms [8,9]. For the case of finite-gap solids, ionization is replaced by tunnel excitation from the valence to the conduction band, and interband harmonics are radiated upon electron-hole recombination [9]. Up to now, HHG has been observed in different finite-gap solids, such as ZnO, MoS_2, ZnSe, GaSe or SiO_2 [6,10–14]. Low-dimensional systems, as single-layer graphene, have also been recently demonstrated to produce high-order harmonics [15] where, interestingly, tunnel excitation is replaced by an electron-hole pair creation from the non-adiabatic crossings near the Dirac points [16]. Such mechanism leads to the emission of a complex set of electron-hole trajectories responsible for HHG [16–18], very different to those in bulk solids [19]. In addition to the interband contributions, solid systems also present HHG from intraband dynamics [9]. Nowadays many theoretical works have explored HHG in solids at the microscopic level to gain understanding into these dynamics [9,16,20–25], probing that HHG can serve as a unique spectroscopic tool to unveil the structural dynamics of solid materials [13,14].

One of the potential advantages of HHG from solids is the capability to produce brighter harmonics, due to the larger number of emitters involved. The efficiency of the macroscopic

#412639 https://doi.org/10.1364/OE.412639
Journal © 2021 Received 20 Oct 2020; revised 29 Dec 2020; accepted 29 Dec 2020; published 14 Jan 2021

Optics EXPRESS

harmonic emission, however, depends crucially on the phase matching of the microscopic contributions. Phase matching in HHG has been extensively studied in atoms and molecules [26–33], and several theoretical methods have been proposed [34–43]. There are many examples where the emitted harmonic radiation is controlled tuning only macroscopic parameters, such as the isolation of attosecond pulses [44,45], the generation of circularly polarized harmonics [46,47], lenless focusing of high-order harmonics [48,49], or the generation of structured harmonics with custom orbital angular momentum or self-torque properties [50–52], among others. However, up to now few works have theoretically studied the macroscopic picture of HHG in solids. Floss and coworkers [53] coupled ab-initio simulations of the time-dependent density functional theory with the Maxwell equations to study macroscopic effects of HHG in diamond along the propagation direction. The primary effect observed in the macroscopic signal was the production of a cleaner harmonic spectra, an effect that is universally observed in experiments, and which has been previously invoked phenomenologically in theoretical simulations by including short dephasing times [9,13,24]. Moreover, macroscopic HHG in Dirac-Weyl materials such as single-layer graphene, where excitation takes place through the Dirac points, remains unstudied.

One could think that microscopic HHG is a reasonable approximation to the target emission for single-layer graphene, as the propagation length is at the atomic scale. However, HHG is a non-perturbative process and, therefore, the harmonic emission depends strongly on the driving field's intensity. In particular, the harmonic phase of the microscopic emission is substantially affected by the driver's intensity profile. Therefore, in the non-perturbative case, the concept of harmonic phase matching, and the associated coherence length, must be extended to describe also phase differences in the plane transverse to propagation [54]. It has been demonstrated that transverse phase matching in atomic gases plays a relevant role to enhance the HHG efficiency [54], and to shape the temporal [55] or spatial properties [48,49,56] of the high-order harmonics—specially for structured driving fields—, as it is the case when they carry orbital angular momentum [50]. Transverse phase matching should be thus expected to be of paramount importance in HHG in low-dimensional solids, for orthogonal driver incidences, where longitudinal propagation distances are reduced to the atomic size.

In this work we develop theoretical simulations of macroscopic HHG in single-layer graphene, that combine the numerical integration of the time-dependent Schrödinger equation and the electromagnetic field propagator. Our simulations demonstrate that phase matching plays a relevant role in the macroscopic spectrum, despite the two-dimensional nature of graphene. As a main result, we demonstrate that macroscopic HHG in single-layer graphene irradiated by a Gaussian driving beam is effectively confined to a phase-matched ring. This spatial confinement follows from the non-perturbative scaling law of the harmonic efficiencies with the driver intensity, thus being a particular feature of HHG, not found in other photon conversion processes. We thus establish a fundamental connection between the non-perturbative strong-field physics at the microscopic level and the macroscopic HHG in single-layer graphene. Our numerical method and our results pave the route for the complete theoretical study of HHG in other solid systems—such as Dirac-Weyl materials—, or in other configurations—such as the use of structured driving beams—that require the description of the macroscopic picture.

2. Microscopic vs macroscopic HHG in single-layer graphene

2.1. *Theoretical method: time-dependent Schrödinger equation coupled with the electromagnetic field propagator*

Our method integrates both the microscopic and macroscopic description of HHG in single-layer graphene. The calculations at the microscopic level combine the tight-binding description of the valence and conduction bands in graphene with the solution of the time-dependent Schrödinger equation, as depicted in [16].

Optics EXPRESS

We consider a nearest-neighbor tight-binding model to describe the electron dynamics in the periodic potential of graphene. The energy spectrum of the field-free hamiltonian, H_0, consists of two bands, the conduction band (+) and the valence band (-), with energy dispersion $\epsilon_{\pm}(\mathbf{k}) = \pm\gamma|f(\mathbf{k})|$ ($\gamma = 2.97$ eV) in the Brillouin zone, see Figs. 1(a) and (b), with

$$f(\mathbf{k}) = e^{-iak_x/\sqrt{3}}\left(1 + 2e^{i\sqrt{3}ak_x/2}\cos\frac{ak_y}{2}\right), \tag{1}$$

where $a = 2.45$. The Bloch-state wavefunctions can be expressed as:

$$\Phi^{\pm}_{\mathbf{k}}(\mathbf{r}) = \sqrt{\frac{1}{2}}e^{i\mathbf{k}\cdot\mathbf{r}}\begin{pmatrix}\pm 1\\ e^{-i\phi(\mathbf{k})}\end{pmatrix}, \tag{2}$$

where $\phi(\mathbf{k})$ is the argument of the complex function $f(\mathbf{k})$. The time-dependent wave function can then be expressed as a superposition of the eigenstates described by Eq. (2):

$$\Psi(\mathbf{r},t) = \int \Psi_{\mathbf{k}}(\mathbf{r},t)d\mathbf{k} = \int \left[C_+(\mathbf{k},t)\Phi^+_{\mathbf{k}}(\mathbf{r}) + C_-(\mathbf{k},t)\Phi^-_{\mathbf{k}}(\mathbf{r})\right]d\mathbf{k}. \tag{3}$$

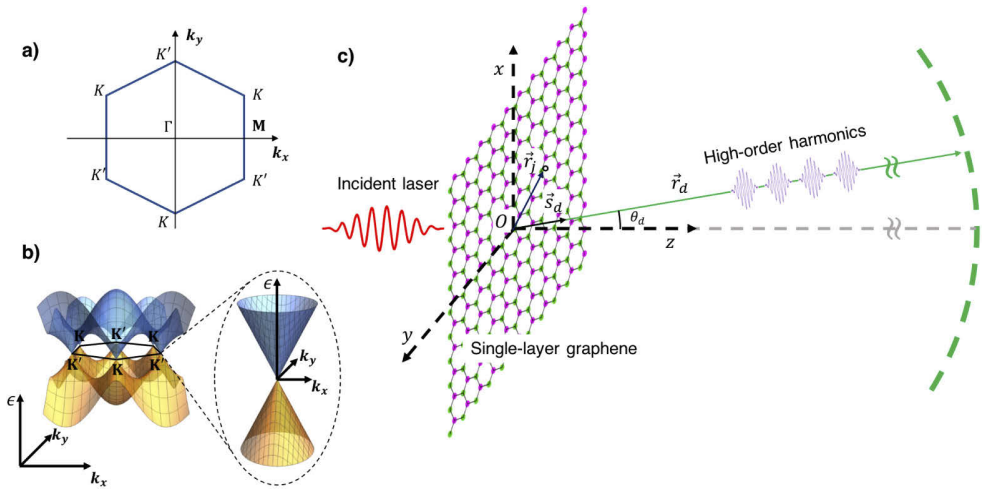

Fig. 1. Scheme of the micro+macroscopic HHG method to compute HHG in single-layer graphene. a) Scheme of graphene's first Brillouin Zone in the reciprocal space. b) Graphene's band structure within the nearest-neighbor tight-binding approximation. The Fermi level is set to zero. The conduction and valence bands correspond to positive and negative values of energy, respectively. Dirac points K and K' are degenerated in energy at the Fermi level. c) Interaction geometry considered. The driving field propagates along the z-direction, perpendicularly to the graphene layer, where high-order harmonics are generated. Afterwards, the high-order harmonics are propagated to a far-field detector placed at position $\mathbf{r}_d$ from the center of the layer (dashed green line).

The interaction of the driving laser pulse $\mathbf{E}(t)$ is described by the time-dependent Hamiltonian $H(t) = H_0 + V_i(t)$ and $V_i(t) = -q_e\mathbf{E}(t)\cdot\mathbf{r}$ is the coupling with the electric field, in the dipole approximation, q_e being the electron charge. We consider a driving field linearly polarized and aimed perpendicularly to the graphene layer, therefore the vector field $\mathbf{E}$(t) is included in the graphene plane. If the duration of the pulse is less than the characteristic carrier scattering time

Optics EXPRESS

~ 10-100 fs [57–59], the electron dynamics can be described by the time-dependent Schrödinger equation [16]:

$$i\hbar\frac{d}{dt}C_+(\boldsymbol{\kappa}_t,t) = \left[\epsilon_+(\boldsymbol{\kappa}_t) - \mathbf{E}(t)\cdot\mathbf{D}(\boldsymbol{\kappa}_t)\right]C_+(\boldsymbol{\kappa}_t,t) - \mathbf{E}(t)\cdot\mathbf{D}(\boldsymbol{\kappa}_t)C_-(\boldsymbol{\kappa}_t,t), \tag{4}$$

$$i\hbar\frac{d}{dt}C_-(\boldsymbol{\kappa}_t,t) = \left[\epsilon_-(\boldsymbol{\kappa}_t) - \mathbf{E}(t)\cdot\mathbf{D}(\boldsymbol{\kappa}_t)\right]C_-(\boldsymbol{\kappa}_t,t) - \mathbf{E}(t)\cdot\mathbf{D}(\boldsymbol{\kappa}_t)C_+(\boldsymbol{\kappa}_t,t), \tag{5}$$

where $\hbar\boldsymbol{\kappa}_t = \hbar\mathbf{k} - q_e\mathbf{A}(t)/c$, being $\mathbf{A}(t)$ the vector potential and c the speed of light, and $\mathbf{D}(\mathbf{k}) = (q_e/2)\partial\phi/\partial\mathbf{k}$ is the interband matrix element , proportional to the Berry connection. We assume all states of the valence band occupied and all states of the conduction band empty before the interaction with the driving pulse, so we take $C_-(\mathbf{k},0) = 1$ and $C_+(\mathbf{k},0) = 0$ as initial conditions. The harmonic emission is then computed from the total dipole acceleration, $\mathbf{a}(t) = \frac{d^2}{dt^2}\mathbf{d}(t)$, with [16]

$$\begin{aligned}\mathbf{d}(t) = \langle\Psi|q_e\mathbf{r}|\Psi\rangle = iq_e\left[C_+^*(\boldsymbol{\kappa}_t,t)\nabla_{\boldsymbol{\kappa}_t}C_+(\boldsymbol{\kappa}_t,t) + C_-^*(\boldsymbol{\kappa}_t,t)\nabla_{\boldsymbol{\kappa}_t}C_-(\boldsymbol{\kappa}_t,t)\right] + \\ \mathbf{D}(\boldsymbol{\kappa}_t)\left[C_-^*(\boldsymbol{\kappa}_t,t)C_+(\boldsymbol{\kappa}_t,t) + C_-(\boldsymbol{\kappa}_t,t)C_+^*(\boldsymbol{\kappa}_t,t)\right].\end{aligned} \tag{6}$$

The intraband contribution to the total acceleration is computed as

$$\mathbf{a}_{\leftrightarrow}(t) = \frac{q_e^2}{\hbar^2}\mathbf{E}(t)\int\left[|C_+(\boldsymbol{\kappa}_t,t)|^2\frac{\partial^2\epsilon_+(\boldsymbol{\kappa}_t)}{\partial\mathbf{k}^2} + |C_-(\boldsymbol{\kappa}_t,t)|^2\frac{\partial^2\epsilon_-(\boldsymbol{\kappa}_t)}{\partial\mathbf{k}^2}\right]d\mathbf{k}. \tag{7}$$

In order to take into account macroscopic effects of HHG, one should solve the wave equation for the electric field $\mathbf{E}$,

$$\nabla^2\mathbf{E} - \frac{1}{c^2}\frac{\partial^2}{\partial t^2}\mathbf{E} = \frac{4\pi}{c^2}\frac{\partial}{\partial t}\mathbf{J}, \tag{8}$$

where $\mathbf{J}$ is the current density. We will adopt a similar strategy as in [41], whose results have been validated with experiments in HHG in atomic and molecular gases (as for example in Refs. [3,44,46,47,51,52,54,55,60]). We consider, therefore, the formal integral solution: $\mathbf{E}(\mathbf{r},t) = \mathbf{E}_0(\mathbf{r},t) + \mathbf{E}_i(\mathbf{r},t)$, where $\mathbf{E}_0(\mathbf{r},t)$ is the laser field, as it propagates in vacuum, and $\mathbf{E}_i(\mathbf{r},t)$ is the field radiated by the accelerated charges in the target,

$$\mathbf{E}_i(\mathbf{r},t) = -\frac{1}{c^2}\int d\mathbf{r'}\frac{1}{|\mathbf{r}-\mathbf{r'}|}\left[\frac{\partial}{\partial t'}\mathbf{J}(\mathbf{r'},t')\right]_{t'=t-|\mathbf{r}-\mathbf{r'}|/c}. \tag{9}$$

The far field radiated by the jth charge in the layer, reaching the detector placed at $\mathbf{r}_d$ (see Fig. 1(c)), can be written as,

$$\mathbf{E}_i^j(\mathbf{r}_d,t) = \frac{1}{c^2}\frac{q_j}{|\mathbf{r}_d - \mathbf{r}_j(0)|}\mathbf{s}_d\times\left[\mathbf{s}_d\times\mathbf{a}_j(t-|\mathbf{r}_d-\mathbf{r}_j(0)|/c)\right], \tag{10}$$

where $\mathbf{a}_j$ is the charge's acceleration, evaluated at the retarded time, and $\mathbf{s}_d$ is the unitary vector pointing towards the detector. We discretize the layer into a random distribution of spatial regions of size much smaller that the driver's wavelength, where the driving field can be assumed homogeneous. These elemental regions, however, still include a number of graphene primitive cells large enough to approximate the Brillouin zone to a continuum. Therefore, the macroscopic signal radiated by the graphene layer can be written as the superposition of the individual contributions $\mathbf{E}_i(\mathbf{r},t) = \sum_{j=1}^{N}\mathbf{E}_i^j(\mathbf{r},t)$, corresponding to each of the regions. The number of elemental regions considered must be large enough to ensure convergence of the radiation at the detector. Note that for a two-dimensional target, Eq. (9) corresponds to the Huygens-Fresnel diffraction formula.

Optics EXPRESS

2.2. Microscopic vs macroscopic results

We consider as driving field a linearly polarized 3 μm-wavelength Gaussian beam of 30 μm beam waist, aimed perpendicularly to the graphene layer, with a peak intensity of 3.5×10^{12} W/cm^2, well below the threshold damage of graphene [61]. The driving field is modelled with a $\sin^2$ envelope of 8 cycles temporal length—corresponding to 28.8 fs full width at half maximum (FWHM)—smaller than the decoherence time due to carrier collisions [57–59].

The microscopic HHG spectrum corresponding to the driving field at the beam center, and obtained from Eq. (6), is shown in Fig. 2(a) (blue line). It presents a non-perturbative plateau of harmonics extending towards a cutoff frequency. As commented before, the generation of this high-frequency radiation is understood in terms of interband and intraband transitions. The contribution of the intraband transitions, calculated from Eq. (7), is shown in the cyan line. It can be concluded, therefore, that interband transitions are the main responsible for the generation of the high-frequency harmonics. As studied in [16], interband HHG is produced by electron-hole pairs created during the non-adiabatic crossings near the Dirac points, followed by their recombination at the emission time. The electron-hole pair can follow complex trajectories before recombining, which gives rise to unstructured spectra.

We have computed the macroscopic response considering the graphene layer at the focus of the Gaussian beam, where the driving field exhibits a transverse intensity profile with uniform phase. The on-axis detected coherent superposition of the microscopic contributions introduced in Section 2.1 is presented in filled-red in Fig. 2(a). In order to highlight the role of phase matching, we also include in the figure the spectrum corresponding to the incoherent addition of the microscopic fields (black line), where the harmonic phase is artificially ignored when obtaining the far-field emission. The coherent addition cleans the spectrum, showing clearly visible harmonic peaks, an effect that has been also observed theoretically in diamond [53], and is universally observed in experiments of HHG in solids [6,10–12]. The coherent addition results also in a weaker harmonic signal compared with the incoherent addition, through all the HHG spectrum, thus demonstrating partial destructive interference due to phase mismatch. Also, the signal at odd harmonic frequencies shows much higher degree of coherence than that of the non-harmonic frequencies. To further show the cleaning of the HHG spectrum obtained when considering transverse phase-matching, we present in Figs. 2(b) and 2(c) the time-frequency analysis for the macroscopic (coherent addition) and microscopic cases, respectively. Though the family of trajectory contributions to HHG in graphene is very complex [16,18], the temporal emission is substantially cleaned when considering the macroscopic result (Fig. 2(c)). The comparison between microscopic and macroscopic cases demonstrates the relevance of considering phase matching in single-layer graphene to reproduce the harmonic signal detected in an experiment.

In addition, the intraband contribution to the coherent macroscopic response is shown in dark red in Fig. 2. Similarly to the microscopic response, the macroscopic response of the high-order harmonics is dominated by the interband transitions.

For the sake of completeness we show in Figs. 2(d) and 2(e) the far-field spatial distribution of the HHG spectrum corresponding to the coherent and incoherent macroscopic additions, respectively. Note that the profiles at zero divergence correspond to the HHG spectra shown in filled-red and black in Fig. 2(a), respectively. The comparison between the spatial profiles reveals that the coherent macroscopic addition results in a much narrower emission of the HHG radiation. In addition, the coherent macroscopic harmonics exhibit a divergence that decreases with the harmonic order, a direct consequence of the non-perturbative behavior of HHG in graphene, as we demonstrate in the next section.

Optics EXPRESS

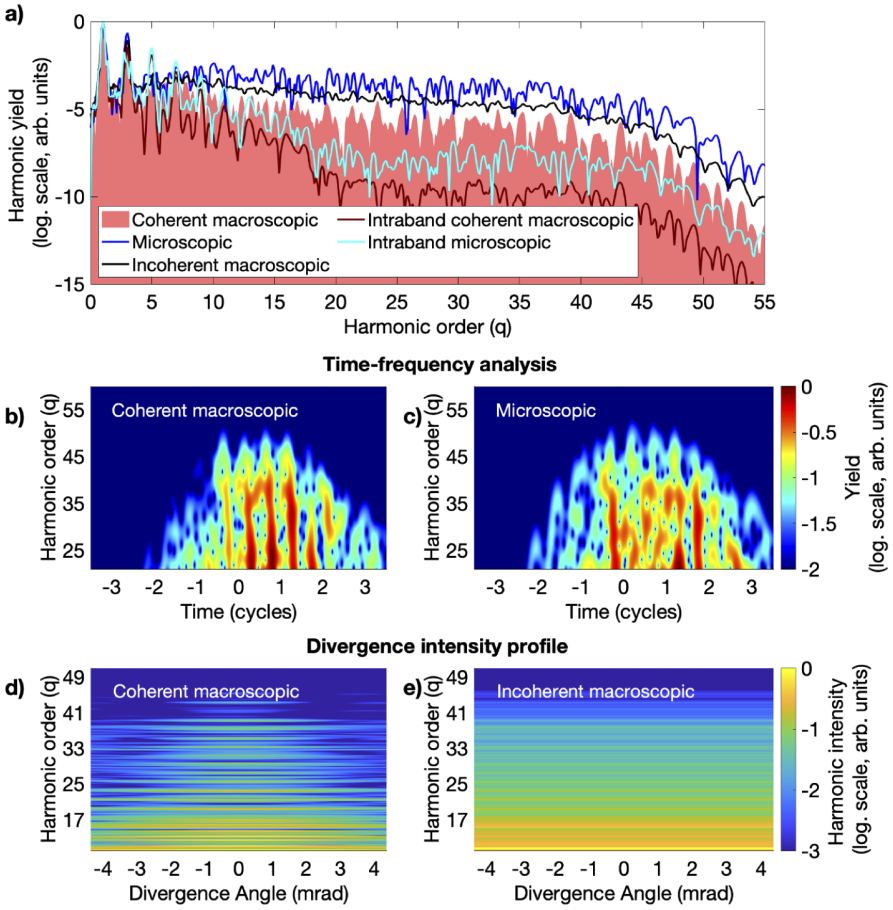

Fig. 2. (a) Comparison between the microscopic and macroscopic HHG spectrum in single-layer graphene irradiated by a 3 μm in wavelength, 28.8 fs FWHM, and 3.5×10^{12} W/cm^2 peak intensity Gaussian beam (30 μm beam waist). The microscopic spectrum obtained at the center of the Gaussian profile is shown as a blue line, the macroscopic HHG spectrum resulting from the coherent (incoherent) addition of the microscopic contributions are shown in filled-red (black line). The spectrum in the microscopic case has been rescaled to the peak at the fundamental frequency of the macroscopic coherent addition. The intraband contributions are shown in solids lines for the microscopic (cyan) and coherent macroscopic (dark red) cases. Time-frequency analysis (log. scale) of the (b) coherent macroscopic and (c) microscopic harmonic emission, performed with a spectral Gaussian mask of width $3\omega_0$, where ω_0 is the frequency of the driving laser pulse. The far-field intensity divergence profile is shown in panels (d) and (e) for the coherent and incoherent macroscopic additions, respectively.

Optics EXPRESS

3. Phase-matched ring and atom-like features in non-perturbative harmonic generation from graphene

In order to gain insight into the build-up of the the macroscopic harmonic signal presented in Fig. 2, we now analyze the high-order emission at different positions along the graphene layer. The qth-order harmonic far-field emission detected on-axis can be found from the Fraunhofer integral

$$U_q' = \frac{2\pi e^{ikz}}{iz\lambda_q} \int U_q(\rho)\rho d\rho, \tag{11}$$

where $U_q(\rho)$ is the microscopic harmonic field emitted at each point of the graphene slab, proportional to the dipole acceleration, Eq. (6). $U_q(\rho)$ inherits the cylindrical symmetry from the driving field, a Gaussian beam. We present in Fig. 3 the contributions of the different radii in Eq. (11), $U_q(\rho)\rho$, in amplitude and phase, i.e., the near-field harmonic emission weighted by the distance to the beam center. Remarkably, Fig. 3(a) shows that the most prominent high harmonic field amplitudes (orders above the 13th in the figure) are radiated from a limited, annular, region around a radius that we denote as ρ_{max}. However, the overall efficiency of this ring depends crucially on the degree of phase matching around it. We plot, therefore, in Fig. 3(b) the phase distribution of $U_q(\rho)$ at the sample. Note that, for the higher-order harmonics, the phase variation shows two distinct regions, slower for smaller radii and faster for larger radii. Interestingly enough, the region enclosed by the ring of maximal amplitudes, ρ_{max}, belongs to the former one, ensuring a smooth variation of the phase and, therefore a proper phase matching condition.

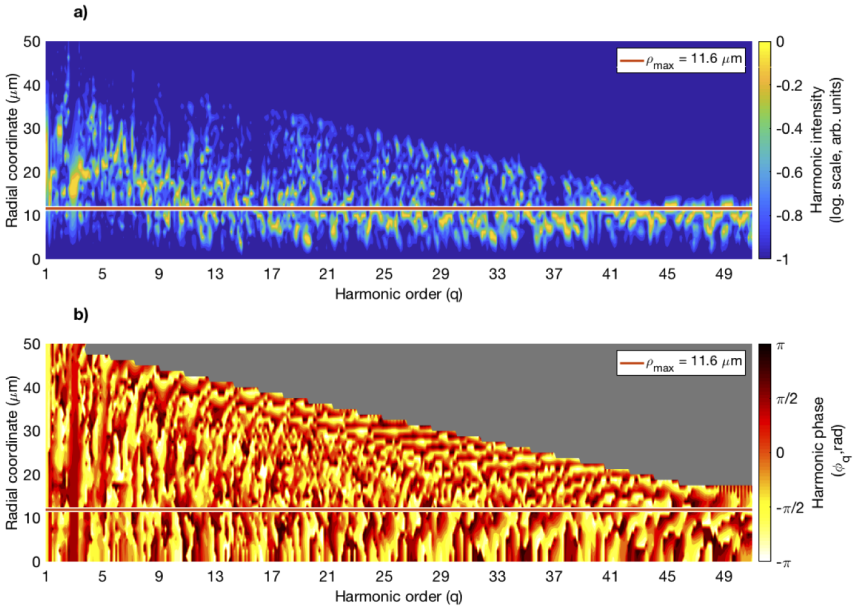

Fig. 3. (a) Harmonic intensity contribution $I_q(\rho)\rho$, and (b) harmonic phase, $\phi_q(\rho)$, of each spatial ring at the graphene layer, considering a Gaussian driving beam profile with beam waist $w_0 = 30$ μm. The harmonic intensity and phase are given by the Fourier transform of Eq. (6) for the same driving pulse parameters as in Fig. 2. The orange solid line indicates the position of the radius of maximum harmonic intensity contribution, $\rho_{\max} = w_0/\sqrt{2p} = 11.6$ μm.

The presence of a phase-matched ring of similar radius for the high-harmonic orders is, in fact, a consequence of the non-perturbative character of the HHG process. To evidence this, we

Optics EXPRESS

will first demonstrate that microscopic HHG follows the same basic non-perturbative features in graphene as in gases. This is a surprising fact since, as mentioned before, the underlying mechanism of HHG in graphene differs in fundamental aspects from that in atoms. On one hand, the electron-hole pair creation is connected with the adiabatic crossing in the Dirac points, instead of tunnelling . On the other hand, harmonics are typically generated by a much more complex set of electron-hole trajectories. Nevertheless, we next see that the amplitude of the harmonics generated at the graphene target can still be approximated using a description valid for atoms [62],

$$U_q(\rho) \propto |U_0(\rho)|^p \, e^{i[q\phi_0(\rho)+\varphi_q(\rho)]}, \tag{12}$$

where q is the harmonic order, $U_0(\rho)e^{i\phi_0(\rho)}$ is the driving field amplitude, $\varphi_q(\rho)$ is the non-perturbative intrinsic phase, and $p<q$ is the power-scaling factor between the harmonic and the driver intensity, for harmonics in the plateau region. In the perturbative case, a similar relation would hold, but with the absence of the intrinsic phase and replacing the scaling factor p by the harmonic order q. Therefore, the non-perturbative nature of HHG is connected with a constant scaling exponent, p, and the additional intrinsic term in the phase.

In order to estimate the behaviour of the power scaling in graphene, we present in Fig. 4(a) the intensity scaling of different harmonic orders (the 19th, 29th and 39th) with the driving field intensity. The logarithmic fit represented in solid lines in Fig. 4(a) allows us to extract the power scaling p, being 2.0, 3.4 and 3.6 for the 19th, 29th and 39th harmonics respectively. In Fig. 4(b) we show the extracted power scaling as a function of the harmonic order for three different driving intensities: 1.3×10^{12} W/cm^2 (dashed red), 3.5×10^{12} W/cm^2 (solid black, same as that used in Fig. 2(a)), and 6.9×10^{12} W/cm^2 (dashed blue). The grey solid line indicates the perturbative power scale behaviour $p = q$. From the results presented in Fig. 4 we can clearly conclude that in HHG in graphene the power scaling is clearly non-perturbative, $p<q$, lying between 2 and 4 in the plateau region, close to the values reported for HHG in atomic gases [49,50,62,63].

Now we can estimate the position of the radius of maximum harmonic contribution, , introduced in Fig. 3. Inserting Eq. (12) in Eq. (11), assuming a Gaussian profile for the driving field at the target with waist w_0, $U_0(\rho) = U_0 e^{-\frac{\rho^2}{w_0^2}}$, and using Eq. (12), the radius of the ring with maximal contribution to the integral Eq. (11) can be found as

$$\frac{\partial\left(U_0^p e^{-p\frac{\rho^2}{w_0^2}}\rho\right)}{\partial\rho} = 0 \longrightarrow \rho_{\max} = \frac{w_0}{\sqrt{2p}}. \tag{13}$$

Note that in the perturbative case ($p = q$) the radii would depend on the harmonic order. In the non-perturbative case, however, p is constant and the high harmonics will be preferentially emitted from the same annular region in the target. For the case shown in Fig. 3, the red line corresponds to ρ_{max} =11.6 μm for p =3.3.

The final HHG efficiency depends on the width of the annular region around ρ_{max} for which the microscopic emissions are properly phase-matched. We show in Fig. 5 the relative phase of the harmonic emission near the ring of maximum efficiency, $\phi_q(\rho) - \phi_q(\rho_{max})$, for the case shown in Fig. 2(a). Note that we only show the phase values at the harmonic peaks, considering as a reference the coherent addition (filled-red line) of Fig. 2(a). The green lines indicate the radii for which the harmonic phase difference is $\pm\pi/2$, relative to the emission at $\rho = \rho_{\max}$, i.e. where the harmonic emission can be considered phase-matched.

The analysis of the intensity and phase profiles in Figs. 3 and 5 allows us to identify the width of the phase-matched graphene ring. The relevance of this ring to the total harmonic emission is illustrated in Fig. 6(a), where we show the HHG emission resulting from the whole graphene layer (filled-red, same as that in Fig. 2(a)), and from rings centered at $\rho = \rho_{\max}$ with thicknesses

Optics EXPRESS

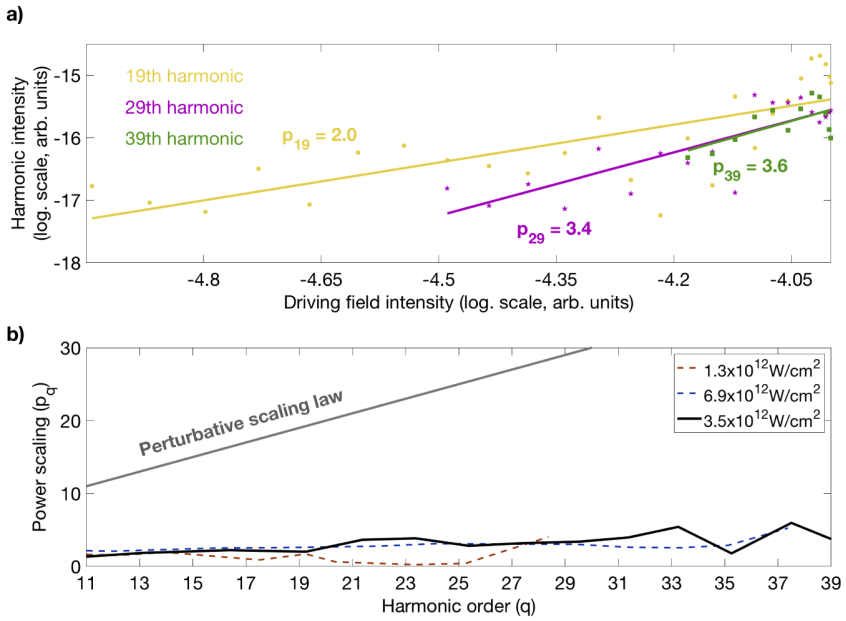

Fig. 4. (a) Intensity scaling of the 19th (yellow), 29th (pink), and 39th (green) harmonics with the driving field intensity (log. scale), obtained through the microscopic calculation of HHG in single-layer graphene. The solid lines indicate the fit for extracting the power scaling p_q. (b) Power scaling p_q as a function of the harmonic order for 1.3×10^{12} W/cm^2 (dashed red), 3.5×10^{12} W/cm^2 (solid black, same intensity as in Fig. 2), and 6.9×10^{12} W/cm^2 (dashed blue) driving intensities. The grey solid line indicates the perturbative power scale behaviour $p_q = q$.

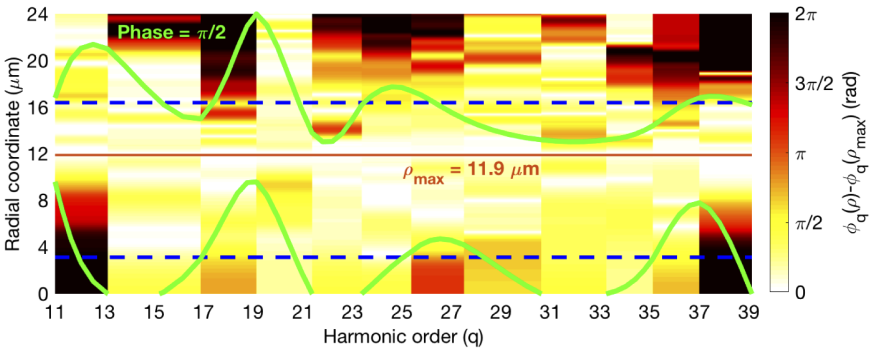

Fig. 5. Relative phase of the harmonics with respect to the emission at $\rho_{\max}$ (orange line). The green lines show the boundaries of the phase-matched region around the circle of maximum efficiency, with phase variation less than $\pi/2$ relative to that at $\rho = \rho_{\max}$, the average is given by the blue-dashed lines.

Optics EXPRESS

of 4 μm (green line) and 12 μm (purple line). These spatial regions are depicted in Fig. 6(b), together with the beam waist of the driving beam (blue-dashed line). While the HHG spectrum of the thin ring differs substantially from that of the whole layer, the thicker one exhibits an excellent agreement. Note that 12 μm thickness is a fair approximation to the phase-matched region identified in Fig. 5.

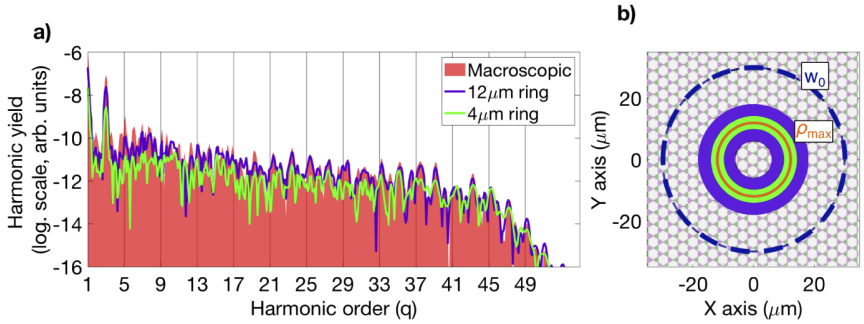

Fig. 6. HHG emission from the phase-matched graphene ring. a) Macroscopic coherent HHG emission resulting from the whole graphene layer (filled-red), and from a ring centered at $\rho = \rho_{\max}$ with a thickness of 4 μm (green line) and 12 μm (purple line). These spatial regions at the graphene-layer are depicted in panel b), where the beam waist of the driving beam ($w_0 = 30$ μm) is indicated by the blue-dashed line.

Finally, we note that the fact that all the harmonics are generated from the same annular region in the graphene layer, implies that the far-field divergence of the harmonics decreases with the harmonic order. This result, that is a consequence of the diffraction of a ring structure with progressive shorter wavelength, was already observed in the results presented in Fig. 2(b).

4. Conclusion

We present a theoretical method to compute both microscopic and macroscopic HHG in solids, similar to what has been used in atomic or molecular targets. We have applied this model to calculate HHG in a two-dimensional layer of graphene, evidencing the connection between the microscopic an macroscopic physics of HHG. On one hand, we observe that the macroscopic HHG spectrum presents cleaner harmonic peaks, as it has been observed in different experiments of HHG in solids. On the other hand, the analysis of the macroscopic HHG emission allows to characterize the non-perturbative dynamics of the microscopic emission, such as the power scaling law. Most interestingly, we show that the macroscopic high-order harmonic emission is dominated by an annular region at the target, with radius approximately constant with the harmonic order. We demonstrate that this finding is a direct consequence of the non-perturbative scaling of the microscopic HHG. Our results show the relevance of considering transverse phase-matching even in 2D solids, when irradiated with intense driving fields. Our work opens the route to study macroscopic effects of HHG in other Dirac-Weyl materials, and in more complex macroscopic geometries. For example, it paves the way in the emerging field of structured laser beams with custom angular momentum properties when considering HHG in solid targets. In such scenarios the macroscopic description of the HHG process is absolutely needed to unveil the up-conversion rules of the angular momentum properties.

Funding. Junta de Castilla y León and FEDER (SA287P18); European Research Council (851201); Ministerio de Ciencia, Innovación y Universidades (FIS2016-75652-P, RYC-2017-22745, PID2019-106910GB-I00).

Acknowledgments. This project has received funding from the European Research Council (ERC) under the European Union's Horizon 2020 research and innovation programme (grant agreement No. 851201). We thankfully

Optics EXPRESS

acknowledge the computer resources at MareNostrum and the technical support provided by Barcelona Supercomputing Center (FI-2020-3-0013).

Disclosures. The authors declare no conflicts of interest.

References

1. A. McPherson, G. Gibson, H. Jara, U. Johann, T. S. Luk, I. A. McIntyre, K. Boyer, and C. K. Rhodes, "Studies of multiphoton production of vacuum-ultraviolet radiation in the rare gases," J. Opt. Soc. Am. B **4**(4), 595–601 (1987).
2. M. Ferray, A. L'Huillier, X. F. Li, L. A. Lompre, G. Mainfray, and C. Manus, "Multiple-harmonic conversion of 1064 nm radiation in rare gases," J. Phys. B: At., Mol. Opt. Phys. **21**(3), L31–L35 (1988).
3. T. Popmintchev, M. C. Chen, D. Popmintchev, P. Arpin, S. Brown, S. Alisauskas, G. Andriukaitis, T. Balciunas, O. Mücke, A. Pugzlys, A. Baltuska, B. Shim, S. E. Schrauth, A. Gaeta, C. Hernández-García, L. Plaja, A. Becker, A. Jaron-Becker, M. M. Murnane, and H. C. Kapteyn, "Bright coherent ultrahigh harmonics in the keV x-ray regime from mid-infrared femtosecond lasers," Science **336**(6086), 1287–1291 (2012).
4. F. Krausz and M. Ivanov, "Attosecond physics," Rev. Mod. Phys. **81**(1), 163–234 (2009).
5. L. Plaja, R. Torres, and A. Zaïr, "Attosecond Physics," in *Attosecond Measurements and Control of Physical Systems* (Springer-Verlag, 2013).
6. S. Ghimire, A. D. DiChiara, E. Sistrunk, P. Agostini, L. F. DiMauro, and D. A. Reis, "Observation of high-order harmonic generation in a bulk crystal," Nat. Phys. **7**(2), 138–141 (2011).
7. K. J. Schafer, B. Yang, L. F. DiMauro, and K. C. Kulander, "Above threshold ionization beyond the high harmonic cutoff," Phys. Rev. Lett. **70**(11), 1599–1602 (1993).
8. G. Ndabashimiye, S. Ghimire, M. Wu, D. A. Browne, K. J. Schafer, M. B. Gaarde, and D. A. Reis, "Solid-state harmonics beyond the atomic limit," Nature **534**(7608), 520–523 (2016).
9. G. Vampa, C. R. McDonald, G. Orlando, D. D. Klug, P. B. Corkum, and T. Brabec, "Theoretical analysis of high harmonic generation in solids," Phys. Rev. Lett. **113**(7), 073901 (2014).
10. H. Liu, Y. Li, Y. S. You, S. Ghimire, T. F. Heinz, and D. A. Reis, "High-harmonic generation from an atomically thin semiconductor," Nat. Phys. **13**(3), 262–265 (2017).
11. A. A. Lanin, E. A. Stepanov, A. B. Fedotov, and A. M. Zheltikov, "Mapping the electron band structure by intraband high-harmonic generation in solids," Optica **4**(5), 516–519 (2017).
12. O. Schubert, M. Hohenleutner, F. Langer, B. Urbanek, C. Lange, U. Huttner, D. Golde, T. Meier, M. Kira, S. W. Koch, and R. Huber, "Sub-cycle control of terahertz high-harmonic generation by dynamical Bloch oscillations," Nat. Photonics **8**(2), 119–123 (2014).
13. T. T. Luu, M. Garg, S. Yu. Kruchinin, A. Moulet, M. Th. Hassan, and E. Goulielmakis, "Extreme ultraviolet high-harmonic spectroscopy of solids," Nature **521**(7553), 498–502 (2015).
14. M. Hohenleutner, F. Langer, O. Schubert, M. Knorr, U. Huttner, S. W. Koch, M. Kira, and R. Huber, "Real-time observation of interfering crystal electrons in high-harmonic generation," Nature **523**(7562), 572–575 (2015).
15. N. Yoshikawa, T. Tamaya, and K. Tanaka, "High-harmonic generation in graphene enhanced by elliptically polarized light excitation," Science **356**(6339), 736–738 (2017).
16. O. Zurrón, A. Picón, and L. Plaja, "Theory of high-order harmonic generation for gapless graphene," New J. Phys. **20**(5), 053033 (2018).
17. O. Zurrón-Cifuentes, R. Boyero-García, C. Hernández-García, A. Picón, and L. Plaja, "Optical anisotropy of non-perturbative high-order harmonic generation in gapless graphene," Opt. Express **27**(5), 7776–7786 (2019).
18. Z. Y. Chen and R. Qin, "Circularly polarized extreme ultraviolet high harmonic generation in graphene," Opt. Express **27**(3), 3761–3770 (2019).
19. Y. S. You, M. Wu, Y. Yin, A. Chew, X. Ren, S. Gholam-Mirzaei, D. A. Browne, M. Chini, Z. Chang, K. J. Schafer, M. B. Gaarde, and S. Ghimire, "Laser waveform control of extreme ultraviolet high harmonics from solids," Opt. Lett. **42**(9), 1816–1819 (2017).
20. M. Wu, S. Ghimire, D. A. Reis, K. J. Schafer, and M. B. Gaarde, "High-harmonic generation from Bloch electrons in solids," Phys. Rev. A **91**(4), 043839 (2015).
21. T. Higuchi, M. I. Stockman, and P. Hommelhoff, "Strong-field perspective on high-harmonic radiation from Bulk Solids," Phys. Rev. Lett. **113**(21), 213901 (2014).
22. P. G. Hawkins, M. Y. Ivanov, and V. S. Yakovlev, "Effect of multiple conduction bands on high-harmonic emission from dielectrics," Phys. Rev. A **91**(1), 013405 (2015).
23. M. Wu, D. A. Browne, K. J. Schafer, and M. B. Gaarde, "Multilevel perspective on high-order harmonic generation in solids," Phys. Rev. A **94**(6), 063403 (2016).
24. T. T. Luu and H. J. Wörner, "High-order harmonic generation in solids: A unifying approach," Phys. Rev. B **94**(11), 115164 (2016).
25. N. Tancogne-Dejean, O. D. Mücke, F. X. Kärtner, and A. Rubio, "Impact of the electronic band structure in high-harmonic generation spectra of solids," Phys. Rev. Lett. **118**(8), 087403 (2017).
26. P. Salières, A. L'Huillier, and M. Lewenstein, "Coherence control of high-order harmonics," Phys. Rev. Lett. **74**(19), 3776–3779 (1995).
27. P. Balcou, P. Salières, A. L'Huillier, and M. Lewenstein, "Generalized phase-matching conditions for high harmonics: The role of field-gradient forces," Phys. Rev. A **55**(4), 3204–3210 (1997).

Optics EXPRESS

28. A. Rundquist, C. G. Durfee III, Z. Chang, C. Herne, S. Backus, M. M. Murnane, and H. C. Kapteyn, "Phase-matched generation of coherent soft x-rays," Science **280**(5368), 1412–1415 (1998).
29. C. G. Durfee III, A. Rundquist, S. Backus, C. Herne, M. M. Murnane, and H. C. Kapteyn, "Phase matching of high-order harmonics in hollow waveguides," Phys. Rev. Lett. **83**(11), 2187–2190 (1999).
30. M. B. Gaarde, J. L. Tate, and K. J. Schafer, "Macroscopic aspects of attosecond pulse generation," J. Phys. B: At., Mol. Opt. Phys. **41**(13), 132001 (2008).
31. T. Popmintchev, M. C. Chen, P. Arpin, M. M. Murnane, and H. C. Kapteyn, "The attosecond nonlinear optics of bright coherent x-ray generation," Nat. Photonics **4**(12), 822–832 (2010).
32. C. Hernández-García and L. Plaja, "Off-axis compensation of attosecond pulse chirp," J. Phys. B: At., Mol. Opt. Phys. **45**(7), 074021 (2012).
33. C. Hernández-García, T. Popmintchev, M. M. Murnane, H. C. Kapteyn, L. Plaja, A. Becker, and A. Jaron-Becker, "Group velocity matching in high-order harmonic generation driven by mid-infrared lasers," New J. Phys. **18**(7), 073031 (2016).
34. I. P. Christov, M. M. Murnane, and H. C. Kapteyn, "Generation and propagation of attosecond x-ray pulses in gaseous media," Phys. Rev. A **57**(4), R2285–R2288 (1998).
35. E. Priori, G. Cerullo, M. Nisoli, S. Stagira, S. De Silvestri, P. Villoresi, L. Poletto, P. Ceccherini, C. Altucci, R. Bruzzese, and C. de Lisio, "Nonadiabatic three-dimensional model of high-order harmonic generation in the few-optical-cycle regime," Phys. Rev. A **61**(6), 063801 (2000).
36. M. Geissler, G. Tempea, and T. Brabec, "Phase-matched high-order harmonic generation in the nonadiabatic limit," Phys. Rev. A **62**(3), 033817 (2000).
37. M. B. Gaarde and K. J. Schafer, "Space-Time Considerations in the Phase Locking of High Harmonics," Phys. Rev. Lett. **89**(21), 213901 (2002).
38. V. Tosa, H. T. Kim, I. J. Kim, and C. H. Nam, "High-order harmonic generation by chirped and self-guided femtosecond laser pulses. I. Spatial and spectral analysis," Phys. Rev. A **71**(6), 063807 (2005).
39. V. S. Yakovlev, M. Ivanov, and F. Krausz, "Enhanced phase-matching for generation of soft X-ray harmonics and attosecond pulses in atomic gases," Opt. Express **15**(23), 15351–15364 (2007).
40. C. Jin, A.-T. Le, and C. D. Lin, "Retrieval of target photorecombination cross sections from high-order harmonics generated in a macroscopic medium," Phys. Rev. A **79**(5), 053413 (2009).
41. C. Hernández-García, J. A. Pérez-Hernández, J. Ramos, E. Conejero Jarque, L. Roso, and L. Plaja, "High-order harmonic propagation in gases within the discrete dipole approximation," Phys. Rev. A **82**(3), 033432 (2010).
42. M. C. Kohler and K. Z. Hatsagortsyan, "Macroscopic aspects of relativistic x-ray-assisted high-order-harmonic generation," Phys. Rev. A **85**(2), 023819 (2012).
43. V. V. Strelkov, V. T. Platonenko, A. F. Sterzhantov, and M. Yu. Ryabikin, "Attosecond electromagnetic pulses: generation, measurement, and application. Generation of high-order harmonics of an intense laser field for attosecond pulse production," Phys.-Usp. **59**(5), 425–445 (2016).
44. M.-C. Chen, C. Mancuso, C. Hernández-García, F. Dollar, B. Galloway, D. Popmintchev, P. C. Huang, B. Walker, L. Plaja, A. A. Jaroń-Becker, A. Becker, M. M. Murnane, H. C. Kapteyn, and T. Popmintchev, "Generation of bright isolated attosecond soft X-ray pulses driven by multicycle midinfrared lasers," Proc. Natl. Acad. Sci. USA **111**(23), E2361–E2367 (2014).
45. C. Hernández-García, T. Popmintchev, M. M. Murnane, H. C. Kapteyn, L. Plaja, A. Becker, and A. Jaron-Becker, "Isolated broadband attosecond pulse generation with near- and mid-infrared driver pulses via time-gated phase matching," Opt. Express **25**(10), 11855–11866 (2017).
46. D. Hickstein, F. Dollar, P. Grychtol, J. Ellis, R. Knut, C. Hernández-García, D. Zusin, C. Gentry, J. M. Shaw, T. Fan, K. Dorney, A. Becker, A. Jaron-Becker, M. M. Murnane, H. C. Kapteyn, and C. G. Durfee, "Non-collinear generation of angularly isolated circularly polarized high harmonics," Nat. Photonics **9**(11), 743–750 (2015).
47. P. C. Huang, C. Hernández-García, J. T Huang, P. Y. Huang, C. H. Lu, L. Rego, D. Hickstein, J. Ellis, A. Jaron-Becker, A. Becker, S. D. Yang, C. Durfee, L. Plaja, H. Kapteyn, M. Murnane, A. Kung, and M. C. Chen, "Polarization control of isolated high-harmonic pulses," Nat. Photonics **12**(6), 349–354 (2018).
48. L. Quintard, V. Strelkov, J. Vabek, O. Hort, A. Dubrouil, D. Descamps, F. Burgy, C. Péjot, E. Mével, F. Catoire, and E. Constant, "Optics-less focusing of XUV high-order harmonics," Sci. Adv. **5**(4), eaau7175 (2019).
49. H. Wikmark, C. Guo, J. Vogelsang, P. W. Smorenburg, H. Coudert-Alteirac, J. Lahl, J. Peschel, P. Rudawski, H. Dacasa, S. Carlstrom, S. Macloa, M. B. Gaarde, P. Johnsson, C. L. Arnold, and A. L'Huillier, "Spatiotemporal coupling of attosecond pulses," Proc. Natl. Acad. Sci. U. S. A. **116**(11), 4779–4787 (2019).
50. C. Hernández-García, J. San Román, L. Plaja, and A. Picón, "Quantum-path signatures in attosecond helical beams driven by optical vortices," New J. Phys. **17**(9), 093029 (2015).
51. K. M. Dorney, L. Rego, N. J. Brooks, J. San Román, C. T. Liao, J. L. Ellis, D. Zusin, C. Gentry, Q. L. Nguyen, J. M. Shaw, A. Picón, L. Plaja, H. C. Kapteyn, M. M. Murnane, and C. Hernández-García, "Controlling the polarization and vortex charge of attosecond high-harmonic beams via simultaneous spin-orbit momentum conservation," Nat. Photonics **13**(2), 123–130 (2019).
52. L. Rego, K. M. Dorney, N. J. Brooks, Q. Nguyen, C. T. Liao, J. San Román, D. E. Couch, A. Liu, E. Pisanty, M. Lewenstein, L. Plaja, H. C Kapteyn, M. M. Murnane, and C. Hernández-García, "Generation of extreme-ultraviolet beams with time-varying orbital angular momentum," Science **364**(6447), eaaw9486 (2019).

Optics EXPRESS

53. I. Floss, C. Lemell, G. Wachter, V. Smejkal, S. A. Sato, X. M. Tong, K. Yabana, and J. Burgdörfer, "Ab initio multiscale simulation of high-order harmonic generation in solids," Phys. Rev. A **97**(1), 011401 (2018).
54. C. Hernández-García, I. J. Sola, and L. Plaja, "Signature of the transversal coherence length in high-order harmonic generation," Phys. Rev. A **88**, 043848 (2013).
55. C. Hernández-García, W. Holgado, L. Plaja, B. Alonso, F. Silva, M. Miranda, H. Crespo, and I. J. Sola, "Carrier-envelope-phase insensitivity in high-order harmonic generation driven by few-cycle laser pulses," Opt. Express **23**(16), 21497–21508 (2015).
56. F. Catoire, A. Ferré, O. Hort, A. Dubrouil, L. Quintard, D. Descamps, S. Petit, F. Burgy, E. Mével, Y. Mairesse, and E. Constant, "Complex structure of spatially resolved high-order- harmonic spectra," Phys. Rev. A **94**(6), 063401 (2016).
57. M. Breusing, C. Ropers, and T. Elsaesser, "Ultrafast Carrier Dynamics in Graphite," Phys. Rev. Lett. **102**(8), 086809 (2009).
58. D. Brida, A. Tomadin, C. Manzoni, Y. J. Kim, A. Lombardo, S. Milana, R. R. Nair, K. S. Novoselov, A. C. Ferrari, G. Cerullo, and M. Polini, "Ultrafast collinear scattering and carrier multiplication in graphene," Nat. Commun. **4**(1), 1987 (2013).
59. J. M. Iglesias, M. J. Martín, E. Pascual, and R. Rengel, "Carrier-carrier and carrier-phonon interactions in the dynamics of photoexcited electrons in graphene," J. Phys.: Conf. Ser. **647**, 012003 (2015).
60. L. Rego, C. Hernández-García, A. Picón, and L. Plaja, "Site-specific tunnel-ionization in high harmonic generation in molecules," New J. Phys. **22**(4), 043012 (2020).
61. A. Roberts, D. Cormode, C. Reynolds, T. Newhouse-Illige, B. J. LeRoy, and A. S. Sandhu, "Response of graphene to femtosecond high-intensity laser irradiation," Appl. Phys. Lett. **99**(5), 051912 (2011).
62. A. L'Huillier, Ph. Balcou, S. Candel, K. J. Schafer, and K. C. Kulander, "Calculations of high-order harmonic generation processes in xenon at 1064 nm," Phys. Rev. A **46**(5), 2778–2790 (1992).
63. L. Rego, J. San Román, A. Picón, L. Plaja, and C. Hernández-García, "Nonperturbative twist in the generation of extreme-ultraviolet vortex beams," Phys. Rev. Lett. **117**(16), 163202 (2016).

4.3 HHG in polycrystalline graphene

In this work we have studied the possibility of characterizing polycrystalline graphene samples via high-order harmonic spectroscopy. In particular, we take advantage of the the graphene's non-linear anisotropy in HHG to study the changes in polarimetry induced by the different domain distributions in the sample.

As we have introduced in previous chapters, single-layer graphene is a unique material with an enormous potential in many technological applications, ranging from biomedicine to sensors and microelectronics. All these implementations require scalable techniques to produce large-area samples of graphene. Practically, most of these single layers are generated by CVD, as previously explained in section 3.3.3. Typical films of graphene produced by CVD have polycrystalline nature, i.e. the graphene samples are composed of single-crystalline domains with different sizes and orientations, forming boundaries between them. In Ref. [49], Huang *et al.* used a DF-TEM technique to characterize a polycrystalline graphene sample grown using CVD. They obtained the grain size and relative rotation distributions shown in Fig. 4.3. Note that, while in many electrical applications graphene's grain boundaries are relevant, such as in transport [84], their influence in HHG can be neglected because they represent a small fraction of the total grain surface.

In order to simulate HHG from polycrystalline graphene, we consider the domain statistics found in [49], where the sample size is 2.5 μm (see Fig. 4.3). We use a linearly-polarized driving field centered at 3 μm, with a sin^2 envelope of 28 fs FWHM and $5 \times 10^{11} W/cm^2$ peak intensity. The small size of the domains compared to the laser pulse wavelength allows us to assume that every grain interacts with the same spatial part of the driving beam. Therefore, following similar distributions as in Fig. 4.3 A) and B), we can theoretically generate samples of polycrystalline graphene with different number of grain sizes and orientations.

A first conclusion applies to polycrystals with large number of grains. In this case, we have found little dependence of the harmonic emission on the driver's polarization tilt. On the other hand, if the polycrystal is formed by a small number of grains, the harmonic polarization deviates from that of the driver. In this case, the system is sensitive to the domain distribution. Repeating this calculation many

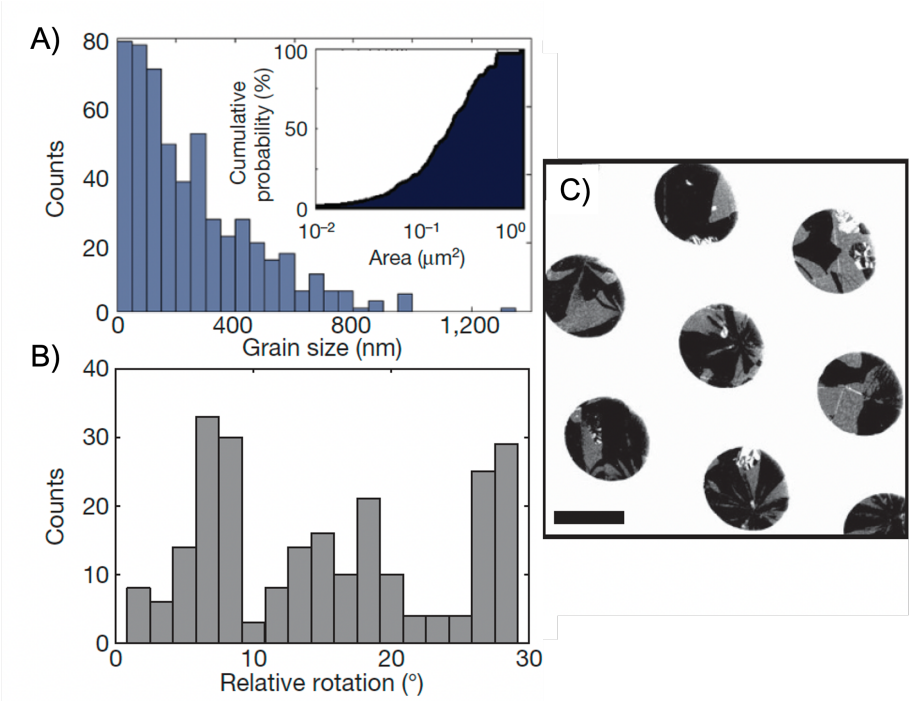

FIGURE 4.3: Characterization of three representative samples using DF-TEM. A) and B) are histogram of grain sizes and their relative rotation, respectively. D) DF-TEM image of different polycrystal areas. Scale bar, 2 μm. Figure adapted from [49].

times with different polycrystal configurations, we found that the standard deviation of the harmonic tilt-angle increases with the harmonic order. We made a map with the standard deviation of the tilt-angle of the 7th harmonic order in terms of the domain size and orientation distribution. While the dependence of the standard deviation of the harmonic tilt with the domain orientation is quite small, this is not the case for the size distributions. We could, therefore, design a proof-of-concept strategy to determine the standard deviation of the domain size distribution from the values of the most frequent grain size and the standard deviation of the harmonic tilt.

Resumen

According to the requirements of the University of Salamanca, the Spanish version of the abstract is:

La actual producción en masa de grandes areas de grafeno se basa fundamentalmente en métodos de deposición química de vapor (CVD). La generación de fronteras, que dividen las muestras de cristal en dominios, es inherente en este tipo de

métodos de fabricación. Estudios recientes han demostrado una fuerte anisotropía en la respuesta no lineal ultrarápida de la lámina de grafeno cuando está sometido a condiciones no perturbativas, un campo láser intenso por debajo del límite de daño. Nosotros proponemos utilizar su anisotropía para caracterizar la distribución de tamaños de los dominios de grafeno en policristales via polarimetría de los órdenes elevados de armónicos. Nuestras resultados simulados demuestran la sensibilidad del estado de polarización de los armónicos a detalles de la distribución de granos del policristal. En particular, mostramos que la rotación en la inclinación de la polarización de los órdenes elevados de armónicos contiene información sobre la distribución de granos en el policristal. Como prueba de concepto, proponemos un método para determinar la desviación estandar de la distribución de tamaños de granos partiendo de los valores más frecuentes de tamaño de grano y la desviación estandar de la rotación de la inclinación de los armónicos a partir de medidas hipotéticas en diferentes policristales generados. Nuestro trabajo muestra la capacidad de la polimetría basada en armónicos de ordene elevado para caracterizar policristales de materiales de dos dimensiones.

Research Article | Vol. 12, No. 9 / 1 Sep 2022 / Optical Materials Express 3543
Optical Materials EXPRESS

High-order harmonic spectroscopy of polycrystalline graphene

ROBERTO BOYERO-GARCÍA,* ANA GARCÍA-CABRERA, OSCAR ZURRÓN-CIFUENTES, CARLOS HERNÁNDEZ-GARCÍA, AND LUIS PLAJA

Grupo de Investigación en Aplicaciones del Láser y Fotónica, Departamento de Física Aplicada, Universidad de Salamanca, E- 37008, Salamanca, Spain
robertobg@usal.es

Abstract: Present mass production of large-area single-layer graphene relies fundamentally on chemical vapor deposition methods. The generation of grain boundaries, which divides the sample into a set of crystalline domains, is inherent to these fabrication methods. Recent studies have demonstrated a strong anisotropy in the ultrafast non-linear response of single-layer graphene when subjected to non-perturbative, intense laser fields below the damage threshold. We propose to exploit this anisotropy to characterize the size distribution of graphene domains in polycrystals via high-order harmonic polarimetry. Our simulation results demonstrate the sensitivity of the harmonic polarization state to details of the polycrystal grain distribution. In particular, we show that the rotation in the polarization tilt of the highest-order harmonics holds information about the grain distribution in the polycrystal. As a proof-of-concept, we propose a method to determine the standard deviation of the grain size distribution from the values of the most frequent grain size and the standard deviation of the harmonic tilt rotation from a set of hypothetical measurements on different polycrystal realizations. Our work reveals the capability of high-order harmonic polarimetry to characterize polycrystalline two-dimensional materials.

1. Introduction

Single-layer graphene (SLG) is a two dimensional –atomic thin– carbon allotrope with extraordinary potential in a variety of fields, ranging from biomedicine to sensors and microelectronics [1]. Industrial applications require large layers of graphene. Chemical vapor deposition (CVD) on metal substrates is one of the most popular choices to fabricate large-area SLG [2]. However, CVD typically leads to polycrystals with grain size and orientation distributions that depend on the fabrication parameters (substrate, growth temperature, hydrogen flow, etc.) [3]. While graphene's electronic properties are degraded by the grain boundaries [4], the smaller fraction of the boundary regions against the total grain surface makes the optical response to be dominated by the inner part of the grain [3]. Grain analysis can be performed using a variety of techniques, either resolving the grain scale (using transmission electron microscopy [3]) or the polycrystal scale (using low-energy electron microscopy [5] or by Raman microscopy [6]).

High-order harmonic generation (HHG) stands as a unique method to produce short-wavelength coherent radiation. This highly non-linear process is triggered by the intense laser-matter interaction driven mainly by infrared and mid-infrared laser pulses. As a result, high-order harmonics of the driving field, extending towards the extreme-ultraviolet or even soft x-rays, are produced [7]. The extraordinary coherence of the process allows tracking the fastest laser-driven electronic dynamics at the attosecond timescales [8]. While HHG was initially explored using gaseous targets [9,10], a substantial interest has recently burgeoned its study in crystalline solids [11].

#468125 https://doi.org/10.1364/OME.468125
Journal © 2022 Received 16 Jun 2022; revised 30 Jul 2022; accepted 1 Aug 2022; published 10 Aug 2022

Optical Materials EXPRESS

The underlying mechanism of HHG in two-dimensional (2D) solids depends strongly on the interaction geometry. On the one hand, for intense p-polarized driving fields at grazing incidence, the process resembles that reported for atoms and molecules [12]: electrons are detached from the crystal's surface, quiver in the continuum, and are finally redirected to collide with the crystal potential, where harmonics are emitted [13]. Interestingly, the detached electron wavefunction preserves the transverse structure imprinted by the crystal potential. These transverse modulations introduce a Talbot revival dynamics at the femtosecond/nanometer scale, whose signature can be resolved in the harmonic spectrum [14]. On the other hand, at normal incidence, the electrons remain in the crystal plane. In such scenario, the driving field generates electron-hole pairs from tunneling excitation at the band gap. Once excited, electrons and holes quiver in reciprocal space following corresponding trajectories in direct space. The harmonic emission occurs from pair recombination when the electron and hole trajectories overlap [15,16], or when they are sufficiently close [17,18]. The corresponding mechanism of HHG in single-layer graphene differs from finite gap solids in the very first step, in which excitation results from the non-adiabatic crossings near the Dirac points [19], instead of tunneling. HHG from other carbon allotropes can be understood through modifications of this basic mechanism [20].

The dynamical details of the coupling of the driving field with the crystal structure (energy dispersion or symmetries) introduce time-resolved signatures in the HHG spectra, that can be unraveled using high-harmonic spectroscopy techniques [21]. Among them, it has been recently demonstrated that crystal symmetries introduce an anisotropic nonlinear response [22–25]. In particular, HHG in graphene yields elliptically polarized harmonics when driven by linearly polarized laser pulses, and viceversa [26–28]. In the recent years, these results have triggered the use of the polarization state of the harmonics as an extension to state-of-the-art high harmonic spectroscopic techniques [29]. Consequently, non-linear optics is at the root of recent proposals for the characterization of 2D or quasi-2D materials [30]. While second harmonic spectroscopy and four-wave mixing are used to determine the number of layers, crystal axis orientation and crystal phase and defects, HHG has been demonstrated to be sensitive to crystal orientation, interlayer coupling and valley structure [31].

In this paper we propose to exploit the graphene's non-linear anisotropic response to characterize the statistical distribution of the domain sizes in polycrystalline graphene. For this purpose, we have implemented HHG simulations in polycrystalline graphene based on the time-dependent Schrödinger equation. We have performed a series of calculations of different polycrystal realizations corresponding to a given grain size and orientation distributions, interacting with a mid-infrared linearly-polarized driving field. For each of these realizations, we compute the polarization properties of the generated harmonics. The statistical analysis for a sufficiently large number of polycrystal calculations shows that the harmonics are emitted with zero mean ellipticity and null rotation of the polarization axis, i.e. the average polarization properties of the harmonics reproduce that of the driving field's. However, we show that the standard deviation of these quantities is sensitive to the grain size distribution. From this, we propose a scheme for the characterization of the grain size distribution knowing the most-frequent grain size and the standard deviation of a series of measurements of the harmonic polarization tilt rotation, as measured from a sample of polycrystals.

2. Theoretical description of HHG in polycristalline single-layer graphene

We consider polycrystal parameters similar to the corresponding to CVD graphene grown on copper films (see method A in [3]). The polycrystal layer is irradiated by a linearly polarized laser pulse centered at 3 μm in wavelength and modeled by a $\sin^2$ envelope of 28 fs full width at half maximum (FWHM) in intensity, and peak intensity of 5×10^{11} W/cm^2 (see Fig. 1a). Each polycrystal presents a typical area of 4.9 μm^2 and is composed by domains whose size and orientation distributions are plotted in Fig. 1, according to Ref. [3]: panel (b) shows the

Optical Materials EXPRESS

grain's size distribution, the most frequent size being 25 nm, with a standard deviation of 275.8 nm, calculated from the best fit to a Gaussian distribution. The black solid line depicts the Gaussian distribution corresponding to the values extracted from the proof-of-principle proposal described in next section. Panels (c) and (d) depict the distribution of the orientation shift between neighboring domains, and the corresponding absolute orientations of the domains in the polycrystal, respectively. The laser beam is aimed perpendicularly to the sample, and we consider the driver's waist larger than the polycrystal size, therefore the driver's intensity profile can be approximated as constant. Note that this is crucial to ensure that all domains are subjected to the same driving field conditions.

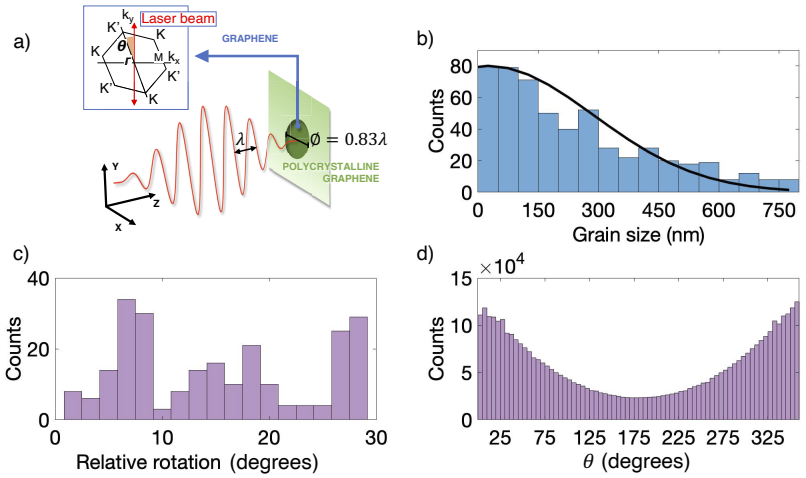

Fig. 1. a) Scheme of the interaction between the driving field and a polycrystal. The driving laser is aimed perpendicularly to the graphene's surface, linearly polarized along the y-axis. The inset represents the first Brillouin Zone of graphene, tilted by an angle θ from the vertical axis, i.e. the driving field's polarization direction. b) Distribution of grain sizes and c) relative grain rotation angles of a polycrystalline graphene grown with CVD, according to [3]. We include in b) the Gaussian distribution resulting from our analysis in section 3. d) Distribution of the absolute angles of rotation of the domains.

Graphene's nonlinear response to intense laser radiation is computed from the integration of the dynamical equations of SLG in the nearest neighbor tight-binding approximation [32]. Following [19] we solve the equations in the oscillatory frame $\boldsymbol{\kappa}_t = \hbar\mathbf{k} - q_e\boldsymbol{\alpha}(t)/c$, where $\mathbf{k}$ are points in the Brillouin Zone, q_e is the electron's charge and $\boldsymbol{\alpha}(t)/c$ is the normalized vector potential of the driving field. Projecting the wavefunction on the Bloch basis of each graphene sublattice (A and B), $\{\phi^A_{\mathbf{k}}, \phi^B_{\mathbf{k}}\}$, the light-induced dipole can be computed as [19]

$$\mathbf{d}(t) = \langle\Psi(t)|q_e\mathbf{r}|\Psi(t)\rangle = i\frac{q_e}{2}\int \left[C^*_A(\boldsymbol{\kappa}_t,t)\nabla_{\mathbf{k}}C_A(\boldsymbol{\kappa}_t,t) + C_B(\boldsymbol{\kappa}_t,t)\nabla_{\mathbf{k}}C_B(\boldsymbol{\kappa}_t,t)\right]d\mathbf{k}, \quad (1)$$

where $C_{A,B}$ are the probability amplitudes of the electron wavefunction in each Bloch basis. The harmonic emission is then calculated from the the dipole acceleration, $\mathbf{a}(t) = \frac{d^2}{dt^2}\mathbf{d}(t)$.

We consider first a set of polycrystals, each built by tiling randomly chosen domains according to the size and orientation distributions shown in Figs. 1(b) to 1c, similar to those reported in [3]. The driving field is linearly polarized along the vertical direction. Therefore, the domain orientation refers to the angle between the grain's $\Gamma - K'$ axis and the vertical axis. If we consider a particular polycrystal realization j in the set, its harmonic emission is computed from the coherent addition of the contributions of the grains. Thus, the j-th polycrystal's dipole

Optical Materials EXPRESS

acceleration is computed as $\mathbf{A}_j(t) = \sum_i^{N_j} \mathbf{a}_i(t)$, where N_j is the number of grains and $\mathbf{a}_i(t)$ is the dipole acceleration in each grain, given by the second derivative of Eq. (1).

We compute the harmonic emission from the j-th polycrystal through the Fourier transform, $\tilde{\mathbf{A}}_j(\omega)$, of the dipole acceleration $\mathbf{A}_j(t)$. Additionally, we determine the polarization state of the harmonics radiated by the j-th polycrystal by calculating the Stokes parameters, $S_k^j(\omega)$, with $k = 0, \ldots, 3$, for each of the Fourier amplitudes $\tilde{\mathbf{A}}_j(\omega)$, as

$$S_0^j(\omega) = \left|\tilde{\mathbf{A}}_{j,\mathbf{x}}(\omega)\right|^2 + \left|\tilde{\mathbf{A}}_{j,\mathbf{y}}(\omega)\right|^2, \tag{2}$$

$$S_1^j(\omega) = \left|\tilde{\mathbf{A}}_{j,\mathbf{x}}(\omega)\right|^2 - \left|\tilde{\mathbf{A}}_{j,\mathbf{y}}(\omega)\right|^2, \tag{3}$$

$$S_2^j(\omega) = \left|\tilde{\mathbf{A}}_{j,\mathbf{a}}(\omega)\right|^2 - \left|\tilde{\mathbf{A}}_{j,\mathbf{b}}(\omega)\right|^2, \tag{4}$$

$$S_3^j(\omega) = \left|\tilde{\mathbf{A}}_{j,\mathbf{r}}(\omega)\right|^2 - \left|\tilde{\mathbf{A}}_{j,\mathbf{l}}(\omega)\right|^2, \tag{5}$$

where (**x**,**y**) is the Cartesian basis, (**a**,**b**) the 45° rotated basis and (**l**,**r**) the circular basis of the space of Jones vectors.

We define the Stokes parameters $S_{q,k}^j$ for a given harmonic order, q, as the integral of $S_k^j(\omega)$ along the interval $\Delta\omega = \pm\omega_0/10$ centered at $q\omega_0$, ω_0 being the driving field's frequency. The ellipticity of each harmonic order and the tilt angle of the major axis is then determined from the Stokes parameters as,

$$\epsilon_q^j = \tan\left[\frac{1}{2}\arctan\left(\frac{S_{q,3}^j}{\sqrt{S_{q,1}^{j^2} + S_{q,2}^{j^2}}}\right)\right], \tag{6}$$

$$\theta_q^j = \frac{\pi}{2} - \frac{1}{2}\arctan\frac{S_{q,2}^j}{S_{q,1}^j}. \tag{7}$$

The characterization of the polycrystal domain-size distribution is done considering a set of 8×10^4 individual polycrystal realizations according to the distributions shown in Fig. 1. The domain rotation is discretized in steps of one degree, and the size distribution in steps of 10 nm. Therefore the number of different domain configurations corresponding to the case of Fig. 1 is about 29000. From each realization, j, we compute the high-order harmonic spectrum, and the ellipticity and the tilt of the different harmonic orders. Finally, we derive statistics of the polarization parameters ϵ_q^j and θ_q^j (mean and deviation), by collecting the results from the complete set of polycrystal realizations.

3. Results and discussion

Figure 2(a) shows the comparison of the harmonic spectrum emitted by a single crystal with that corresponding to a particular polycrystal random realization, j. Note that the harmonic spectrum includes little information on the polycrystal structure. This can be understood since, as it has been recently reported in [27], the efficiency of the higher-order harmonic emission is optimal for graphene rotated $15° + k30°$ $\{k \in \mathbb{Z}\}$ from the driver's polarization axis, dominating over the other orientations. In addition, for the lower-order harmonics, the emission is almost insensitive to the orientation. Due to these reasons and, since the domain orientations span over the whole circle (see Fig. 1(d)), the polycrystal harmonic spectrum barely deviates from that of a single crystal oriented with the driver's polarization axis. Therefore, as first conclusion, monitoring the variations of the harmonic efficiency does not result in an useful strategy for the spectroscopic characterization of the polycrystal grain distribution.

An alternative and more successful strategy for the characterization of the polycristal domain distribution consists in looking at the polarization properties of the generated harmonics, instead

Optical Materials EXPRESS

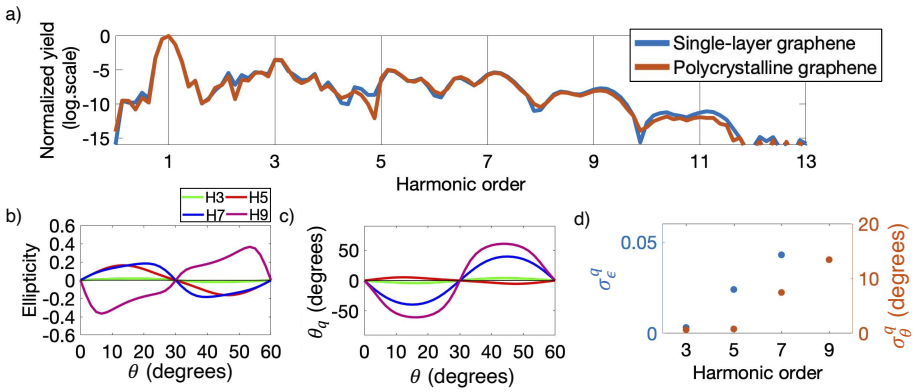

Fig. 2. a) Comparison between the spectra of single-crystal graphene (blue line) and that of a particular realization j of a polycrystal (orange line) according to the domain distributions in Fig. 1. b) and c) show the ellipticity and tilt-angle for harmonics 3th to 9th from a single-crystal graphene in terms of the rotation θ of its $\Gamma - K'$ axis. d) Statistical analysis of the standard deviation of the ellipticity σ_ϵ^q (blue dots) and tilt-angle σ_θ^q (orange dots) for 8×10^4 polycrystal cases with the distributions shown in Fig. 1.

of at the harmonic efficiency. Our computations show that the polarization of the high-order harmonic emission is indeed sensitive to the domain distribution. This stems from the non-linear anisotropy of single-crystal graphene [27]. Figures 2(b) and 2(c) show the dependence of the ellipticity, ϵ_q, and major-axis tilt angle, θ_q, of the 3rd, 5th, 7th and 9th harmonic orders emitted by a single-crystal graphene irradiated with a linearly-polarized driving field, as a function of the crystal's $\Gamma - K'$ axis rotation-angle, θ. In both panels the crystal's orientation spans over $0<\theta<60°$ since, due to the graphene's symmetry, the pattern is repeated periodically for all subsequent angular intervals. Both parameters, ϵ_q and θ_q, are basically unaffected for the lower-order harmonics, i.e. the lower-order harmonics are almost linearly polarized in the same direction as the driver. In contrast, the higher-order harmonics show a substantial deviation from the driver's polarization, as graphene's anisotropy is more pronounced for the highest orders in the HHG spectrum. Note also, in this latter case, that both ellipticity and major-axis tilt-angle show a maximum deviation from the driver's at orientation angles odd-multiples of $\theta = 15°$. In addition, the deviations are symmetric and opposite with respect to $\theta = 30°$ for any harmonic order.

As a consequence of the non-linear anisotropy in single-crystal graphene, the different domains in a polycrystal will radiate high-order harmonics with a distinctive polarization state, depending on their particular orientation. However, note that, for a sufficient number of grains in the polycrystal, the domain orientations will spread over 360° (see Fig. 1(d)). This, together with the opposite symmetry of the non-linear response shown in Figs. 2(b) and 2(c), leads to the expectation that the net polycrystal harmonic emission present the same polarization properties as the driving field. However, for finite-size polycrystals, similar to those in [3], the number of grains is limited to their cumulative area filling the polycrystal's surface. Therefore, in this case, we should expect a residual ellipticity and tilt deviations in the harmonics emitted by the target. Note that the magnitude of the residual deviations decreases progressively for polycrystals with large number of domains, as each realization will contain effectively all possible domain configurations. For the case of Fig. 1, as the number of domain configurations is 29000 and the mean domain size is 25 nm, this limit corresponds to polycrystals with sizes above 4.3 μm, about twice the size we are considering in this paper.

Optical Materials EXPRESS

Let us now consider the statistics of such deviations from repeated measurements of the polarization properties over a set of N polycrystal realizations, grown accordingly to the same distribution of grains sizes and orientations. In particular, we focus into the mean and standard deviation of the tilt-angle and ellipticity of each qth-order harmonic, with respect to that of the driving field, which we assume linearly polarized in the vertical direction,

$$\langle \theta^q \rangle = \frac{1}{N}\sum_j^N \theta_j^q, \qquad \langle \epsilon^q \rangle = \frac{1}{N}\sum_j^N \epsilon_j^q \tag{8}$$

$$\sigma_\theta^q = \sqrt{\frac{1}{N}\sum_j^N \left(\theta_j^q - \langle \theta^q \rangle\right)^2}, \qquad \sigma_\epsilon^q = \sqrt{\frac{1}{N}\sum_j^N \left(\epsilon_j^q - \langle \epsilon^q \rangle\right)^2} \tag{9}$$

where θ_j^q and ϵ_j^q are the tilt angle and ellipticity of the qth-order harmonic radiated by the j polycrystal realization. Consistently with the above discussion on the symmetries of single-crystal graphene's anisotropy, we find near vanishing results for the mean values in Eqs. (8), i.e. θ_q and ϵ_q are not sensitive enough to characterize the polycrystal domain distribution. In contrast, the standard deviations presented in Eqs. (9), σ_θ^q and σ_ϵ^q, for the harmonic orders 3rd to 9th show non-vanishing values, as shown in Fig. 2(d). Note that while the deviations of the ellipticity are rather small, those of the harmonic tilt-angle are large enough to be measured for the higher harmonics. Therefore harmonic tilt-angle deviation is a potentially useful parameter for the characterization of polycrystal domain order.

In order to demonstrate the sensitivity of the standard deviation σ_θ^q to the domain-size distribution, we have performed a series of calculations of σ_θ^7 for different Gaussian distributions, $\exp\left(-(s-s_0)^2/2\sigma^2\right)$, with s_0<1000 nm being the most frequent domain size and σ<360 nm. Figure 3(a) plots the results extracted from a set of 8×10^4 crystal realizations for each Gaussian distribution. The two insets in panel (a) represent two examples of domain distributions with s_0 = 500 nm and widths of 353.6 nm (upper inset, green) and 35.4 nm (lower inset, yellow). We find an approximate linear dependence of the tilt-angle standard deviation σ_θ^7 with the grain size s_0, with slopes varying as a function of the polycrystal distribution width σ. In all cases, the variations in the standard deviation σ_θ^7 with the distribution are of some tens of degrees, therefore sensitive enough to use this quantity in a polarimetric characterization of the distribution.

As a proof-of-concept, we finally propose a possible strategy for the characterization of the graphene polycrystal domain-size distribution based on high-order harmonic polarimetry. For this, we shall use Fig. 3(b), which shows the same information as Fig. 3(a) but representing the tilt-angle standard deviation σ_θ^7 (color scale) as a function of s_0 and σ. We now consider an hypothetical experiment in which we measure the tilt angle of the 7th harmonic, θ_j^7, for a set of $j \in N$ polycrystals, fabricated under similar conditions, and thus according to the same domain-size distribution. We compute the standard deviation of the measurements $\sigma_\theta^7\big|_{meas}$ according to Eq. (9). For concreteness, we have run a simulation of this hypothetical experiment using the distribution shown in Figs. 1(b) and 1(c), similar to that reported in [3], from which we obtain a value of $\sigma_\theta^7\big|_{meas} = 7.4°$. Knowing the value of $\sigma_\theta^7\big|_{meas}$, we choose the corresponding contour in Fig. 3(b) to find the relation between the grain-distribution width σ in terms of the most frequent size s_0. This contour predicts a width of σ_{exp} = 264.3 nm for s_0 = 25 nm, i.e. the most frequent size in the distribution of Figs. 1(b). The corresponding Gaussian profile is plotted in Fig. 1(b) as a solid black line. We confirm the accuracy of our method comparing σ_{exp} with the best Gaussian profile fit of the histograms in Fig. 1(b), which leads to the value of 275.8 nm.

In order to demonstrate the robustness of our procedure, in Fig. 3(c) we represent the corresponding contours resulting from the same road map applied to drivers with different intensities, from 3.5×10^{10} W/cm^2 to 1.14×10^{11} W/cm^2, and considering both the 7th and 9th harmonic-orders. The excellent overlapping of the contours reveals an extraordinary consistency

Optical Materials EXPRESS

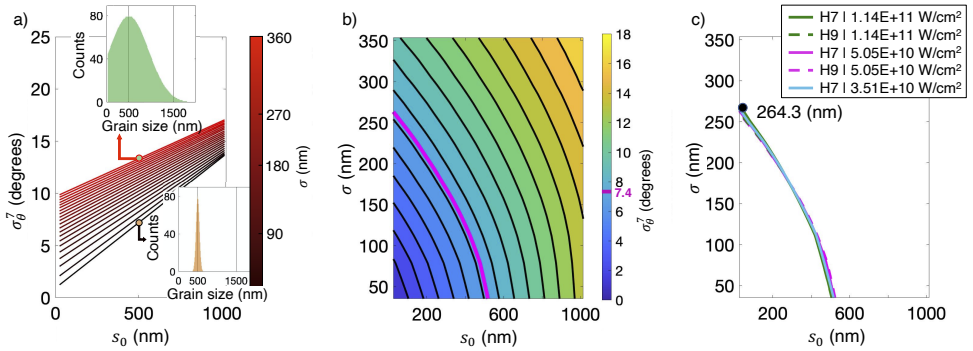

Fig. 3. a) Standard deviation of the 7th harmonic tilts σ_θ^7 computed for different Gaussian distributions of grain sizes, from wider (red light line) to narrower (red dark line). The insets show the Gaussian distributions for the wider case (green dot) and the narrower case (orange dot), respectively, centered at $s_0 = 500$ nm grain size. b) dependence of the tilt angle deviation σ_θ^7 in terms of the width σ and the most frequent size s_0 of the Gaussian distribution, the magenta line corresponds to all the contour $\sigma_\theta^7 = 7.4°$. Both a) and b) panels correspond to a driver of intensity of $5.1 \times 10^{11} W/cm^2$. c) shows the contours found for different driving intensities, from 3.5×10^{10} W/cm^2 to 1.14×10^{11} W/cm^2, and for harmonics 7th an 9th.

in the prediction of domain-size standard deviations using different drivers and harmonic orders. We believe that this result demonstrates the reliability of HHG polarimetry for the characterization of polycrystaline graphene.

4. Conclusion

We have proposed high-order harmonic polarimetry as a method for the characterization of domain parameters in single-layer graphene polycrystals. Our proposal stems from the recently reported non-linear anisotropy in single-crystal graphene. While our theoretical simulations show that the efficiency of high-order harmonic generation in polycrystals, as well as the ellipticity measurements, are not sensitive enough to the details of the polycrystal disorder, we demonstrate that the measurement of the tilt angle is indeed sensitive. As a proof-of-principle, we suggest a simple method to retrieve the width of the grain-size distribution from the statistical deviation of the measurements of the tilt rotation of the harmonics for a set of polycrystal realizations.

Funding. European Research Council (8511201); Ministerio de Educación y Formación Profesional (FPU18/03348); Junta de Castilla y León (SA287P18); Ministerio de Ciencia, Innovación y Universidades (PID2019-106910GB-100, RYC-2017-22745).

Acknowledgments. We acknowledge support from the European Research Council (ERC) under the European Union's Horizon 2020 research and innovation programme (grant agreement No. 851201).

Disclosures. The authors declare no conflicts of interest.

Data availability. Data underlying the results presented in this paper are not publicly available at this time but may be obtained from the authors upon reasonable request.

References

1. S. K. Tiwari, S. Sahoo, N. Wang, and A. Huczko, "Graphene research and their outputs: Status and prospect," J. Sci.: Adv. Mater. Devices **5**, 10–29 (2020).
2. M. Saeed, Y. Alshammari, S. A. Majeed, and E. Al-Nasrallah, "Chemical vapour deposition of graphene-synthesis, characterisation, and applications: A review," Molecules **25**(17), 3856 (2020).

Optical Materials EXPRESS

3. P. Y. Huang, C. S. Ruiz-Vargas, A. M. van der Zande, W. S. Whitney, M. P. Levendorf, J. W. Kevek, S. Garg, J. S. Alden, C. J. Hustedt, Y. Zhu, J. Park, P. L. McEuen, and D. A. Muller, "Grains and grain boundaries in single-layer graphene atomic patchwork quilts," Nature **469**(7330), 389–392 (2011).
4. B. G. Mendis, Q. M. Ramasse, T. P. Shalvey, J. D. Major, and K. Durose, "Optical properties and dielectric functions of grain boundaries and interfaces in cdte thin-film solar cells," ACS Appl. Energy Mater. **2**(2), 1419–1427 (2019).
5. W. Zhao, B. Xia, and L. L. , *et al.*, "Low-energy transmission electron diffraction and imaging of large-area graphene," Sci. Adv. **3**(9), e1603231 (2017).
6. Z. Ni, Y. Wang, T. Yu, and Z. Shen, "Raman spectroscopy and imaging of graphene," Nano Res. **1**(4), 273–291 (2008).
7. T. Popmintchev, M. C. Chen, and D. P. et al, "Bright coherent ultrahigh harmonics in the kev x-ray regime from mid-infrared femtosecond lasers," Science **336**(6086), 1287–1291 (2012).
8. X. Shi, C.-T. Liao, Z. Tao, E. Cating-Subramanian, M. M. Murnane, C. Hernández-García, and H. C. Kapteyn, "Attosecond light science and its application for probing quantum materials," J. Phys. B: At., Mol. Opt. Phys. **53**(18), 184008 (2020).
9. A. McPherson, G. Gibson, H. Jara, U. Johann, T. S. Luk, I. A. McIntyre, K. Boyer, and C. K. Rhodes, "Studies of multiphoton production of vacuum-ultraviolet radiation in the rare gases," J. Opt. Soc. Am. B **4**(4), 595–601 (1987).
10. M. Ferray, A. L'Huillier, X. F. Li, L. A. Lompre, G. Mainfray, and C. Manus, "Multiple-harmonic conversion of 1064 nm radiation in rare gases," J. Phys. B: At. Mol. Opt. Phys. **21**(3), L31–L35 (1988).
11. S. Ghimire and D. A. Reis, "High-harmonic generation from solids," Nat. Phys. **15**(1), 10–16 (2019).
12. K. J. Schafer, B. Yang, L. F. DiMauro, and K. C. Kulander, "Above threshold ionization beyond the high harmonic cutoff," Phys. Rev. Lett. **70**(11), 1599–1602 (1993).
13. N. Tancogne-Dejean and A. Rubio, "Atomic-like high-harmonic generation from two-dimensional materials," Sci. Adv. **4**(2), eaao5207 (2018).
14. A. García-Cabrera, C. Hernández-García, and L. Plaja, "Ultrafast sub-nanometer matter-wave temporal talbot effect," New J. Phys. **23**(9), 093011 (2021).
15. G. Vampa, C. R. McDonald, G. Orlando, D. D. Klug, P. B. Corkum, and T. Brabec, "Theoretical analysis of high harmonic generation in solids," Phys. Rev. Lett. **113**(7), 073901 (2014).
16. G. Vampa, T. J. Hammond, N. Thiré, B. E. Schmidt, F. Légaré, C. R. McDonald, T. Brabec, and P. B. Corkum, "Linking high harmonics from gases and solids," Nature **522**(7557), 462–464 (2015).
17. L. Yue and A. M. B. Gaarde, "Imperfect recollisions in high-harmonic generation in solids," Phys. Rev. Lett. **124**(15), 153204 (2020).
18. R. Boyero-García, A. García-Cabrera, O. Zurrón-Cifuentes, C. Hernández-García, and L. Plaja, "Non-classical high harmonic generation in graphene driven by linearly-polarized laser pulses," Opt. Express **30**(9), 15546–15555 (2022).
19. O. Zurrón, A. Picón, and L. Plaja, "Theory of high-order harmonic generation for gapless graphene," New J. Phys. **20**(5), 053033 (2018).
20. O. Zurrón-Cifuentes, R. Boyero-García, C. Hernández-García, and L. Plaja, "High harmonic generation in armchair carbon nanotubes," Opt. Express **28**, 719760 (2020).
21. J. Li, J. Lu, A. Chew, S. Han, J. Li, Y. Wu, H. Wang, S. Ghimire, and Z. Chang, "Attosecond science based on high harmonic generation from gases and solids," Nat. Commun. **11**(1), 2748 (2020).
22. O. Schubert, M. Hohenleutner, F. Langer, B. Urbanek, C. Lange, U. Huttner, D. Golde, T. Meier, M. Kira, S. W. Koch, and R. Huber, "Sub-cycle control of terahertz high-harmonic generation by dynamical bloch oscillations," Nat. Photon. **8**(2), 119–123 (2014).
23. N. Tancogne-Dejean, O. D. Mücke, F. X. Kärtner, and A. Rubio, "Impact of the electronic band structure in high-harmonic generation spectra of solids," Phys. Rev. Lett. **118**(8), 087403 (2017).
24. Y. S. You, D. A. Reis, and S. Ghimire, "Anisotropic high-harmonic generation in bulk crystals," Nat. Phys. **13**(4), 345–349 (2017).
25. H. Liu, Y. Li, Y. You, S. Ghimire, T. F. Heinz, and D. A. Reis, "High-harmonic generation from an atomically thin semiconductor," Nat. Phys. **13**(3), 262–265 (2017).
26. N. Yoshikawa, T. Tamaya, and K. Tanaka, "High-harmonic generation in graphene enhanced by elliptically polarized light excitation," Science **356**(6339), 736–738 (2017).
27. O. Zurrón-Cifuentes, R. Boyero-García, C. Hernández-García, A. Picón, and L. Plaja, "Optical anisotropy of non-perturbative high-order harmonic generation in gapless graphene," Opt. Express **27**(5), 7776–7786 (2019).
28. Z.-Y. Chen and R. Qin, "Circularly polarized extreme ultraviolet high harmonic generation in graphene," Opt. Express **27**(3), 3761–3770 (2019).
29. N. Klemke, N. Tancogne-Dejean, G. M. Rossi, Y. Yang, F. Scheiba, R. E. Mainz, G. Di Sciacca, A. Rubio, F. X. Kärtner, and O. D. Mucke, "Polarization-state-resolved high-harmonic spectroscopy of solids," Nat. Commun. **10**(1), 1319 (2019).
30. L. Zhou, H. Fu, T. Lv, C. Wang, H. Gao, D. Li, L. Deng, and W. Xiong, "Nonlinear optical characterization of 2d materials," Nanomaterials **10**(11), 2263 (2020).
31. M. S. Mrudul, "High-harmonic spectroscopy of two-dimensional materials," Ph.D. thesis, Indian Institute of Technology, Bombay (2021).
32. S. Reich, C. Thomsen, and J. Maultzsch, *Carbon Nanotubes: Basic Concepts and Physical Properties* (Wiley-VCH, 2004).

Chapter 5

Conclusions

This thesis presents an extensive study that explores the process of high-order harmonic generation (HHG) in single-layer graphene by an intense laser from microscopic and macroscopic points of view. From our study we can derive the following main conclusions:

1. We have demonstrated the substantial role of *imperfect recollisions* in HHG in monolayer systems without Berry curvature, using linearly polarized incident fields. We have shown that the classical trajectories are not capable of reproducing the full high-order harmonic spectrum, and a quantum perspective is needed to take into account non-zero electron-hole recollision distances. We have also verified the non-perturbative character of the process, similar to that of HHG in gases.

2. In the same way that occurs in gaseous media, the role of phase-matching is also relevant in solids. In this thesis we have demonstrated the influence of the *transverse phase-matching* in HHG in graphene, and its importance to reproduce the harmonic emission from a macroscopic target. As it can be seen from our results, the harmonic spectrum is dominated by the emission produced in a certain ring of the graphene layer, which is centered on the propagation axis.

3. As a proof-of-concept, we have designed a way to characterize polycrystalline graphene through polarimetry of the high-order harmonics emitted in the HHG process in polycrystalline graphene. We have been able to develop a technique to determine the distribution that follows the size domains forming the polycrystal.

From the methodological point of view:

1. We have extended the semiclassical description of HHG in graphene to include *imperfect recollisions*. This model allows us to calculate recombinations that occur when the electron and hole centers do not overlap spatially.

2. We have extended the macroscopic calculation of HHG in gases to a single layer of graphene. This allows us to identify the role of *transverse phase-matching* in HHG from two-dimensional materials.

3. We have developed a tool to calculate the high-order harmonic emission from polycrystals with different grain size and orientation distributions. In addition, we are able to calculate the total harmonic emission in this system, as well as its polarization.

5.1 Conclusiones

Esta tesis presenta un amplio estudio que explora el proceso de generación de armónicos de orden elevado (HHG) en una lámina de grafeno mediante un láser intenso desde puntos de vista microscópico y macroscópico. De nuestro estudio podemos derivar las siguientes conclusiones principales:

1. Hemos extendido el concepto de recolisiones imperfectas en HHG en cristales gruesos a sistemas monocapa sin curvatura de Berry y utilizando campos incidentes polarizados linealmente. Hemos demostrado que las trayectorias clásicas no son capaces de reproducir el espectro completo de armónicos y se necesita una perspectiva cuántica que tenga en cuenta distancias de recolisión en el par electrón-hueco diferentes a cero. También hemos comprobado el carácter no perturbativo del proceso, de la misma manera que ocurre en HHG en gases.

2. De la misma manera que ocurre en medios gaseosos, el papel del acuerdo de fase también es relevante en los sólidos. En esta tesis hemos demostrado la influencia del ajuste de fase transversal en la HHG del grafeno, y su importancia en la observación de las dinámicas macroscópicas del sistema. Como se puede ver en nuestros resultados, el espectro de armónicos está dominado por

la emisión producida en un cierto anillo de la lámina del grafeno, centrado en el eje de propagación.

3. Como prueba de concepto, diseñamos una estrategia para caracterizar el grafeno policristalino a través de medidas de polarización de los armónicos de orden elevado emitidos en el proceso de HHG en grafeno policristalino. Hemos sido capaces de desarrollar una técnica para determinar la distribución que sigue el tamaño de los dominios que forman el policristal.

Desde el punto de vista metodológico:

1. Hemos desarrollado una descripción teórica para identificar las recolisiones imperfectas que ocurren en el proceso de HHG en grafeno. Esta descripción nos permite calcular recombinaciones que se dan cuando los centros del electrón y el hueco no coinciden espacialmente.

2. Hemos extendido el cálculo macroscópico de HHG en gases a láminas monocapa, como el grafeno. Esto nos permite identificar el papel del ajuste de fase transversal en el proceso de HHG en materiales bidimensionales.

3. Hemos desarrollado una herramienta para calcular teóricamente policristales con diferentes distribuciones de tamaño y orientación de sus dominios. Además, somos capaces de calcular la emisión total de armónicos en estos sistema, así como su polarización.

Bibliography

1. D. Strickland, G. Mourou, Compression of amplified chirped optical pulses. *Optics Communications* **56**, 219–221 (1985).
2. T. Gaumnitz, A. Jain, Y. Pertot, M. Huppert, I. Jordan, F. Ardana-Lamas, H. J. Wörner, Streaking of 43-attosecond soft-X-ray pulses generated by a passively CEP-stable mid-infrared driver. *Opt. Express* **25**, 27506–27518 (2017).
3. A. McPherson, G. Gibson, H. Jara, U. Johann, T. S. Luk, I. A. McIntyre, K. Boyer, C. K. Rhodes, Studies of multiphoton production of vacuum-ultraviolet radiation in the rare gases. *J. Opt. Soc. Am B* **4**, 595–601 (1987).
4. M Ferray, A L'Huillier, X. F. Li, L. A. Lompre, G Mainfray, C Manus, Multiple-harmonic conversion of 1064 nm radiation in rare gases. *Journal of Physics B: Atomic, Molecular and Optical Physics* **21**, L31–L35 (1988).
5. P. B. Corkum, Plasma perspective on strong field multiphoton ionization. *Phys. Rev. Lett.* **71**, 1994–1997 (13 1993).
6. K. J. Schafer, B. Yang, L. F. DiMauro, K. C. Kulander, Above threshold ionization beyond the high harmonic cutoff. *Phys. Rev. Lett.* **70**, 1599–1602 (11 1993).
7. C. Kern, M. Zürch, C. Spielmann, Limitations of Extreme Nonlinear Ultrafast Nanophotonics. *Nanophotonics* **4**, 303–323 (2015).
8. X. F. Li, A. L'Huillier, M. Ferray, L. A. Lompré, G. Mainfray, Multiple-harmonic generation in rare gases at high laser intensity. *Phys Rev A Gen Phys* **39**, 5751–5761 (1989).
9. J. L. Krause, K. J. Schafer, K. C. Kulander, *Phys. Rev. Lett.* **68**, 3535–3538 (1992).
10. T. Popmintchev, M.-C. Chen, P. Arpin, M. M. Murnane, H. C. Kapteyn, The attosecond nonlinear optics of bright coherent X-ray generation. *Nature Photon* **4**, 822–832 (2010).

11. P. Salières, A. L'Huillier, M. Lewenstein, Coherence Control of High-Order Harmonics. *Phys. Rev. Lett.* **74**, 3776–3779 (19 1995).

12. P. Balcou, P. Sali'eres, A. L'Huillier, M. Lewenstein, Generalized phase-matching conditions for high harmonics: The role of field-gradient forces. *Phys. Rev. A* **55**, 3204–3210 (4 1997).

13. A. Rundquist, C. G. Durfee, Z. Chang, C. Herne, S. Backus, M. M. Murnane, H. C. Kapteyn, Phase-Matched Generation of Coherent Soft X-rays. *Science* **280**, 1412–1415 (1998).

14. C. G. Durfee, A. R. Rundquist, S. Backus, C. Herne, M. M. Murnane, H. C. Kapteyn, Phase Matching of High-Order Harmonics in Hollow Waveguides. *Phys. Rev. Lett.* **83**, 2187–2190 (11 1999).

15. M. B. Gaarde, J. L. Tate, K. J. Schafer, Macroscopic aspects of attosecond pulse generation. *J. Phys. B: At. Mol. Opt. Phys.* **41**, 132001 (2008).

16. P. M. Paul, E. S. Toma, P. Breger, G. Mullot, F. Augé, P. Balcou, H. G. Muller, P. Agostini, Observation of a Train of Attosecond Pulses from High Harmonic Generation. *Science* **292**, 1689–1692 (2001).

17. M. Hentschel, R. Kienberger, C. Spielmann, G. A. Reider, N. Milosevic, T. Brabec, P. Corkum, U. Heinzmann, M. Drescher, F. Kraus, Attosecond metrology. *Nature* **414**, 509–513 (2001).

18. M.-C. Chen *et al.*, Generation of bright isolated attosecond soft X-ray pulses driven by multicycle midinfrared lasers. *Proceedings of the National Academy of Sciences* **111**, E2361–E2367 (2014).

19. C. Hernández-García, T. Popmintchev, M. M. Murnane, H. C. Kapteyn, L. Plaja, A. Becker, A. Jaron-Becker, Isolated broadband attosecond pulse generation with near- and mid-infrared driver pulses via time-gated phase matching. *Opt. Express* **25**, 11855–11866 (2017).

20. D. D. Hickstein *et al.*, Non-collinear generation of angularly isolated circularly polarized high harmonics. *Nature Photonics* **9**, 743–750 (2015).

21. P.-C. Huang *et al.*, Polarization control of isolated high-harmonic pulses. *Nature Photonics* **12**, 349–354 (2018).

22. S. Ghimire, A. D. DiChiara, E. Sistrunk, P. Agostini, L. F. DiMauro, D. A. Reis, Observation of high-order harmonic generation in a bulk crystal. *Nature Physics* **7**, 138–141 (2011).

23. H. Liu, Y. Li, Y. S. You, S. Ghimire, T. F. Heinz, D. A. Reis, High-harmonic generation from an atomically thin semiconductor. *Nature Physics* **13**, 262–265 (2017).

24. A. A. Lanin, E. A. Stepanov, A. B. Fedotov, A. M. Zheltikov, Mapping the electron band structure by intraband high-harmonic generation in solids. *Optica* **4**, 516–519 (2017).

25. O. Schubert *et al.*, Sub-cycle control of terahertz high-harmonic generation by dynamical Bloch oscillations. *Nature Photonics* **8**, 119–123 (2014).

26. T. T. Luu, M. Garg, S. Y. Kruchinin, A. Moulet, M. T. Hassan, E. Goulielmakis, Extreme ultraviolet high-harmonic spectroscopy of solids. *Nature* **521**, 498–502 (2015).

27. Y. S. You, D. A. Reis, S. Ghimire, Anisotropic high-harmonic generation in bulk crystals. *Nature Physics* **13**, 345–349 (2017).

28. Y. S. You, J. Lu, E. F. Cunningham, C. Roedel, S. Ghimire, Crystal orientation-dependent polarization state of high-order harmonics. *Opt. Lett.* **44**, 530–533 (2019).

29. N. Tancogne-Dejean, O. D. Mücke, F. X. Kärtner, A. Rubio, Ellipticity dependence of high-harmonic generation in solids originating from coupled intraband and interband dynamics. *Nature Communications* **8**, 745 (2017).

30. N. Yoshikawa, T. Tamaya, K. Tanaka, High-harmonic generation in graphene enhanced by elliptically polarized light excitation. *Science* **356**, 736–738 (2017).

31. D. Baykusheva, A. Chacón, D. Kim, D. E. Kim, D. A. Reis, S. Ghimire, Strong-field physics in three-dimensional topological insulators. *Phys. Rev. A* **103**, 023101 (2 2021).

32. P. R. Wallace, The Band Theory of Graphite. *Phys. Rev.* **71**, 622–634 (1947).

33. H. P. Boehm, R. Setton, E. Stumpp, Nomenclature and terminology of graphite intercalation compounds (IUPAC Recommendations 1994). *Pure and Applied Chemistry* **66**, 1893–1901 (1994).

34. D. D. L. Chung, Review graphite. *Journal of Materials Science* **37**, 1475–1489 (2002).

35. K. S. Novoselov, S. V. M. A. K. Geim, Y. Z. D. Jiang, I. V. G. S. V. Dubonos, A. A. Firsov, Electric Field Effect in Atomically Thin Carbon Films. *Science* **306**, 666–669 (5659 2004).

36. K. S. Novoselov, Z. Jiang, Y. Zhang, S. V. Morozov, H. L. Stormer, U. Zeitler, J. C. Maan, G. S. Boebinger, P. Kim, A. K. Geim, Room-Temperature Quantum Hall Effect in Graphene. *Science* **315**, 1379–1379 (2007).

37. A. K. Geim, K. S. Novoselov, The rise of graphene. *Nature Materials* **6**, 183–191 (2007).

38. F. D. M. Haldane, Model for a Quantum Hall Eff'ect without Landau Levels: Condensed-Matter Realization of the "Parity Anomaly". *Phys. Rev. Lett.* **61**, 2015–2018 (1988).

39. J. R. Wallbank *et al.*, Tuning the valley and chiral quantum state of Dirac electrons in van der Waals heterostructures. *Science* **353**, 575–579 (6299 2016).

40. O. Zurrón, A. Picón, L. Plaja, Theory of high-order harmonic generation for gapless graphene. *New Journal of Physics* **20**, 053033 (2018).

41. S. A. Mikhailov, Non-linear electromagnetic response of graphene. *EPL* **79**, 27002 (2007).

42. S. A. Mikhailov, K. Ziegler, Nonlinear electromagnetic response of graphene: frequency multiplication and the self-consistent-field effects. *J. Phys.: Condens. Matter* **20**, 384204 (2008).

43. K. L. Ishikawa, Nonlinear optical response of graphene in time domain. *Phys. Rev. B* **82**, 201402 (2010).

44. N. Kumar, J. Kumar, C. Gerstenkorn, R. Wang, H. Chiu, A. L. Smirl, H. Zhao1, Third harmonic generation in graphene and few-layer graphite films. *Phys. Rev. B* **87**, 121406 (2013).

45. M. Taucer *et al.*, Nonperturbative harmonic generation in graphene from intense midinfrared pulsed light. *Phys. Rev. B* **96**, 195420 (2017).

46. N. R. Wilson *et al.*, Graphene Oxide: Structural Analysis and Application as a Highly Transparent Support for Electron Microscopy. *ACS Nano* **3**, 2547–2556 (2009).

47. X. Wang, L. Zhi, K. Müllen, Transparent, Conductive Graphene Electrodes for Dye-Sensitized Solar Cells. *Nano Lett.* **8**, 323–327 (2008).

48. Y. M. Lin, K. A. Jenkins, A. Valdes-Garcia, J. P. Small, D. B. Farmer, P. Avouris, Operation of Graphene Transistors at Gigahertz Frequencies. *Nano Lett.* **9**, 422–426 (2009).

49. P. Y. Huang *et al.*, Grains and grain boundaries in single-layer graphene atomic patchwork quilts. *Nature* **469**, 389–392 (2011).

50. H. Nishidome, K. Nagai, K. Uchida, Y. Ichinose, Y. Yomogida, Y. Miyata, K. Tanaka, K. Yanagi, Control of High-Harmonic Generation by Tuning the Electronic Structure and Carrier Injection. *Nano Lett.* **20**, 6215–6221 (2020).

51. R. Boyero-García, O. Zurrón-Cifuentes, L. Plaja, C. Hernández-García, Transverse phase matching of high-order harmonic generation in single-layer graphene. *Opt. Express* **29**, 2488–2500 (2021).

52. R. Boyero-García, A. García-Cabrera, O. Zurrón-Cifuentes, C. Hernández-García, L. Plaja, Non-classical high harmonic generation in graphene driven by linearly-polarized laser pulses. *Opt. Express* **30**, 15546–15555 (2022).

53. L. Yue, M. B. Gaarde, Imperfect Recollisions in High-Harmonic Generation in Solids. *Phys. Rev. Lett.* **124**, 153204 (15 2020).

54. L. Li, P. Lan, X. Zhu, T. Huang, Q. Zhang, M. Lein, P. Lu, Reciprocal-Space-Trajectory Perspective on High-Harmonic Generation in Solids. *Phys. Rev. Lett.* **122** (19 2019).

55. R. Boyero-García, A. García-Cabrera, O. Zurrón-Cifuentes, C. Hernández-García, L. Plaja, High-order harmonic spectroscopy of polycrystalline graphene. *Opt. Mater. Express* **12**, 3543–3550 (2022).

56. O. Zurrón-Cifuentes, R. Boyero-García, C. Hernández-García, A. Picón, L. Plaja, Optical anisotropy of non-perturbative high-order harmonic generation in gapless graphene. *Opt. Express* **27**, 7776–7786 (2019).

57. Óscar Zurrón-Cifuentes, R. Boyero-García, C. Hernández-García, L. Plaja, High harmonic generation in armchair carbon nanotubes. *Opt. Express* **28**, 19760–19771 (2020).

58. M. Göppert-Mayer, Über Elementarakte mit zwei Quantensprüngen. *Annalen der Physik* **401**, 273–294 (1931).

59. P. A. Franken, A. E. Hill, C. W. Peters, G. Weinreich, Generation of Optical Harmonics. *Phys. Rev. Lett.* **7**, 118–119 (4 1961).

60. R. W. Terhune, P. D. Maker, C. M. Savage, Optical Harmonic Generation in Calcite. *Phys. Rev. Lett.* **8**, 404–406 (10 1962).

61. C. Hernández García, PhD thesis, 2013.

62. T. F. Gallagher, Above-Threshold Ionization in Low-Frequency Limit. *Phys. Rev. Lett.* **61**, 2304–2307 (20 1988).

63. M. D. Perry, J. K. Crane, High-order harmonic emission from mixed fields. *Phys. Rev. A* **48**, R4051–R4054 (6 1993).

64. H. Eichmann, A. Egbert, S. Nolte, C. Momma, B. Wellegehausen, W. Becker, S. Long, J. K. McIver, Polarization-dependent high-order two-color mixing. *Phys. Rev. A* **51**, R3414–R3417 (5 1995).

65. I. J. Kim, C. M. Kim, H. T. Kim, G. H. Lee, Y. S. Lee, J. Y. Park, D. J. Cho, C. H. Nam, Highly Efficient High-Harmonic Generation in an Orthogonally Polarized Two-Color Laser Field. *Phys. Rev. Lett.* **94**, 243901 (24 2005).

66. M. Lewenstein, P. Balcou, M. Y. Ivanov, A. L'Huillier, P. B. Corkum, Theory of high-harmonic generation by low-frequency laser fields. *Phys. Rev. A* **49**, 2117–2132 (3 1994).

67. A. Zaïr *et al.*, Quantum Path Interferences in High-Order Harmonic Generation. *Phys. Rev. Lett.* **100**, 143902 (14 2008).

68. J. Crank, P. Nicolson, A practical method for numerical evaluation of solutions of partial differential equations of the heat-conduction type. *Mathematical Proceedings of the Cambridge Philosophical Society* **43**, 50–67 (1947).

69. J. D. Jackson, *Classical Electrodynamics* (Wiley, 1998).

70. L. V. Keldysh, IONIZATION IN THE FIELD OF A STRONG ELECTROMAGNETIC WAVE. *Zh. Eksperim. i Teor. Fiz.* **47** (Nov. 1964).

71. F. H. M. Faisal, Multiple absorption of laser photons by atoms. *Journal of Physics B: Atomic and Molecular Physics* **6**, L89–L92 (1973).

72. H. R. Reiss, Effect of an intense electromagnetic field on a weakly bound system. *Phys. Rev. A* **22**, 1786–1813 (5 1980).

73. J. A. Pérez-Hernández, L. Roso, L. Plaja, Harmonic generation beyond the Strong-Field Approximation: the physics behind the short-wave-infrared scaling laws. *Opt. Express* **17**, 9891–9903 (2009).

74. C. Hernández-García, I. J. Sola, L. Plaja, Signature of the transversal coherence length in high-order harmonic generation. *Phys. Rev. A* **88**, 043848 (4 2013).

75. C Hernández-García, J. S. Román, L Plaja, A Picón, Quantum-path signatures in attosecond helical beams driven by optical vortices. *New Journal of Physics* **17**, 093029 (2015).

76. F. Catoire *et al.*, Complex structure of spatially resolved high-order-harmonic spectra. *Phys. Rev. A* **94**, 063401 (6 2016).

77. E. Kogan, V. U. Nazarov, V. M. Silkin, M. Kaveh, *Phys. Rev. B* **89**, 165430 (16 2014).

78. F. Bloch, Über die quantenmechanik der elektronen in kristallgittern. *Z. Physik* **52**, 555–600 (1929).

79. O. Zurrón Cifuentes, PhD thesis, 2021.

80. X. Li *et al.*, Large-Area Synthesis of High-Quality and Uniform Graphene Films on Copper Foils. *Science* **324**, 1312–1314 (5932 2009).

81. O. V. Yazyev, Y. P. Chen, Polycrystalline graphene and other two-dimensional materials. *Nature Nanotech* **9**, 755–767 (2014).

82. M. Lewenstein, P. Salières, A. L'Huillier, Phase of the atomic polarization in high-order harmonic generation. *Phys. Rev. A* **52**, 4747–4754 (6 1995).

83. G. Vampa, C. R. McDonald, G. Orlando, D. D. Klug, P. B. Corkum, T. Brabec, Theoretical Analysis of High-Harmonic Generation in Solids. *Phys. Rev. Lett.* **113**, 073901 (7 2014).

84. D. Van Tuan, J. Kotakoski, T. Louvet, F. Ortmann, J. C. Meyer, S. Roche, Scaling Properties of Charge Transport in Polycrystalline Graphene. *Nano Letters* **13**, 1730–1735 (2013).